Behavior and Mechanisms of Doppler Wind Lidar Error in Varying Stability Regimes

Rachel Robey[1] and Julie K. Lundquist[2,3]

[1]Department of Applied Mathematics, University of Colorado Boulder, Boulder, Colorado, USA
[2]Department of Atmospheric and Oceanic Sciences, University of Colorado Boulder, Boulder, Colorado, USA
[3]National Renewable Energy Laboratory, Golden, Colorado, USA

Correspondence: Rachel Robey (rachel.robey@colorado.edu)

Abstract. Wind ~~lidar~~ lidars are widespread and important tools in atmospheric observations. An intrinsic part of lidar measurement error is due to atmospheric variability in the ~~remote sensing~~ remote-sensing scan volume. This study describes and quantifies the distribution of measurement error due to turbulence in varying atmospheric stability. While the lidar error model is general, we demonstrate the approach using large ensembles of virtual WindcubeV2 lidar performing ~~profiling doppler-beam-swinging (DBS) scans~~ a profiling Doppler-beam-swinging scan in quasi-stationary large-eddy simulations (LES) of convective and stable boundary layers. Error trends vary with the stability regime, time-averaging of results, and observation height. A systematic analysis of the observation error explains dominant mechanisms and supports the findings of the empirical results. Treating the error under a random variable framework allows for informed predictions about the effect of different configurations or conditions on lidar performance. Convective conditions are most prone to large errors (up to 1.5 $\mathrm{m\,s^{-1}}$ in the 1-Hz wind speed in strong convection), driven by the large vertical ~~velocities in convective plumes and exacerbated by~~ velocity variances in convective conditions and the high elevation angle of the scanning beams ~~. The violations of the assumption of horizontal homogeneity due to filtered turbulent velocity variances dominate the error variance, with the vertical velocity variations of particular importance. Range gate weighting contributes little to the variability of the error, but induces an underestimating~~ (62°). Range-gate weighting induces a negative bias into the horizontal ~~velocity~~ wind speeds near the surface shear layer ~~. Error~~ (-0.2 $\mathrm{m\,s^{-1}}$ in the stable test case). Errors in the horizontal wind speed and direction computed from ~~wind components is~~ the wind components are sensitive to the background wind speed but ~~has~~ have negligible dependence on the relative orientation of the instrument. Especially during low winds and in the presence of large errors in the ~~u and v~~ horizontal velocity estimates, the reported wind speed is subject to a systematic positive bias (up to 0.4 $\mathrm{m\,s^{-1}}$ in 1-Hz measurements in strong convection). Vector time-averaged measurements can improve the behavior of the error ~~distribution~~ distributions (reducing the 10-minute wind speed error standard deviation to < 0.3 $\mathrm{m\,s^{-1}}$ and the bias to < 0.1 $\mathrm{m\,s^{-1}}$ in strong convection) with a predictable effectiveness related to the number of decorrelated samples in the time window. Hybrid schemes weighting the 10-minute scalar- and vector-averaged lidar measurements are shown to be effective at reducing the wind-speed biases compared to cup measurements in most of the simulated conditions, with time-averages longer than 10-minutes recommended for best-use in some unstable conditions. The approach in decomposing the error mechanisms with the help of the LES flow field ~~extends~~ could be extended to more complex measurement scenarios and scans.

1 Introduction

Effectively and efficiently collecting observations of atmospheric winds poses an ongoing, ~~multifaceted~~ multi-faceted challenge for the atmospheric science community. Wind-profiling ~~lidar offers~~ light detection and ranging (lidar) instruments offer a cheaper, more easily deployable, and ~~higher-profiling~~ higher-ranging alternative to traditional meteorological towers while scanning lidar ~~allows~~ systems allow for collection of data over broad regions of the atmosphere. Over the last few decades, lidar technology has ~~grown into maturity~~matured, with several commercial wind lidar systems becoming available since the late 2000s. Lidar systems are widely employed in scientific studies of atmospheric boundary layer meteorology (Cheynet et al., 2017; Smith et al., 2019) and in assessments of wind resources (Gryning et al., 2017; Menke et al., 2020), wind turbine wake behavior (Aitken and Lundquist, 2014; Bodini et al., 2017), air quality (Liu et al., 2019), and fire meteorology (Clements et al., 2018). Lidar data, as opposed to ~~'point'~~"point"-measurements collected by ~~in-situ~~ in situ instruments like sonic anemometers, offer a more complex, indirect representation of the flow field ~~which~~ that must be analyzed critically and in conjunction with an understanding of what is being measured and the extent of its limitations and potential biases.

All wind lidar instruments function on the fundamental basis of sampling the flow along an emitted beam. With a single lidar's beam, only a one-dimensional, line-of-sight projection of the velocity can be measured. In light of this sampling limitation, dual- and ~~triple- lidar~~ triple-lidar methods have been explored to allow concurrent measurement of the necessary spanning wind vectors (Newsom et al., 2008; Stawiarski et al., 2013; Choukulkar et al., 2017; Menke et al., 2020). Use of single profiling or scanning lidar remains common and economic, so that quantifying their error behavior remains a high priority. Profiling lidar in particular make additional assumptions about the flow (usually ~~horizontal homogeneity~~"horizontal homogeneity", i.e. constant winds across the scan volume) to reconstruct an estimate of the three-dimensional (3D) winds at various heights from a series of measurements pointing the beam in different directions (Bingöl et al., 2009; Lundquist et al., 2015).

The error of ~~remote sensing~~ remote-sensing instruments like lidar, sodar, and radar depends not just on the system itself but is a statistical distribution arising from the interplay of the system with the turbulent atmospheric flow. Sources of error in profiling lidar measurement ~~were distinguished~~ are delineated by Gottschall and Courtney (2010). Uncertainties in the instrument hardware configuration (e.g. the beam angle) or in the alignment of the lidar ~~on site~~ on-site (e.g. leveling and direction) can introduce ~~error which~~ measurement errors that can roughly be controlled by the calibration accuracy. Additional error is inherent to the measurement system, depending on the atmospheric conditions~~and~~, the distribution of aerosols in the air, and the character of the flow itself. Measurements of mean horizontal winds in favorable (flat, uniform) conditions have generally performed well in field assessments; the ~~ten-minute~~ 10-minute averages of the horizontal wind have reported accuracy of 0.1-0.2 m/s with wind direction within 2° (Lindelöw, 2008; Cariou and Boquet, 2010). Questions about ~~measurements of vertical velocities and~~ the ability of wind profiling lidar to measure turbulence remain ~~areas of active research (Sathe et al., 2011; Sathe and Mann, 2012; Sathe et al., 2015; Newman et al., 2016)~~an active area of research (Sathe et al., 2011; Sathe and Mann, 2012; Sathe et al., 2015; Newman et al., 2016; Bonin et al., 2016).

The study of instrument error using numerical large-eddy simulations (LES) was introduced by Muschinski et al. (1999). The simulated flow, in conjunction with ~~radio wave scattering~~ radio-wave-scattering theory, represented the action of a radar wind

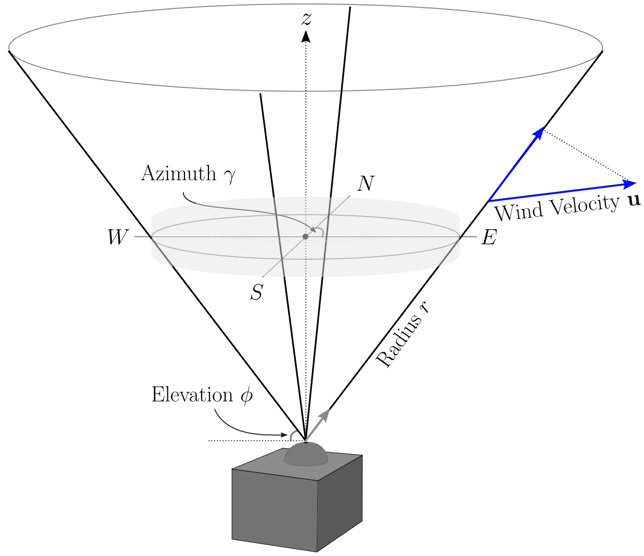

Figure 1. Geometry of a ~~Doppler Beam Swinging (~~DBS ~~)~~ scan performed by a Leosphere WindcubeV2 to estimate a vertical profile of the ~~three-dimensional~~ 3D wind velocity. At a frequency of ~~1s~~ 1 Hz, the sampling beam moves through a vertical and four angled positions corresponding to the cardinal directions. ~~Scan ranges from 40-240m above the ground.~~ The light grey cylinder demarcates a reference volume for the scan.

profiler in a flow field. Analysis of the virtual instrument data provided valuable insights into field study results concerning vertical-velocity bias and primary sources of ~~signal to noise~~ signal-to-noise ratio (SNR). Wainwright et al. (2014) leveraged LES in a similar way with a sodar simulator applied to a convective boundary layer. As wind lidar systems took off in popularity, interest grew for similar kinds of investigations ~~and the insights the combination of~~ combining a lidar model with LES ~~could provide into the instruments~~and the insights they might yield.

LES ~~enable~~ enables the generation of realistic turbulent atmospheric flows with which to study likely interactions and resulting error behavior of remote-sensing instruments. The spatial resolution of LES is typically on the order of ~~1-10s~~ one to tens of meters, and is designed to explicitly capture the most critical length scales in the atmospheric boundary layer while parameterizing the effects of the smallest turbulent scales. The resolution is not sufficient to explicitly compute the underlying optical measurement of scattering in profiling lidar; however, the salient effects of volume averaging and reconstruction over the scanning volume occur at a scale ~~which~~ that can be supported by the LES data. Compared to field studies of instrument accuracy, studies with virtual instruments in LES have unencumbered access to full knowledge of the flow field~~, allow for~~ . This knowledge enables control over the ~~the~~ case parameters (terrain, forcing, boundaries), and ~~can 'deploy'~~ so users can "deploy" instruments in ways that ~~are not~~ may not be physically or financially possible in reality (e.g. re-sampling the same flow field or testing many locations in a domain) (Muschinski et al., 1999; Stawiarski et al., 2013; Wainwright et al., 2014; Gasch et al., 2019). The comprehensive ~~flow field~~ flow-field data also opens up the discussion about the appropriate reference ~~'truth '~~ truth for lidar observations. Measurements may be better thought of as representing volume averages, which we cannot directly measure in the field but can compute a reference for in LESin an LES flow.

Earlier virtual lidar studies have generally considered complex lidar behavior and have been built on a range of different LES models. The coordinated use of multiple lidar devices to simultaneously probe spanning vectors of the wind in a volume was studied by Stawiarski et al. (2013) using the parallelized large-eddy simulation model (PALM) (Maronga et al., 2015) (Raasch and Schröter, 2001; Maronga et al., 2015). The dependence of profiling lidar on horizontal homogeneity complicates its use in complex terrain; Klaas et al. (2015) investigated observation deviations due to terrain and choice of instrument location. Gasch et al. (2019) implemented an airborne virtual lidar with PALM and studied errors due to flow inhomogeneities. Wind energy applications have been a notable driver of virtual lidar studies. Simley et al. (2011) modeled scanning continuous wave lidar to optimize their upwind measurements for use in wind turbine control. The measurement of turbine wakes with profiling lidar was explored in Lundquist et al. (2015) (using SOWFASimulator fOr Wind Farm Applications [SOWFA]) and Mirocha et al. (2015) (using WRF-LESWeather Research and Forecasting [WRF]-LES). Turbine wakes are also considered in Forsting et al. (2017), which focuses on the volume averaging along lidar beams in these high-gradient regions. Only recently has virtual lidar been employed for baseline studies of profiling wind lidar in favorable (flat, uniform, quasi-stationary) conditions. Rahlves et al. (2021) used virtual lidar in PALM LES to compare the bulk performance of various profiling scan types (DBS and VAD Doppler-beam-swinging [DBS] and velocity-azimuth-display [VAD] at varying cone angles) across a suite of convective conditions.

We have developed a virtual lidar model tool in Python to run on output from the Weather Research and Forecasting large-eddy simulation (WRF-LES). WRF-LES boasts a user base of over 48,000 and is attractive for its accessibility as an open-source, documented model. It can be configured for ideal simulations or coupled with mesoscale nesting to simulate case studies of real sites (Mazzaro et al., 2017; Haupt et al., 2019) , and offers a range of subfilterscale sub-filter-scale turbulence models for use in LES (Mirocha et al., 2010; ?)(Mirocha et al., 2010; Kirkil et al., 2012). In validations, WRF-LES has also compared well to observations of boundary layers in varying stabilities (Peña et al., 2021). Though the virtual lidar tool is targeted at WRF-LES, with minor adjustments to accommodate for the different output formats, it could be easily adapted for use with other LES models.

In this first demonstration of the virtual lidar tool, we consider a specific case of the Leosphere WindcubeV2 profiling lidar (Figure Fig. 1) measuring mean winds wind vectors in ideal simulations of stable and convective conditions over flat terrain. As in Rahlves et al. (2021), the configuration allows for a baseline assessment of the lidar performance by omitting external sources of inhomogeneities, like complex terrain or wind turbines, and isolates the system error arising from complex but statistically stationary turbulent boundary layer flow. Depending on the quantity of interest, Rahlves et al. (2021) found that the configuration choices (scan type, cone angle, averaging lengthtime) have distinct effects on the lidar retrieval error. Additionally, profiling in strongly convective conditions, absent other sources of inhomogeneity, the lidar exhibited markedly larger errors than in more moderate convection. Our work extends that study for a single DBS profiling scan to include a range gate range-gate weighting in the lidar model, a further stable stability regime, and the disaggregation of the vertical profile heights. The idea of using ensembles to gauge the uncertainty of the error (Rahlves et al., 2021) is expanded to using larger ensembles to characterize an error distribution particular to the flow conditions and scan geometry. Further, we present an analytic treatment of the observation system error to explain the dominant error mechanisms and trends, supporting the findings of the empirical results. The framework further enables informed, a priori predictions of how different configurations or conditions might be expected to impact lidar performance, without relying on the full virtual lidar model.

Section 2 presents the lidar model and its configuration to represent the WindcubeV2 lidar. It then describes the WRF-LES cases against which ensembles of the virtual instruments were tested. The resulting observation error distributions are summarized in section 3, focusing on empirical trends across stability conditions, height, and time-averaging. Section ?? analyzes the mechanisms behind the errors and the conditions which drive the trends found by the virtual lidar model. HereA corresponding, random-variable model of the error in the measurement is developed. Here, we address the expected influence of the range gate weighting function and analytically represent (RWF) and the impact of violations of the horizontal homogeneity assumption. Further treatment investigates the (uniformity) assumption. The expected behavior of the errors in the horizontal wind speed and direction measurements derived from the wind components and time-averaged measurements. arising from the reconstructed wind components is also treated, along with the effect of time-averaging. In Section 3, we present the error distributions of the ensemble of virtual measurements, focusing on trends with respect to stability condition, height, and over time averages of the measurements. The mechanisms and conditions driving the error behavior are analyzed through a combination of the analytic representation and the LES data. A discussion of how our findings relate to existing work and a summary of the key findings are given in Sections 4 and 5 respectively.

2 Data and Methods

2.1 Generalized virtual lidar model

The virtual lidar was is designed to create a configurable, general model that can be modified to replicate most lidar instruments. The observing system is decomposed into modular components common across lidar systems: the retrieval of radial wind velocities along an individual beam via a range gate weighting functionan RWF, the scanning pattern the beam moves through, and the internal post-processing of these measurements. The handling of each of the components can be easily modified and new definitions substituted to allow for customization.

This initial study focuses on a common commercial system: the vertical profiling Leosphere WindcubeV2 performing a Doppler-Beam-Swinging (DBS) scan (Figure DBS scan (Fig. 1). Its parameters and geometry, summarized in table Table 1, form the basis of the description of the model stages. Thorough discussions of the Windcube, other wind lidar systems, and the underlying technology can be found in Courtney et al. (2008); Lindelöw (2008); Cariou and Boquet (2010), Courtney et al. (2008), Lindelöw (2008), Cariou and Boquet (2010), and Thobois et al. (2015).

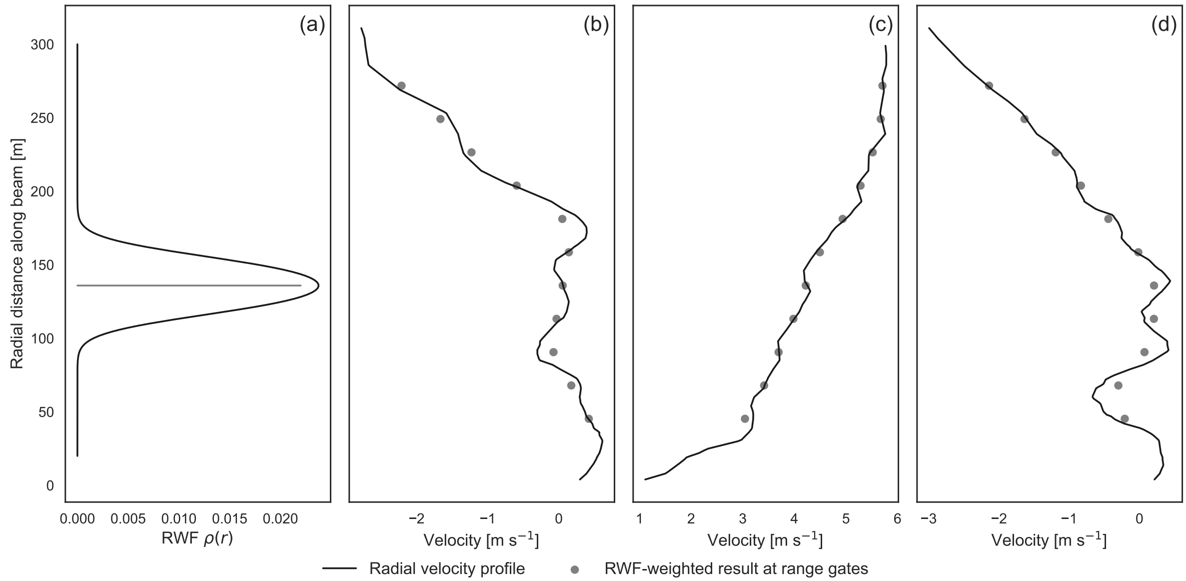

Figure 2. (a) ~~Range gate weighting function (~~WindcubeV2 RWF ~~)~~ centered at the ~~120m~~ 120 m range gate and examples (b, c, d) of ~~full,~~ unweighted radial velocity profiles~~along a beam~~, interpolated from instantaneous LES winds, compared to the corresponding weighted result at the range gates.

2.1.1 Sampling along a single lidar beam

The basis of wind lidar technology is the retrieval of radial (line-of-sight) wind velocities along an emitted laser beam using the backscatter off aerosols entrained in the flow. Doppler lidar devices diagnose the shift in the frequency of the backscattered light to measure radial wind velocity (~~equation~~ Eq. 1).

$$v_r = \hat{\boldsymbol{b}} \cdot \boldsymbol{u} = u \sin\gamma\cos\phi + v\cos\gamma\cos\phi + w\sin\phi \qquad (1)$$

The radial velocity, v_r, is the ~~dot product~~ projection of the wind velocity vector, $\boldsymbol{u} = (u, v, w)$ ~~with~~ onto the beam unit direction vector, $\hat{\boldsymbol{b}}$. We take u to be along the zonal ~~direction, and the beam unit directionvector~~ ~~$\hat{\boldsymbol{b}}$~~and v the meridional direction. The beam direction points along the azimuthal angle, $\gamma \in [0°, 360°)$, measured clockwise from north, and the elevation angle from the horizon, $\phi \in [0°, 90°]$. With this convention, positive radial velocities move away from the instrument.

In the context of our model, we assume ~~'perfect'~~ "perfect" conditions in the sense of ignoring factors like aerosol type, size, and density distribution and conditions like humidity, fog, or precipitation that can affect the quality of the return signal in the optical measurement of the radial velocity (Aitken et al., 2012; Boquet et al., 2016; Rösner et al., 2020). We similarly omit impacts of the carrier-to-noise ratio which can introduce additional uncertainty into the diagnosis of the radial velocity (Cariou and Boquet, 2010; Aitken et al., 2012). We instead focus on the representation of the averaging introduced by the sampling process.

Although the scattering cannot be explicitly resolved on an LES scale, previous studies have found that the full sampling procedure (collection and internal processing of backscattered light) is well-approximated by the application of ~~a range-gate weighting function (RWF)~~ an RWF (Frehlich, 1997; Gryning et al., 2017; Simley et al., 2018). Prevalent lidar technologies employ either continuous wave (e.g. ZephIR) or pulsed (e.g. Windcube) lasers to target distances along the beam at which to retrieve velocities. ~~Continuous wave~~ Continuous-wave systems set a focal distance to center returns, ~~while pulsed lidar~~ whereas pulsed lidar systems release a rapid sequence of pulses and separate the returns into a series of spatio-temporal ~~'range gates'~~ "range gates" along the beam. In both cases, the process acts like a weighted, volume average of radial velocities along the beam about the target distance. The cross-sectional area of the beam is ~~negligibly small~~ negligible compared to the along-beam length scale, so that the averaging may be described by a one-dimensional line integral. ~~The~~ At a target distance, r_0, the system-observed radial velocity~~at a distance r, $\overline{v}_r(r)$~~, $\overline{v}_r(r_0)$, is given by the convolution of projected wind velocities with the weighting function (~~equation~~ Eq. 2).

$$\overline{v}_r(r_0) = \int_{-\infty}^{\infty} \rho(s) v_r(r_0 + s) ds = \int_{-\infty}^{\infty} \rho(s) \hat{\boldsymbol{b}} \cdot \boldsymbol{u}((r_0 + s)\hat{\boldsymbol{b}}) ds \qquad (2)$$

$\rho(s)$ is the normalized RWF satisfying $\int_{-\infty}^{\infty} \rho(s) ds = 1$, ~~$\boldsymbol{b}$~~ $\hat{\boldsymbol{b}}$ is the beam direction unit vector, and $\boldsymbol{u}$ the velocity field.

For a pulsed lidar, the weighting function arises from the convolution of the range-gate profile with the ~~beam~~ pulse profile (Frehlich, 1997); ~~equation~~ Eq. 3 gives the integral in space.

$$\rho(r) = \int_{-\infty}^{\infty} g(r - s) \chi(s) ds \qquad (3)$$

A top hat, normalized indicator function, ~~χ~~ $\chi(s)$, represents the time span of the range gate and the pulse shape, ~~g~~ $g(s)$, is assumed to be Gaussian (Banakh et al., 1997). In the lidar operation, the parameters for the pulse and range gate are temporal quantities. To transform into their representation for the spatial integral, assume that propagation is at the speed of light, c (0.29979 m ns^{-1}), and note that the originating signal must travel to a point in space and back to the instrument receiver to be collected (Lindelöw, 2008; Cariou and Boquet, 2010). The indicator function for the ~~spatial range gatewith temporal interval~~ range gate, Δp, corresponding to the temporal interval, τ_m, is given in ~~equation~~ Eq. 4.

$$\chi(s) = \begin{cases} \frac{1}{\Delta p}, & s \in \left[-\frac{\Delta p}{2}, \frac{\Delta p}{2}\right] \\ 0, & \text{else} \end{cases}; \qquad \Delta p = \frac{c\tau_m}{2} \qquad (4)$$

We can ~~also~~ express the spatial Gaussian pulse in terms of the temporal full-width half-maximum (FWHM) parameter, τ (~~equation~~ Eq. 5).

$$g(s) = \frac{2\sqrt{\ln 2}}{\tau_s \sqrt{\pi}} \exp\left(-4 \ln 2 \frac{s^2}{\tau_s^2}\right); \qquad \tau_s = \frac{c\tau}{2} \qquad (5)$$

Table 1. Parameters used in the model to configure a representative WindcubeV2 lidar performing a DBS scan.

	WindcubeV2 ~~(table 1), the shape and extent of the RWF(equation 6)can be made concrete (figure~~
DBS Elevation Angle ϕ [deg]	62
DBS Elevation Angle ϕ [deg]	0, 90, 180, 270
Minimum Range Gate [m]	40
Range Gate Spacing [m]	20
Number of Range Gates [#]	11
Vertical Range Above Ground Level [m]	40-240
Frequency [Hz]	1
Range Gate Weighting Function (RWF)	Pulsed lidar (Eq. 6)
FWHM Pulse Width τ [ns]	165
Temporal Range Gate τ_m [ns]	265
Velocity Reconstruction Equation	Wind-direction weighted vertical (Eq. 9)

Cariou and Boquet (2010); Bodini et al. (2019)

The convolution integral (~~equation~~ Eq. 3) may be solved analytically in this case, yielding the expanded form (~~equation~~ Eq. 6) found in some references (Cariou and Boquet, 2010; Lundquist et al., 2015; Forsting et al., 2017).

$$\rho(r) = \frac{1}{c\tau_m}\left[\operatorname{erf}\left(\frac{4\sqrt{\ln 2}}{c\tau}r + \frac{\tau_m\sqrt{\ln 2}}{\tau}\right) - \operatorname{erf}\left(\frac{4\sqrt{\ln 2}}{c\tau}r - \frac{\tau_m\sqrt{\ln 2}}{\tau}\right)\right] \tag{6}$$

~~Here, c (0.29979 m/ns) is the speed of light, τ_m the temporal range gate, and τ the full width half maximum (FWHM) pulse duration.~~ Other representations of the pulse and range gate (i.e. not top hat and Gaussian) are not necessarily valid under this approximation. Lindelöw (2008), for example, adapted the form to account for a focused beam ~~which~~ that scales the RWF by the focusing efficiency. The basic, unadapted form presented here and implemented in our model for this study is also used in several other virtual lidar models (Stawiarski et al., 2013; Lundquist et al., 2015; Gasch et al., 2019; Forsting et al., 2017).

~~Using parameters from the~~

The RWF for the modeled WindcubeV2 (Fig. 2a) ~~. The~~ results from substituting its range gate and pulse parameters (Table 1) into the general, pulsed lidar equation (Eq. 6). The shape of the RWF peaks at the center and tapers symmetrically toward zero to either side. The weights drop to half their peak value about 20 ~~m to either side of~~ m from the target distance and are non-negligible up to around 40 ~~m. The choices of pulse and range gate parameters~~ m. The range-gate parameter in a coherent lidar system must balance the desire for spatial locality ~~(reducing the 'width' of the RWF)~~ and the need for ~~adequate accumulation time (τ_m) to accurately resolve frequencies used for~~ accurate frequencies used in measuring the radial velocity~~measurement. The~~. The more signal points from the traveling pulse used, i.e. the longer the range gate, the more accurate the diagnosis of the frequencies but the longer the averaging volume along the beam. The application of the RWF to the radial velocity profile may be thought of as a smoothing~~/~~, low-pass filter (~~figure 2(~~Fig. 2b,c,d~~)~~).

~~The form of the pulsed lidar RWF is distinct from that of continuous wave lidar (Gryning et al., 2017; Forsting et al., 2017). A major difference is the consistency of the pulsed RWF over target distances; the RWFs of continuous wave lidar vary with distance, giving better locality close to the instrument than far away. Closer distances will be sampled at higher resolution by a CW instrument and further distances by a pulsed lidar.~~

To compute the RWF-weighted retrieval from an LES flow field, the wind components are first interpolated to points along the beam and ~~the projection~~ then projected onto the beam direction~~found~~. The virtual lidar uses a linear barycentric interpolation from a triangulation of the LES grid (i.e. linear interpolation on tetrahedrons using Virtanen et al. (2020)~~, ?~~). The numerical approximation of the convolution integral ~~from the~~ of the RWF with the interpolated radial velocities treats the continuous weighted average as a discrete weighted average (~~equation~~ Eq. 7). The form is a slightly modified formulation of that used in Lundquist et al. (2015) and Forsting et al. (2017) (see ~~appendix~~ Appendix D).

$$\overline{v}_r(r_0) = \int_{-\infty}^{\infty} \rho(s) v_r(r_0+s)ds \approx \int_{\cancel{-T}\,-R}^{\cancel{T}\,R} \rho(s) v_r(r_0+s)ds \approx \sum_k \frac{h_k \rho(s_k)}{\sum_i h_i \rho(s_i)} v_r(r_0+s_k) \quad (7)$$

Parameterizing along the beam, the $\{s_i\}$ nodes are the points where the winds have been interpolated ($s_i = 0$ is at r_0). If the nodes are taken ~~as~~ to be midpoints of intervals with corresponding lengths $\{h_i\}$ ~~partitioning~~ that partition the integral range~~$[-T,T]$,~~ , $[-R,R]$, then the quadrature formulation is a normalized midpoint rule. The normalization ensures the result is a weighted average (avoiding over- or under-estimation due to the numeric weights not summing to unity). The placement of the nodes $\{s_i\}$ is free to be chosen for convenience or, as recommended by Forsting et al. (2017), to optimize utility of the interpolated points in the convolution so that fewer points need be interpolated. Our current implementation uses equi-spaced points ~~one meter~~ 1 m apart along the beam (see ~~appendix~~ Appendix D for discussion).

~~Interpolation dominates the computational work in most virtual lidar models, making it a prime target for performance optimization. Some preliminary efforts have been made in our implementation, e.g. computing and saving interpolation weights to reuse for the different velocity components and for repeating beams on a static grid. Further improvements to the implementation and choice of nodes are possible and will be targeted in subsequent developments.~~

2.1.2 Time-resolved scanning patterns

Based on the type of scan they perform, lidars are categorized as profiling or scanning systems. Profiling lidars are designed to provide a vertical profile of the ~~three-dimensional~~ 3D wind velocity, much as would be reported by a meteorological tower. To reconstruct a ~~three-dimensional~~ 3D wind vector, the instrument needs spanning radial velocity samples from at least three different directions. The scanning head rotates through the necessary positions quickly, which limits the intervening evolution of the wind field. ~~Scanning lidars perceive the atmosphere in a fundamentally different way; they move the beam more slowly through a slice of the atmosphere, resolving the radial velocity of features in the spatial selection. Common configurations include vertical slices (range height indicator or RHI scan) which fix the azimuthal angle while varying elevation; conical slices (vertical azimuthal display or VAD scan) which fix the elevation angle but slowly complete a full rotation, or a partial conical section (plan position indicator or PPI scan), as visualized in Clifton et al. (2015).~~ Any scanning geometry, ~~as described~~

above or a more complex configurationthat described here or other common or complex options (Clifton et al., 2015), arises from 'pointing' "pointing" the beam and is most naturally and compactly represented as a time series of elevation, ϕ, and azimuthal, γ, angles in spherical coordinates with the beam source at the origin.

For the purposes of this study, we consider the Doppler-beam-swinging (DBS) DBS profiling scan used by the WindcubeV2, which moves through the four cardinal directions, angled 28° from the vertical62° from the horizon, before pointing the beam straight vertically (Figure Fig. 1). The total scan takes approximately 5 seconds5 s, spending about a second at each of the scan positions (Bodini et al., 2019). The range gates correspond to equi-spaced heights above the ground. The vertical range of the WindcubeV2 is determined by the number and spacing of the range gates and a typical configuration for the instrument has 11 range gates spaced vertically every 20 m from 40 to 240 m above ground level (Table 1). As the beam rotates through the scan, radial velocities are measured at the center and four points around the circular perimeter of the scanning cone for each given height. At each second in the post-processing stage, the most recent set of radial velocities is used to reconstruct an estimate of the vertical profile of three-dimensional 3D velocities.

The beam accumulation time for the WindcubeV2 is about a second, while whereas the LES model time steps are on the order of a tenth of a second. The additional averaging due to the longer accumulation time is ignored in the current version of the virtual lidar; it handles the scan by performing the beam sampling on snapshots of the flow field output at one second 1-s intervals. It is assumed that in the WindcubeV2, the temporal average is less significant than the spatial averaging; future versions of the model will account for accumulation times by performing this averaging step explicitly.

2.1.3 Internal processing: 3-D 3D velocity reconstruction

In the WindcubeV2, the post-processing stage reconstructs the three-dimensional 3D velocity from the radial velocities collected across the scan cycle. Under the assumptions of horizontal homogeneity and invariance of the flow field (i.e. constant winds) over the scan volume and invariance over the scan duration, the radial velocities collected by each of the beams at a given height are all projections of the same three-dimensional 3D velocity vector. Omitting the vertical beam, we solve for the vector components at a given range gate height (equation 8) as in, e. g. Cariou and Boquet (2010). Eq. 8) (Cariou and Boquet, 2010).

$$\boldsymbol{u}_{lidar\,l} = \begin{pmatrix} \dfrac{v_{r,E} - v_{r,W}}{2\cos\phi} \\ \dfrac{v_{r,N} - v_{r,S}}{2\cos\phi} \\ \dfrac{v_{r,N} + v_{r,E} + v_{r,S} + v_{r,W}}{4\sin\phi} \end{pmatrix} \tag{8}$$

At a fixed height, $u_{E,W,N,S}$ $v_{r,E,W,N,S}$ are the most recently measured radial velocities ($\overline{v}_r(r)$$\overline{v}_r(r_0)$) from beams pointed in each of the cardinal directions. The elevation angle of the beams from the horizon is $\phi = 62°$.

Later versions of Leosphere's Windcube instruments use a modified reconstruction (Krishnamurthy, 2020) for the vertical velocity (equation Eq. 9), which weights the beams in the reconstruction using the estimated wind direction, Θ, measured clockwise from due north, as presented in Newman et al. (2016) and Sathe et al. (2011). Re-weighting emphasizes beams

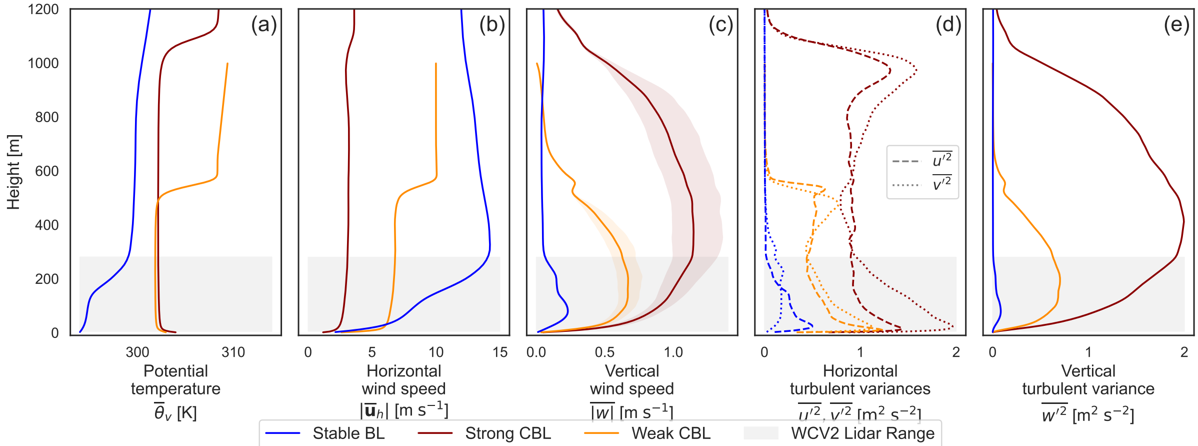

Figure 3. For each of the idealized LES cases, mean profiles of (a) virtual potential temperature; (b) horizontal winds: wind speed(solid), U (dashed) and V (dotted); and (c) mean vertical velocity magnitudes (solid) and with shaded color indicating the span between mean magnitudes over just the positive (dashed) and negative (dotted) vertical velocity and positive values. Panels (d) and (e) show the The turbulent velocity variances, $\overline{u'^2}$ (dashed) , and $\overline{v'^2}$ (dotted), and are shown in (d) with $\overline{w'^2}$ in panel (solide). The grey region demarcates the WindcubeV2 vertical range including the region of influence for the range gate range-gate weighting.

along the mean wind direction, exploiting the fact that decorrelation distances along the mean wind direction are typically longer than along the cross-stream direction.

$$\boldsymbol{u}_{lidar\,l} = \begin{pmatrix} \dfrac{v_{r,E} - v_{r,W}}{2\cos(\phi)} \\ \dfrac{v_{r,N} - v_{r,S}}{2\cos(\phi)} \\ \dfrac{(v_{r,N} + v_{r,S})\cos^2(\Theta_l) + (v_{r,E} + v_{r,W})\sin^2(\Theta_l)}{2\sin(\phi)} \end{pmatrix} \tag{9}$$

When the mean wind direction is at a 45° angle to the lidar axes (delineated by the south-north and east-west beam pairs), the weights reduce to the uniform $\frac{1}{4}$ in the original reconstruction (equation Eq. 8). When the mean wind aligns directly with one of the lidar axes, only the two respective beams on that axis are used. For our tests, we use reconstruction with wind-direction weighting to represent currently utilized versions of the instrumentWe compare the error in both approaches as well as the measurement by the vertically pointing beam (Section 3.4).

2.2 Idealized atmospheric boundary layer simulations of varying stability

Realistic atmospheric flow fields were generated using large-eddy simulation (LES) are generated using LES configurations of the Advanced Research Weather Research and Forecasting (WRF-ARW) model v4.1 (Skamarock et al., 2019). WRF-ARW is a finite difference numerical model which that solves the flux form of the fully compressible, nonhydrostatic Euler equations

Table 2. Parameters for WRF LES runs used to represent different stability regimes.

Case	Strong CBL	Weak CBL	Stable BL
Domain Size ($L_x \times L_y \times L_z$) [~~km~~km]	(5×5×2)	(3×3×1)	(9×3.99×2.5)
Cell Count ($N_x \times N_y \times N_z$)	(500×500×200)	(500×500×160)	(1300×570×66)
Horizontal Resolution [~~m~~m]	10	6.25	7
Bottom Cell Height [~~m~~m]	3	3	5
Surface Heating [~~K m s^{-1}~~K m s^{-1}]	0.24	0.1	–
Surface Cooling Rate [~~K h^{-1}~~K h^{-1}]	–	–	-0.5
Obukhov Length [~~m~~m]	-5.44	-12.32	78
Friction Velocity [~~m s^{-1}~~m s^{-1}]	0.29	0.44	0.21
Boundary Layer Height [~~m~~m]	1050	525	170
Typical ~~100m~~ 100-m winds ($\overline{\lvert U\rvert}, \overline{\lvert V\rvert}, \overline{\lvert W\rvert}$) [~~m/s~~m s^{-1}]	(2.8,0.2,0.9)	(6.4, 1.3, 0.6)	(8.4, 0.2, 0.2)

for ~~high Reynolds number~~ high-Reynolds-number flows. The model runs on a staggered, Arakawa-C grid with stretched, terrain-following hydrostatic pressure coordinates in the vertical. The simulations in this study ~~employed~~ employ a third-order Runge-Kutta time integrator and fifth- and third-order horizontal and vertical advection. All simulations ~~used a nonlinear~~ use a non-linear backscatter and anisotropy (NBA2) ~~sub-filter scale~~ sub-filter-scale stress model (Mirocha et al., 2010).

To establish a baseline reference for lidar operation in ideal conditions, all simulations in this study ~~used~~ use uniform flat, grassy terrain (roughness length ~~$z_0 = 0.1m$~~$z_0 = 0.1$ m), periodic boundary conditions, ~~with~~ and temporally and spatially invariant forcing. The idealized scenarios isolate fundamental characteristics of the atmospheric flows, removing potential influence from additional complexities and inhomogeneities~~from~~ , e.g. mesoscale forcing, varied terrain and land cover, and the influence of the diurnal cycle or nearby obstructions like wind turbines. None of the simulations in this study ~~incorporated~~ incorporate models for moisture, clouds, radiation, microphysics, or land surface. The simulations ~~were~~ are distinguished by varying stability: two convective cases and one stable stratification case, detailed in ~~table 2 and figure~~ Table 2 and Fig. 3. For each of the simulations, we ~~used ten~~ use 10 minutes of simulated time after spin-up ~~was~~ has been achieved, output at ~~one second~~ 1-s intervals.

For the convective boundary layers (CBLs), we use data from ~~precursor~~ precursory simulations in Rybchuk et al. (2021), which emulate observed conditions during the Project Prairie Grass campaign (Barad, 1958). Following the labeling therein, we designate the cases as the ~~'strong' and 'weak'~~ "strong" and "weak" convective boundary layers. Although both are considered strongly convective by their Obukhov length classification (Muñoz-Esparza et al., 2012) and are largely dominated by cell structures (Salesky et al., 2017), the cases differ meaningfully in the relative strength of the surface heating and geostrophic winds. The strong CBL case features stronger heating and slower winds than the weak CBL.

The ~~stable boundary layer~~ stable-boundary-layer simulation closely follows the configuration of Sanchez Gomez et al. (2021). The surface condition for the stable case is driven with a cooling rate, rather than a negative heat flux (Basu et al., 2007). Spinning up a stable case to relatively steady turbulence statistics can also be computationally expensive; a set of two one-way nested domains ~~was~~ is used to reduce the computational demand. The parent domain has periodic boundary conditions and a horizontal resolution of ~~70m~~70 m. It evolves for about 13.5 hours before the inner domain is started and simulated over the final 45 minutes. To reduce the fetch required to spin up fine turbulence in the nested interior grid, we employ the cell-perturbation method ~~(CPM)~~ from Muñoz-Esparza et al. (2014). The first 30 minutes of data from the fine-scale domain are discarded and only an interior region excluding fetch and edge effects is used for the virtual lidar sampling.

Mean profiles, computed with data from the valid regions of the LES cases, are characteristic of the respective stability regimes (~~figure~~ Fig. 3). Well-developed mixed layers, with consistent virtual potential temperature and wind speeds, account for the majority of the lidar observation range in the convective boundary layers. The bottom two reported range gates, however, incorporate values from the surface layer due to ~~range gate~~ range-gate weighting. The weaker convective case has significantly stronger winds and the surface heating only supports a boundary layer about half as high as in the strong CBL case. The entrainment zone is out of lidar range in both cases. Vertical velocity magnitudes reach maximum values in the middle of the convective boundary layers, with a notable gap between the mean negative and positive values reflecting strong upward plumes and weaker, broader downdrafts. In the stable case, the boundary layer falls entirely within the lidar range. The distinctive temperature stratification is paired with strong winds that reach a maximum in a jet not far above the top of the boundary layer. Vertical velocities are typically small and balanced and become negligible aloft.

2.3 ~~Configuration of virtual WindcubeV2 ensemble~~

2.2.1 Configuration of virtual WindcubeV2 ensemble

~~Parameters used in the model to configure a representative WindcubeV2 lidar performing a DBS scan. WindcubeV2 DBS Elevation Angle ϕ deg62 Minimum Range Gate m40 Range Gate Resolution m20Number of Range Gates #11 Frequency Hz 1 Range Gate Weighting Function (RWF) Pulsed lidar (equation 6)FWHM Pulse Width τ ns165 Temporal Range Gate τ_m ns265 Velocity Reconstruction Equation Wind-direction weighted vertical (equation 9)~~

A virtual WindcubeV2 is created in the lidar model as described in ~~the previous section~~ Section 2.1 and summarized in ~~table~~ Table 1. To maximize realizations of the instrument sampling from each of the LES flows, a grid of ~~forty-five~~ 45 instances of the virtual WindcubeV2 is placed ~~throughout~~ in each domain. The locations are spaced such that their scanning volumes ~~did~~ do not overlap. Each lidar scan coincides uniquely with surrounding flow structures, comprising a statistical sample ~~from which to diagnose general trends in~~ of how the instrument might interact with the distinctive atmospheric variability of each regime.

The mean background states of the LES cases are spatially and temporally consistent across the domain, including the direction of the prevailing winds. To account for potential differences due to the relative orientation of the lidar axes in the flow, the ensemble of virtual lidar ~~were~~ instruments is re-oriented at three additional offset angles ~~$\{15°, 30°, 45°\}$~~ $(15°, 30°, 45°)$, and allowed to sample the LES fields again. The ~~small~~ negligible sensitivity of the error to the relative orientation is discussed in ~~section ??~~Section 3.2.

Determining the error in the lidar observation depends on defining a reference ~~'truth'~~ truth. Profiling lidar are often thought of as replacing meteorological towers, returning a vertical profile of ~~three-dimensional~~ 3D velocities similar to a tower fitted with instruments, but what value the lidar should actually be thought of as ~~'measuring '~~ measuring is not so straightforward. The samples used to estimate the wind components lack the precise locality of tower instruments; the beams collecting line-of-sight data span an increasingly large area with height, each incorporating ~~additional~~ a vertical extent via the RWF. These factors suggest that a volume average might be a more appropriate reference truth (as suggested in ~~e.g.~~ Courtney et al. (2008)). The lidar reflects pieces of both representations: it has the spatial spread of the volume average, but depends on only a handful of points on the edge of the volume ~~which~~ that impart higher variability similar to a pointwise profile.

Along with a ~~'pointwise'~~ "pointwise", tower-style truth profile of interpolated velocities above the instrument, we determined a volume-averaged profile for each lidar. The ~~volume-average was~~ volume average is computed as the mean of all LES points ~~which~~ that fall inside cylinders tracing the lidar scan radius (~~figure~~ Fig. 1). Centered at each range gate, the cylinders ~~were~~ are defined to have a radius equal to that of the scan cone and height corresponding the ~~the~~ vertical projection of the RWF range resolution. For the WindcubeV2, the range resolution is the FWHM of the RWF ~~($\approx 40m$)~~ so that the cylinders are ~~$40\sin(\phi) \approx 35.3m$~~ $40\sin(\phi) \approx 35.3$ m tall. At the lowest levels with the smallest volumes, a minimum of around 80 LES points are used~~which increased~~, which increases to several hundred points in the top cylinders.

3 ~~Observation error trends~~

2.1 Random-variable model of error

~~The error incurred in any individual measurement does not necessarily represent general behaviors; deducing useful, generalizable trends entails focusing instead on distributions of the observation error. Each virtual instrument in the ensemble provides one instance of the ways the WindcubeV2 might interact with turbulent features in each flow regime, thereby sampling the error distribution. We characterize the resulting error distribution, and trends in its behavior, from the raw 1Hz lidaroutput as well as for time-averaged quantities.~~

~~We define the lidar error as the difference between the lidar-observed value and the reference truth, $u_{err} = u_{lidar} - u_{ref}$. Along with errors in each of the reconstructed wind components (u, v, w) we consider errors in the horizontal wind speed and direction derived from the components (equation 17) which are also reported by the lidar and commonly used.~~

$$|\boldsymbol{u}_{h,lidar}| = \sqrt{u_{lidar}^2 + v_{lidar}^2}, \qquad \Theta_{lidar} = \arctan 2(-u_{lidar}, -v_{lidar})$$

~~The wind direction, placed in the appropriate quadrant, is compactly represented by the two-argument inverse tangent (the sign and order of the arguments follows meteorological conventions with the angle measuring the wind source clockwise from north). Wind direction error is bound in the interval $(-180°, 180°)$ where positive values indicate the lidar reading an angle clockwise from truth and negative values an angle counter-clockwise from truth.~~

2.2 ~~Raw 1-second velocities~~

(a)(b)(c)Kernel density estimates (KDEs) of aggregated wind speed error distributions. Errors are computed with respect to the volume average at each height for the (a) strong CBL (b) weak CBL, and (c) stable BL. Each distribution consists of 108,000 data points.

A lidar reports a vertical profile of velocities each second for the ten minute duration of the simulation. Each distribution consists of ten minutes of data combined over the 45 ensemble members and four orientation angles, giving a total of 108Alongside the virtual model of the lidar, 000 error samples. Disaggregating by height and stability, kernel density estimates (KDE) of the error histogram visualize the resulting distribution. Collating the KDEs into a ridgeline plot (figure 6), distinct variations in the distribution center, width, and shape appear. The distribution width in particular varies heavily with stability and height. Visual inspection confirms that the distributions are well-behaved and roughly normal with one central peak.

Statistical moments serve to summarize and quantify the properties of the distributions, facilitating intercomparison and the identification of trends. For each distribution, we computed the first four moments: unbiased estimators of the mean, centered variance/standard deviation, and standardized skewness and excess kurtosis (definitions in appendix **??**). The mean, μ, represents the expected error, with non-zero values indicating a bias in the lidar observation. The centered variance, σ^2, measures the spread of the distribution about the mean, though the corresponding standard deviation, σ, can be easier to intuit as an indication of the distribution width and represents typical error magnitude in the original measurement units. For centered (zero mean) distributions, the standard deviation is comparable to the root-mean-squared-error (RMSE or RMSD) metric.

The higher-order moments of skewness and kurtosis, normalized by the standard deviation, are non-dimensional descriptors of the the distribution shape, namely asymmetries and decay of the tails. With a few exceptions, the metrics suggest that the distributions do not differ substantially from normal. There is a slight positive skewness (long tail on the positive side of the distribution) in wind speed estimates (0.25 in strong convection). The bottom range gates, influenced by the surface layer, also deviate from normal under strong convection: there is evidence of slight positive skewness (0.4) at the surface in wind direction and negative skewness (0.4) in the vertical velocity. Generally the excess kurtosis, though not extreme (+1-2), indicates more slowly decaying tails than those found in a normal distribution. The effect is more pronounced near the surface. Wind direction at the surface exhibits the most extreme behavior with an excess kurtosis of +8 at the surface. The distributions should be regarded as having more 'outliers' with respect to the width than would be found in a normal distribution.

Mean and standard deviation of error in wind speed and wind direction using both volume-averaged truth (dotted) and pointwise 'tower' truth (dashed). Stability cases are distinguished by line color. For wind speed, the primary axis gives absolute error and colored secondary axes designate relative error with respect to 100m values for the respective LES case.

Mean and standard deviation of error in vertical velocity reconstruction (equation 9) using both volume-averaged truth (dotted) and pointwise 'tower' truth (dashed). Stability cases are distinguished by line color. The primary x-axis gives absolute error and colored secondary x-axes designate relative error with respect to typical, 100m values for the respective LES case.

The rest of discussion focuses on trends in the the mean and standard deviation of the error . For the sake of space, they are only shown for the wind speed and direction (figure 11) and for the vertical velocity (figure **??**); see appendix A for the first four moments for all variables. Patterns in the error behavior are considered over stability cases, with respect to height, and as they appear in particular measured quantities.

In all cases, the distribution of the error with respect to the pointwise truth displays larger standard deviation than the error using the volume-averaged truth. With the beam measurements at the perimeter of the scan volume, the lidar reconstruction has no way to predict small-scale variations at the center of the volume where the pointwise truth resides. It can only reconstruct an average representation, and comparison with the point value incorporates additional uncertainty into the error through the pointwise truth reference.

The stability case and corresponding structure of the boundary layer powerfully influence the error behavior. The strong convective case consistently suffers from more significant error, with greater bias and standard deviation in the wind speed, wind direction and vertical velocity error. It is followed by the weak CBL, with the stable case being the best behaved. The primary mechanisms identified in section **??** justify the relative ordering. The heterogeneity, especially in the vertical velocity, of the convective plumes strongly drives the error while high wind speeds in the stable case help to reduce it.

Height trends depend on the change in volume circumscribed by the scan, but also on the vertical structure of the boundary layer (figure 3) and corresponding scale and character of the turbulent structures as noted by Wainwright et al. (2014) for sodar measurements. In the test convective conditions, the standard deviation of the error grows with height up to the top of the Windcube range. The error growth tracks the growth in the vertical velocities from the lower layers the middle of the boundary layer where the convective plumes are strongest. In the stable case, the standard deviation reaches a maximum just below the boundary layer height at 170m. The peak in the error spread seems to occur close to the infection point in the v mean velocity and we develop an analytic model of the maximum vertical velocity magnitude. In these quasi-stationary conditions, the height trends depend strongly on the vertical structure of the flow, not just the size of the scan volume.

Some error traits are particular to the quantity being measured, outside of the general trends identified above. The wind speed measurement exhibits a bias toward over-estimation (positive error mean), particularly in convective conditions. In the stable case, the distribution is more centered except close to the surface where the mean becomes negative (underestimate). Under strong convection, the wind direction observations also suffer from a bias; the direction lists more and more counter-clockwise (southward) from truth with height. In the vertical velocity reconstruction, the relative error can grow to large fractions of typical magnitudes in all stability cases, obscuring the actual signal in the measurement. Note the inversion of the usual stability ordering in the vertical velocity mean error: measurements in weak convection experience larger bias than in strong convection. The vertical velocity error distributions using point or volume-averaged truth references do not mirror one another as they do for the other variables. Since the variability in vertical velocity occurs on a shorter scale, the pointwise value is less representative of the volume average which explains the greater discrepancy. The error in the WindcubeV2 reconstruction of vertical velocity (equation 9) shown here is compared against that in the equally-weighted reconstruction (equation 8) and direct measurement by the vertical beam in section **??**.

(a)(b)(c)Kernel density estimates (KDEs) of the wind speed error distribution for a single lidar over 10 minutes. Errors are computed with respect to the volume average at each height for the (a) strong CBL (b) weak CBL, and (c) stable BL. Each distribution consists of 600 data points. The distributions are not representative.

The aggregate distributions described here are the result of large ensembles over turbulence realizations. They describe the distribution of the error in a single measurement made by an instrument randomly dropped into each stability regime. A time series of measurements does not randomly sample the aggregate distribution, rather it does so selectively based on the character of the few turbulent structures encountered. The selective sampling implies that the distribution of error in measurements made by a single lidar over a finite time window (e.g. ten minutes) can have its own sub-structure (figure **??**). The distributions in this case can display non-normal shapes as well as limited shifts in the mean and variance compared to the ensemble distribution. For example, if only one or two convective plumes move over the instrument, there may be multi-modality based on the strength of the vertical velocity of the plumes. Over long enough times, the instrument encounters more and more turbulent structures and the error will converges toward an ensemble distribution (figure **??**). In light of the selective sampling, caution should be exercised in assuming that the ensemble error distributions presented here can be used to represent the distributions of error in a specific time series of measurements.

Though the error magnitudes are not generally large, the behavior is far from uniform and exhibits strong dependence on the flow itself, even with respect to height within the same stability regime. The mechanisms driving the observed trends in error are broken down in depth in section **??**.

2.2 Ten-minute time averaged velocities

Time averaging is often used to filter out random error 'noise' in the raw measurements output with each beam update. Common averaging intervals may be over two, ten, or even thirty minutes, with experimental evaluations of the system accuracy often reported in terms of the ten-minute average in the wind energy context. As with the error in the high(er) frequency wind measurements, we characterize the error distribution of the ten-minute averaged measurements (figure 14).

Velocity component observations are averaged over the ten-minute simulation span and compared to the time-averaged truth references. The wind speed and direction are not averaged directly but re-computed from the time-averaged wind components (equation 17) so that they correspond to a vector average of the wind. Wainwright et al. (2014) and Gasch et al. (2019) distinguish the 'scalar' average from this kind of 'vector' average while more detailed analysis comparing the averages have been undertaken by Clive (2008) and Rosenbusch et al. (2021). We omit time-averaged vertical velocity error here. Each distribution in the ten-minute average consists of an ensemble of a total of 180 values (ensemble and offset angles).

Statistical moments as in figure 11, but error distributions for the 10-minute averages.

Under quasi-stationary conditions, the notions of pointwise and volume-averaged truth start to converge to a general spatio-temporal average, which is reflected in the merging of the two error distribution metrics. The correspondence suggests that field studies comparing against time-averaged 'point' tower measurements can effectively reflect the error with respect to the volume-average as well. The overall error magnitudes found by the virtual lidar are consistent with those in field deployments of lidar compared against tower measurements. In select, flat conditions typical mean discrepancies in the range ±0.2 m/s with standard deviations of 0.20 m/s (Courtney et al., 2008) have been reported, which encompass all but the more extreme errors in the strong convection case. The measurement error which serves to help explain the mechanisms at work and interpret the results of the virtual ten-minute averaged wind speeds have mean errors within $\pm 0.2 m/s$ with standard deviation $< 0.3 m/s$ and wind direction have mean error bias within 2° and standard deviations in 2.5° except for in the strongly convective case where it can reach up to 12°measurements.

~~Many of the qualitative trends identified in the raw, 1 Hz measurement error persist in this averaged assessment; the ordering of relative error between stability conditions and their respective height trends are similar to the previous section. While respecting these general trends, the form of the moment curves shift a little compared to the original distribution, e.g. the curvature of the standard deviation with height.~~

~~The major benefit of the time average lies in the marked reduction (by a factor of around 5) of the error standard deviation across cases and heights. The erroneous rotation in the strong CBL wind direction mean remains although the time average lessens the over-estimation bias in the wind speed. The distribution shapes in the ten-minute average also grow closer to a normal distribution shape.~~

3 ~~Analysis of error mechanisms~~

The following analysis systematically addresses how turbulent variations induce error in the wind reconstruction and how that error propagates into derived quantities. Much of the analysis presented in this section is quite general and applies to any DBS reconstruction of the form ~~in equation~~ of Eq. 8 and in any flow condition. The approach can be extended to different scan types as well in decomposing their error.

Two elements directly introduce error into the observation model: the application of the ~~range gate weighting function~~ RWF in the radial velocity measurement and the assumption of horizontal ~~homogeneity~~ uniformity in the reconstruction. Using a random variable model, we identify the contributions of the RWF and ~~homogeneity violations~~ horizontal velocity variations to the error in the ~~wind component reconstructions. Accumulation time~~ wind-component reconstructions. Duration of the scan cycle and time-staggering of the beams are not ~~addressed. The behaviors exhibited in the virtual lidar data are tied back to the separate elements based on the character of the flow regime~~exlicitly addressed in the error model, though they are included in the implementation of the virtual instrument.

~~Values computed using~~ Quantities derived from the estimated wind components can take on their own, non-trivial error behavior. Natural derived quantities that are often computed from lidar data include horizontal wind speed and direction and time-averaged winds. We characterize the error in wind speed and direction in terms of the u and v error distributions and ~~examine its dependence on the background wind speed and direction. A time average is also a function acting on the raw velocity data and we trace and quantify its expected and observed effect~~ trace the expected effect of time averaging on the error distributions.

~~Finally, an empirical comparison is made between the error in the different Windcube vertical velocity reconstruction techniques and the direct measurement made by the vertical beam.~~

2.0.1 Wind-component reconstruction

2.1 ~~Random variable model of turbulent variation in wind component error~~

~~Decomposition of wind component error under the weak convection case, as in figure ??.~~

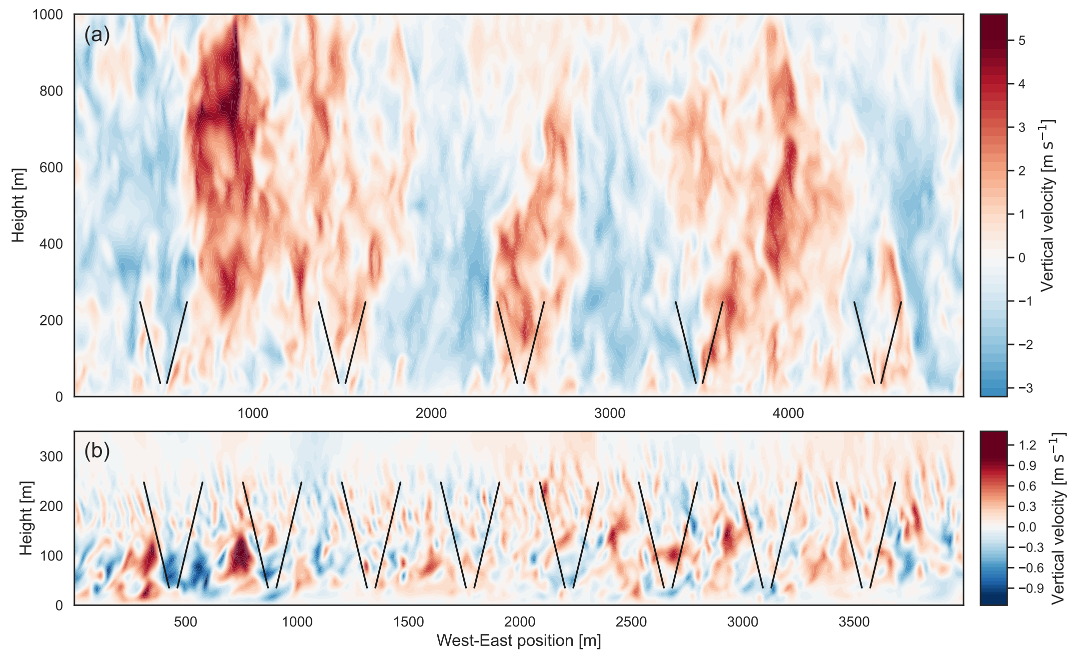

Figure 4. ~~Decomposition~~ Instantaneous slice of ~~error for each wind component in~~ vertical velocity across the ~~strong convective stability case. The mean and variance are partitioned according to equations 12-15 into contributions from perturbations~~ west-east plane in ~~horizontal~~ (~~u', v'~~a) the strong CBL and ~~vertical~~ (~~w'~~b) ~~velocities and~~ the ~~RWF measurement (r')~~ stable BL. ~~Only the data from virtual lidar aligned with the LES U, V axes are used.~~ The ~~sum of the plotted components~~ WindcubeV2 scan geometry is ~~given~~ shown for reference by the beams in ~~grey~~black.~~Discrepancy in the variance between the full model and the sum of terms is due to omitted covariance terms.~~

~~Decomposition of wind component error under the stable case. as in figure ??.~~

~~To break down the driving sources of error in the reconstruction of the velocity components, we~~ We start by deriving the form of the error in the reconstructed velocity components. The formulation allows the contribution to the error due to the turbulent variations to be explicitly delineated and tracked. For a fixed height, let $\boldsymbol{U} = (U, V, W)^T$ be the mean velocity across the scan volume, i.e. the volume-averaged truth, and assume that it is constant through the ~~five second~~ 5-s scan duration. (Different notions of the volume average could be used here, e.g. the two- or four-point average over the beam locations, but the disk seems the most useful average representation to measure). Each angled beam samples a perturbed velocity, ~~$\boldsymbol{u}_{E,W,N,S} = \boldsymbol{U} + \boldsymbol{u}'_{E,W,N,S}$~~ $\boldsymbol{u}_{E,W,N,S}(t) = \boldsymbol{U} + \boldsymbol{u}''_{E,W,N,S}(t)$, where the subscript denotes the cardinal direction of the beam azimuthal direction. The measurement of the projection of the ~~perturbed,~~ point velocity is subject to an additional perturbation, $r_{E,W,N,S}$, due to the ~~range gate weighting function. Then~~RWF. Then, the radial velocity measured by the beam pointed east, for example, is given by:

$$u_E = \cos(\phi)(U + u'_E) + \sin(\phi)(W + w'_E) + r_E$$

in Eq. 10.

$$v_{r,E} = \cos(\phi)(U + u''_E) + \sin(\phi)(W + w''_E) + r_E \qquad (10)$$

Carrying the forms through the reconstruction (equation Eq. 8), the error in the wind components is given by the difference with the volume-averaged value, $\boldsymbol{U}$. (This analysis is similar to that of Newman et al. (2016), which extends the derivation to turbulent variances). For the horizontal u and v components, the resulting representation of the error is given in equations ?? and ??. The vertical velocity error form depends on whether the wind-direction weighting is used; we limit our error model analysis to the equally weighted version (equation ??). Eq. 11).

$$u\boldsymbol{u}_{err} = u_{lidar} - U\boldsymbol{u}_l - \boldsymbol{U} = \frac{1}{2}(u'_E + u'_W) + \tan(\phi)(w'_E - w'_W) + \sec(\phi)(r_E - r_W) v_{err} = v_{lidar} - V = \frac{1}{2}(v'_N + v'_S) + \tan(\phi)(w'_N - w \qquad (11)$$

In a perfectly horizontally homogeneous uniform wind field, the velocity perturbation values all individually vanish (i.e. not due to cancellations). However, even in that perfectly horizontally homogenous uniform case, a non-linear vertical profile can still induce nonzero non-zero error through the RWF. Further, in

In the presence of turbulence in the flow, homogeneity is violated and the the velocity over the scan volume is no longer uniform and the beams sample perturbed variations, violating the assumption underlying the exact reconstruction. The perturbation values may be regarded as random variables with distributions resulting from the character of the atmospheric variations and the lidar scan geometry . (Fig. 4). Under this model, spatial trends in the background flow would be expressed in shifted perturbation mean values at the respective beam locations. The error formulation defines how the inhomogenieties turbulent variations in separate wind components and effects of the RWF RWF effects combine to produce the total error.

As functions of the random perturbations, the wind component errors are themselves random variables. The mean, μ, and variance, σ^2, of the error distributions can be expressed in terms of the perturbation distributions through algebra of random variables (Zwillinger and Kokoska, 2000). The mean of the error distribution describes offsets, or biases, in the error; it represents how quantities are consistently over- or under-estimated. The variance of the error describes the spread in the error values; it reflects the magnitude of errors on top of any systematic, mean bias.

The mean operator is linear and directly decomposes the overall error mean into constituent parts for the horizontal (equation Eq. 12) and vertical (equation Eq. 13) wind components.

$$\mu(u_{err}) = \frac{1}{2}[\mu(u'_E)+\mu(u'_W)]\frac{1}{2}[\mu(u''_E)+\mu(u''_W)] + \frac{\tan(\phi)}{2}[\mu(w'_E)-\mu(w'_W)]\frac{\tan(\phi)}{2}[\mu(w''_E)-\mu(w''_W)] + \frac{\sec(\phi)}{2}[\mu(r_E)-\mu(r_W)] \tag{12}$$

$$\mu(w_{err}) = \frac{1}{2}[\mu(w'_E)+\mu(w'_W)+\mu(w'_N)+\mu(w'_S)]\frac{1}{2}[\mu(w''_E)+\mu(w''_W)+\mu(w''_N)+\mu(w''_S)] + \frac{\cot(\phi)}{2}[\mu(u'_E)-\mu(u'_W)+\mu(u'_N)-\mu(u'_S)] \\ + \frac{\csc(\phi)}{2}[\mu(r_E)+\mu(r_W)+\mu(r_N)+\mu(r_S)] \tag{13}$$

The variance (σ^2) can also be decomposed into a linear combination of constituent terms, but introduces covariance terms (equations 14 - Eq. 14 and 15). (The variance is preferred here to the standard deviation (σ) reported in section 3 so that the contributions are additive , (i.e. no square root). We do not explicitly expand the covariance terms, which quantify correlations between the perturbations.

$$\sigma^2(u_{err}) = \frac{1}{4}[\sigma^2(u'_E)+\sigma^2(u'_W)]\frac{1}{4}[\sigma^2(u''_E)+\sigma^2(u''_W)] + \frac{\tan^2(\phi)}{4}[\sigma^2(w'_E)+\sigma^2(w'_W)]\frac{\tan^2(\phi)}{4}[\sigma^2(w''_E)+\sigma^2(w''_W)] + \frac{\sec^2(\phi)}{4}[\sigma^2(r_E) \tag{14}$$

$$\sigma^2(w_{err}) = \frac{1}{4}[\sigma^2(w'_E)+\mu(w'_W)+\sigma^2(w'_N)+\sigma^2(w'_S)]\frac{1}{4}[\sigma^2(w''_E)+\mu(w''_W)+\sigma^2(w''_N)+\sigma^2(w''_S)] + \frac{\cot^2(\phi)}{4}[\sigma^2(u'_E)+\sigma^2(u'_W)+\sigma^2(u \\ + \frac{\csc^2(\phi)}{4}[\sigma^2(r_E)+\sigma^2(r_W)+\sigma^2(r_N)+\sigma^2(r_S)] + \text{covariance terms} \tag{15}$$

As before, the mean of the error distribution describes offsets, or biases, in the error; it represents how quantities are consistently over- or underestimated. The variance of the error describes the spread in the error values; it reflects the expected magnitude of errors on top of any systematic, mean bias.

The relative weighting of the perturbations is controlled by the scan cone elevation angle from the horizon, ϕ (figure Fig. 1), and describe describes the result of the relative projection of the perturbations on the beam. For the WindcubeV2 cone angle, $\tan\phi \approx 1.88$, so that the vertical velocity perturbations are weighted almost twice as heavily as the horizontal velocity perturbations. The radial velocity perturbations are similarly heavily weighted, with $\sec\phi \approx 2.1$. The asymmetric weighting is further exacerbated in the variance, which uses the squares of these values. The cone angle also

Along with the relative weights, the elevation angle controls the spatial separation of the beamsand can thus implicitly influence , thus implicitly influencing the distributions of the perturbations themselves. The beam separation can be of particular importance in the presence of background spatial variation in the flow , potentially producing error bias. in which larger separation can induce a greater mean error, as explored in terms of linear variations of vertical velocity in Bingöl et al. (2009) . Teschke and Lehmann (2017) derived a shallow elevation angle ($\phi \approx 35.26°$) as minimizing error in the reconstruction in the presence of noisy radial velocity measurements in locally homogeneous conditions. The magnitude of the radial velocity variances are not constant, instead varying with the elevation angle and the resulting projection of the turbulent fluctuations onto the beam.

More off-vertical beams may be used with a linear least-squares reconstruction process (Newsom et al., 2015), of which the DBS scan presented in this study is a special case. The beams are usually preferred to be symmetrically spaced to cancel potential systematic biases in the u and v reconstructions (Sathe et al., 2015; Teschke and Lehmann, 2017).

The virtual lidar model uses the LES to indirectly predict the perturbation distributions and the complex ways in which the perturbations can be interrelated inter-related with each other and with respect to the volume averages. Random variable theory can then be used to describe the propagation of uncertainty into the error from the attributes of the perturbation distributions. The virtual lidar and LES data are used to compute the terms in the decomposition of the error mean (equations 12 and 13) and variance (equations 14-15) over each of the stability cases (figures ??, ??, ??). The error mean in the overall model should be equal to the sum of the decomposed terms. The variance decomposition omits the covariance terms, the combined effect of which accounts for the remaining gap between the sum and the full model error. The explicitly tracked terms explain how much of the total error variability can be ascribed to each set of (weighted) perturbations. In the following sections, the behavior of the decomposed wind component errors in the test cases are explored.

2.1 Effects of range gate weighting

2.0.1 Effects of range-gate weighting

The size of discrepancies in the radial velocity measurement due to weighting by the RWF may be analytically bound. The bound serves to illuminate the conditions under which the perturbations from the point value can become large.

Assume any RWF, $\rho(s)$, is a non-negative, symmetric function which even function that monotonically decays as $s \to \pm\infty$ and satisfies $\int_{-\infty}^{\infty} \rho(s) = 1$. Let $v_r(r)$ be the radial velocity profile along the beam and $R > 0$ a threshold distance from the target, r_0. Then under the RWF model, the size of the discrepancy between the range-gate-weighted measurement, $\overline{v}_r(r_0)$, and the actual, pointwise radial velocity, $v_r(r_0)$, is constrained in equation Eq. 16 (derivation in appendix Appendix C).

$$|\,\overline{v}_r(r_0) - v_r(r_0)| \leq \left[1 - \int\limits_{|s|\leq R} \rho(s)ds\right]\left(\max_{s>|R|} |v_r(r_0+s)| + |v_r(r_0)|\right) + \left[\frac{1}{2}\int\limits_{|s|\leq R} \rho(s)s^2 ds\right] |v_r''(r_0+\xi_*)| \tag{16}$$

The bounding terms can be forced to be small by selecting R to manipulate the coefficients. The magnitude of the radial velocities in the atmosphere can practically be expected to be finitely bound. Taking R to be large drives the integral of $\rho(s)$ to one and thus the first term to zero. The second term does the opposite: the coefficient grows rapidly with R and is small for small R. The tension between the requirements picks out the conditions which that allow for potentially large deviations in the weighted measurement from the true point value.

Radial velocity profiles with constant gradient do not incur error in the RWF application; symmetry leads the linear contributions to cancel. Indeed, visual inspection confirms this behavior in regions of constant gradient about r_0, which incur only small discrepancies (figure 2(Fig. 2b,c,d)). The competition between the remaining bounding terms (equation Eq. 16) places requirements on the radial velocity behavior itself; in the absence of large curvature in the radial velocity profile ($|v_r''|$ small), the error can be expected to be negligible. Data collected by the virtual lidar affirms such behavior in practice, showing the largest misrepresentations The largest misrepresentations appear in areas with sharp bends in the radial velocity profile (figure Fig. 2).

The impact of the RWF on the total error in the test cases is generally limited compared to that of the horizontal inhomogeneities, except where the RWF interacts with the surface layer. Its contribution (r') to bias and variability of the wind component error is separated in each stability case according to the model in the previous section. In the convective regimes, the proportion of error variance from RWF perturbations is negligible across heights and wind components (figures **??**,**??**). The relative impact is larger in the stable case, especially for vertical velocity , though the absolute magnitude is still small (figure **??**). The most prominent influence of the RWF is near the surface layer (due to strong shear) and manifests as a negative shift in the mean error in the horizontal velocities. The weak CBL and stable BL, with strong winds and surface shear, exhibit the effect most strongly. Assuming a logarithmic profile, a large second derivative is to be expected close to the surface, which our analysis suggests is conducive to larger error in the radial velocity measurement. The logarithmic curve in u has a consistent shape which induces an repeated underestimates by the RWF, $r_E < 0$. Accounting for the negative projection of u on the west beam, $r_W > 0$ so that the difference $r_E - r_W$ is systematically negative, leading to a negative bias in u measurements. It follows that if the the mean winds were easterly, the sign of the bias would also flip ($r_E - r_W > 0$) so that the magnitude of the wind component would still be underestimated. Our findings linking the effect of shear on lidar error due to the RWF echo those found by Courtney et al. (2014), and would be applicable in other strong-shear regions of the atmosphere such as at the top of a wind turbine wake.

2.0.2 Horizontal uniformity violations

2.1 Horizontal homogeneity violations

Violations of horizontal homogeneity Variations in the velocity across the scan volume are directly represented in the error model by the velocity perturbations in the wind component errors (equations **??**,**??**,**??**Eq. 11). Horizontal variations may also be reflected in the radial velocity along the beam and are assumed to be encapsulated in the treatment of the RWF. The perturbations in the velocity around the scan radius occur due to heterogeneity on variations over a larger spatial scale than those along a single beam, potentially permitting larger turbulent structures with larger variations.

To describe the error due to the perturbation terms, we consider what they represent and how they relate to the turbulence in the flow. In the lidar model, the velocity perturbations (u'_{beam} $\mathbf{u}''_{E,W,N,S}$) are taken with respect to the average over the scan volume; they are a kind of turbulent fluctuation under the high-pass filter based on the scale of the scan volume (i.e. about 42 m across at the bottom range gate and 255 m at the top), filtering out turbulence at the larger scales). The variance of the perturbations($\sigma^2(u'_{beam})$), , $\sigma^2(u''_{E,W,N,S})$, which determines their magnitude, is a filtered fraction of the full turbulent Reynolds velocity variance(e. g. $\overline{u'u'}$). full-turbulence velocity variance, $\overline{u'^2}$. As the size of the scan volume increases, the volume average approaches an ensemble mean so that the perturbations are Reynolds fluctuationsbecome Reynolds fluctuations, u'. The variance expected in the lidar perturbations is determined by the proportion of turbulent variances in each direction above the filter scale(figure 10), with the full turbulent variance constituting a 'cap ' cap on the total possible variance.

~~(a)(b)Instantaneous slice of vertical velocity across the west-east plane in (a) the strong CBL and (b) the stable BL. The WindcubeV2 scan geometry is shown for reference by the beams in black.~~

It is tempting, with usual conventions about turbulent perturbations, to assume that the lidar velocity perturbations will have zero mean and identical distributions at each of the beam locations. Under these assumptions, the mean error due to the ~~the~~ horizontal homogeneity violations would be zero. However, the ~~volume average mean~~ volume-average over the disk is neither the direct mean of the beam velocities nor is it the turbulent ensemble mean. The velocity perturbations can produce a non-zero mean because of consistently occurring spatial patterns in how the velocities vary at the edges of the scan volume with respect to the average velocity over that volume. The spatial structures at play in the LES cases with respect to the lidar scan volume can be seen in the ~~cross-sections in figure ??.~~ cross sections in Fig. 4. If the turbulent structures are small enough and the scan volume large enough, then the volume average ~~does approach the~~ approaches a turbulent ensemble mean ~~and~~ so that the beams sample ~~separated,~~ independent turbulent fluctuations. Under such conditions, the assumption of zero mean and identically distributed perturbations at each beam are appropriate. ~~However, when there are~~ When coherent turbulent structures ~~on the order of the~~ occur that fill the scan volume, however, the volume average no longer represents a turbulent ensemble mean. Without dissecting the mechanics more closely, we simply note that large coherent ~~structure~~ structures, like turbulent plumes characteristic of the convective boundary layer, can induce repeated, non-symmetric patterns in the relative perturbations of the beams, leading to non-zero means.

~~We can now see how these behaviors play out in the virtual lidar data. Using the derived forms (equations 12-15), the contributions from the horizontal (u', v')~~

2.0.1 Secondary effect on derived quantities: wind speed and direction

An common representation of the observed horizontal wind vector is as a direction, Θ (meteorological convention), and magnitude, $|\boldsymbol{U}_h|$ (Cariou and Boquet, 2010). The WindcubeV2 internally computes and reports these derived quantities by solving for them from the reconstructed velocity components (Eq. 17).

$$|\boldsymbol{u}_{h,l}| = \sqrt{u_l^2 + v_l^2}, \qquad \Theta_l = \arctan 2(-u_l, -v_l) \tag{17}$$

The wind direction, placed in the appropriate quadrant, is compactly represented by the two-argument inverse tangent (the sign and order of the arguments follow meteorological conventions with the angle measuring the wind source clockwise from north). Wind direction error is bound in the interval $(-180°, 180°)$ where positive values indicate the lidar reading an angle clockwise from truth and negative values an angle counter-clockwise from truth (Fig. 5).

The derived values do not inherit the error from the wind-component errors directly; rather the quantities should be thought of as functions of the u and ~~vertical (w') perturbations to~~ v errors treated earlier, taking on their own distinct, related error distribution behavior. As non-linear functions of u and v, the error in the wind speed and direction do not drop out directly.

We may expand the lidar-sensed horizontal wind speed (Eq. 17) about the volume-averaged wind speed, using $\mathbf{u}_{h,l} = \mathbf{U}_h + \mathbf{u}_{h,err}$. (The error compared to a pointwise reference is better served by expanding both about an average reference). We assume the errors in u and v to be small and take a second-order Taylor-series expansion of the square root. Then we obtain Eq. 34 (by

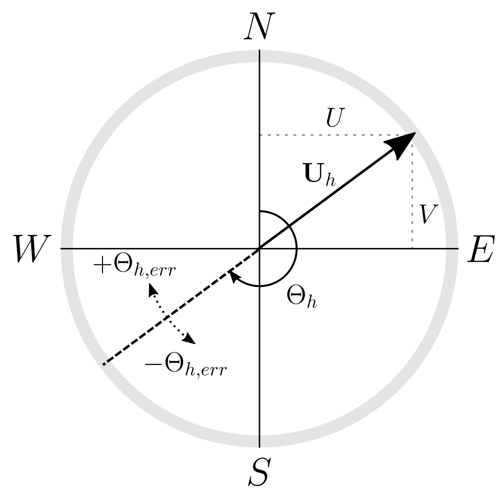

Figure 5. Conventions used for the horizontal wind vector direction and signs of the wind-direction error.

mathematical analog to the Reynolds decomposition, echoing Rosenbusch et al. (2021)),

$$|\boldsymbol{U}_h|_{err} = |\boldsymbol{u}_{h,l}| - |\boldsymbol{U}_h| \approx \frac{U}{|\boldsymbol{U}_h|} u_{err} + \frac{V}{|\boldsymbol{U}_h|} v_{err} + \frac{\left(\frac{U}{|\mathbf{U}_h|} v_{err} - \frac{V}{|\mathbf{U}_h|} u_{err}\right)^2}{2|\mathbf{U}_h|}$$
$$= \frac{\boldsymbol{U}_h}{|\boldsymbol{U}_h|} \cdot \boldsymbol{u}_{h,err} + \frac{\left| \left(\frac{U}{|\mathbf{U}_h|}, \frac{V}{|\mathbf{U}_h|}, 0 \right)^T \times (u_{err}, v_{err}, 0)^T \right|^2}{2|\boldsymbol{U}_h|} \tag{18}$$

We can explicitly find a theoretical mean of the wind speed error and simplify by assuming the u and v error random variables have a mean of zero (Appendix C) and are uncorrelated.

$$\mu(|\boldsymbol{U}_h|_{err}) \approx \frac{\cos^2\Theta\sigma^2(u_{err}) + \sin^2\Theta\sigma^2(v_{err})}{2|\boldsymbol{U}_h|} \tag{19}$$

The persisting, strictly positive term implies we should expect a systematic positive bias in the wind speed error, i.e. that the wind speed will be over-estimated more than under-estimated. Note that this does not mean the total error (Eq. 34) is always positive — the weighted component errors can cause it to be negative — but that on average the reported wind speed will be greater than that of the actual volume-averaged horizontal wind. The expected magnitude of the bias is proportional to the variance of the error in the u and v measurements and inversely proportional to the volume-averaged wind speed.

Without explicitly computing the variance, we can estimate the magnitude of the wind speed error. Based on the leading order terms, the error should generally be on the order of the individual component errors (i.e. their standard deviation), though the bias term has the potential to become more prominent in adverse conditions (large u, v errors, slow winds).

Now consider the wind direction error. To simplify the analysis, we set aside the quadrant correction and consider just the traditional inverse tangent function to find the angle in $[-90°, 90°]$. Then the wind direction error, in radians, is the difference,

$$\Theta_{err} = \Theta_l - \Theta = \arctan\left(\frac{u_l}{v_l}\right) - \arctan\left(\frac{U}{V}\right) \tag{20}$$

As with the wind speed, the mean value does not directly cancel. Applying the difference identity for $\arctan$ and simplifying,

$$\Theta_{err} = \arctan\left(\frac{V u_{err} - U v_{err}}{|\boldsymbol{U}_h|^2 + V v_{err} + U u_{err}}\right) \tag{21}$$

The form in Eq. 34 may be turned into a looser bound that is simpler to interpret. The derivative of $\arctan$ is continuous and bound above by one so that we may bound, $|\arctan(x)| \leq |x|$. For the error,

$$|\Theta_{err}| \leq \left|\frac{\frac{V}{|\boldsymbol{U}_h|} u_{err} - \frac{U}{|\boldsymbol{U}_h|} v_{err}}{|\boldsymbol{U}_h| + v_{err} + u_{err}}\right| \tag{22}$$

The bound is tighter the smaller the error and the sign of the bounding expression should match that of the error creating an "envelope" for the error. From the error approximation, if we again assume the reconstruction of u and v to have zero mean error and similar variances, then the wind direction mean error should also be zero (Appendix C). Without explicitly computing the variance, we estimate the bound on the wind direction magnitude to be (in radians) roughly proportional to the standard deviation of the u and v errors over the volume-averaged wind speed.

2.0.2 Reducing error through time averaging

Time averaging is a tool used to reduce the variation of the error in the raw, high-frequency measurements made by the lidar, leaving a more reliable mean measurement. Under conditions in which the background flow continues to evolve in time, the utility of time averaging must be weighed against the length of the interval during which quasi-stationary conditions exist and the sacrificed resolution of shorter time-scale dynamics. Making an informed assessment of an appropriate time-window length rests on quantifying the expectation of the improvement of the measurement accuracy.

The lidar error varies along with the "random" turbulence in the flow, which we have reflected by describing the error as a random variable that is drawn from a distribution dependent on the character of the turbulence and the lidar scan geometry. Here, we consider how time averaging acts on the error distribution of the raw 1-Hz measurements.

First, we consider a time average (arithmetic mean) performed over the wind components (which is mathematically equivalent to averaging over the beam radial velocities when the reconstruction is linear as in Eq. 8). The following derivations are given in terms of u, but hold identically for all of the wind components (u, v, w). Let T be the length of time window and suppose the instrument samples at a constant interval of τ_s (every second for the WindcubeV2). Then there are $T_s = \lfloor T/\tau_s \rfloor$ samples in the discrete time-average over the window. Expanding the lidar estimate of the time-averaged truth, $\overline{U}^T$, the error in the time-averaged measurement emerges by linearity to be the arithmetic mean of the sample errors (Eq. 23).

$$\overline{u}^T_{err} = \frac{1}{T_s}\sum_{i=1}^{T_s} u_{err}(t_i) \tag{23}$$

That is, the error in the time-averaged measurement can be expressed as the sum of (scaled) random variables drawn from the distribution of the constituent 1-Hz errors. Again using linearity, the mean of the time-averaged error distribution, $\overline{u}^T_{err}$, is equal to the ~~wind component errors are delineated for each test case (figures ??, ??,~~ mean of the original sample errors, $\mu(\overline{u}^T_{err}) = \mu(u_{err})$; i.e. time averaging does not change the mean ensemble error of the wind components.

The primary effect of the time average on the velocity components is to reduce the width of the error distribution, i.e. the typical magnitude of the errors. The variance of the arithmetic mean of independent, identically distributed random variables is well-known (Zwillinger and Kokoska, 2000); given the variance of the original, un-averaged random variable, $\sigma^2(u_{err})$, the variance of the mean over N samples is $\frac{1}{N}\sigma^2(u_{err})$. In a time series, however, the samples cannot simply be treated as independent because subsequent samples can be highly correlated. The correlated data contributes less independent information which results in a lower effective sample size in terms of reducing the variance. Assuming a finite integral scale (decorrelation time), τ_c, in the error time series, the variance of the error in the time-averaged wind component is expected to converge according to Eq. 24 for large enough T (Lumley and Panofsky, 1964).

$$\sigma^2(\overline{u}^T_{err}) \approx \frac{2\tau_c\sigma^2(u_{err})}{T} \approx \frac{2(\tau_c/\tau_s)\sigma^2(u_{err})}{T_s} \tag{24}$$

Then the reduction factor for the error standard deviation scales proportionally to $T^{-1/2}$ (Eq. 34).

$$\frac{\sigma(\overline{u}^T_{err})}{\sigma(u_{err})} \approx \sqrt{\frac{2(\tau_c)}{T}} \tag{25}$$

Under this analysis, the marginal utility of longer time average in terms of reducing the standard deviation shrinks rapidly; just four independent samples are needed to halve the standard deviation but 100 are needed to bring the standard deviation to a tenth of its original value.

In the horizontal wind speed and direction, the time-average can be computed either from the time-averaged vector components (a vector average) or directly over the scalar speed and direction computed each second (a scalar average) (Eq. 26-29). In general, these quantities are not equal; the scalar-averaged wind speed is known to systematically exceed the vector-average (Courtney et al., 2014; Clive, 2008; Rosenbusch et al., 2021).

$$\overline{|\mathbf{u}_h|}^{T,vec} = \left|\overline{\mathbf{u}}_h^T\right| = \left[(\overline{u}^T)^2 + (\overline{v}^T)^2\right]^{1/2} \tag{26}$$

$$\overline{|\mathbf{u}_h|}^{T,sca} = \overline{|\boldsymbol{u}_h|}^T = \overline{\left[u^2 + v^2\right]^{1/2}}^T \tag{27}$$

$$\overline{\Theta}^{T,vec} = \arctan 2(-\overline{u}^T, -\overline{v}^T) \tag{28}$$

$$\overline{\Theta}^{T,sca} = \overline{\arctan 2(-u, -v)}^T \tag{29}$$

The average of the scalar quantities is again a linear operator so that, as with the velocity components, no change is expected in the means of the scalar time-averaged measurement errors compared to the raw 1-Hz error. The decay of the standard deviations of the errors both should mirror that of the wind components as well because the decorrelation time is similar.

For the vector-averaged quantities, we determine the effect on the wind direction and speed error by carrying the changes in the time-averaged wind-component error distributions through into the error forms (Eq. 34 and 34). Assume that the volume-averaged wind speed does not change significantly over the averaging window so that it may be treated as constant. Because we identified the magnitude of the wind speed and direction error to be proportional to the u and ??) v errors, we also expect the variances to decay with the same rate as the wind components. The mean of the vector-averaged wind direction error should experience negligible change under the time average because it arises primarily from the component error means which remain the same. In the mean error of the vector-averaged wind speed (Eq. 34), the first terms in the error depend only on the component means and remain unaltered. The positive bias term, however, is proportional to the u and v error variances and is accordingly scaled by a factor $\propto T^{-1}$. Therefore, we expect the vector averaged wind speed error to experience an improvement not only in reducing the magnitudes of the error but also in the mitigation of the positive bias, which decays to zero in the limit, $T \to \infty$. For the most part, the error mean biases can be attributed to RWF effects and the velocity perturbation terms do have close to zero mean

The discrepancy between the scalar- and vector-averaged lidar quantities arises from the persistence of the positive bias term in the scalar average and its corresponding decay in the vector average. By mathematical analog of a Reynolds decomposition to the error fluctuation on the volume-average winds, the wind speed error derivation (Eq. 34) reflects a discrepancy between any scalar and vector averages of wind measurements. The literature has noted the inflation of scalar-averaged wind speeds compared to the vector-average, which has consequences for the comparison of time-averaged lidar measurements to the pointwise, scalar-averaged measurements made by cup anemometers. Courtney et al. (2014) performs several cross-comparisons of vector and scalar averages between lidar and point measurements while Rosenbusch et al. (2021) derives and analyzes limiting bounds for the comparison of lidar and cup measurements. We briefly re-derive the difference in the inflation for pointwise and lidar measurements.

Assume that the vector time-average acts like an ensemble Reynolds-average (as it does over a long enough time window), so that the vector time-average of the pointwise and lidar measurements both reduce to $\overline{\boldsymbol{u}}_h$. Under this assumption, the 1-Hz wind-speed bias accounts for the total difference between the scalar and vector averaged wind speed. The inflation in the scalar-averaged wind speed over the corresponding vector average is proportional to the variance of the fluctuations transverse to the mean wind in the measurements of the u and v winds (Eq. 30) (Courtney et al., 2014; Rosenbusch et al., 2021).

$$|\overline{\boldsymbol{u}}_h|^{T,sca} = |\overline{\boldsymbol{u}}_h|^{T,vec}(1+\alpha) \approx |\overline{\boldsymbol{u}}_h|^{T,vec}\left(1 + \frac{\sigma^2(r_\perp)}{2|\boldsymbol{u}_h|}\right) \tag{30}$$

The fractional inflation in the scalar average is denoted by α and $r_\perp$ is the fluctuation in the observed horizontal wind perpendicular to the mean wind direction.

Let the volume-average reference be the Reynolds-averaged wind, $\mathbf{U} = \overline{\boldsymbol{u}}$. Then the perturbations in the lidar velocities are Reynolds fluctuations ($u'' = u'$) and the lidar-perceived turbulence, $\boldsymbol{u}_{h,l} - \overline{\boldsymbol{u}}_h$ follows the derived error form (Eq. 11). We omit the RWF terms (r) to focus only on the direct turbulent fluctuations. As before, assume that the vector time-average of both the lidar and pointwise measurement approximate the Reynolds average, $\overline{\boldsymbol{u}}_l^T = \overline{\boldsymbol{u}}_p^T = \overline{\boldsymbol{u}}$. Then we recover, as in Rosenbusch et al. (2021), the inflation factors for the pointwise, α_p, and lidar-derived, but important deviations from that assumption do arise. The largest deviations from zero mean error (except for the RWF) occur in α_l, scalar averages (Eq. 31 and 32).

$$\alpha_p \approx \frac{1}{2|\overline{\mathbf{u}}_h|^3} \overline{\left| \begin{pmatrix} \overline{u} \\ \overline{v} \\ 0 \end{pmatrix} \times \begin{pmatrix} u' \\ v' \\ 0 \end{pmatrix} \right|^2} \tag{31}$$

$$\alpha_l \approx \frac{1}{2|\overline{\mathbf{u}}_h|^3} \overline{\left| \begin{pmatrix} \overline{u} \\ \overline{v} \\ 0 \end{pmatrix} \times \frac{1}{2} \begin{pmatrix} u'_E + u'_W + \tan\phi(w'_E - w'_W) + \\ v'_N + u'_S + \tan\phi(w'_N - w'_S) \\ 0 \end{pmatrix} \right|^2} \tag{32}$$

The inflation will scale with the variance of the perceived velocity fluctuations. A pointwise anemometer measurement experiences only horizontal fluctuations whereas the u and v measurements made by the lidar experience fluctuations due both horizontal and vertical velocity turbulence. In the lidar measurement, the contribution from the horizontal velocity fluctuations, which is the average over the samples at the two beam points, should be smaller than the variance of the sample at just a single point. The vertical velocity fluctuations can conversely increase the variation in the lidar-observed u and v. Analysis of the limiting cases suggests that when the vertical velocity contributions are negligible, e.g. in very stable cases, $\alpha_p \geq \alpha_l$, whereas when all components fluctuate independently and the vertical velocity variance is sufficient, e.g. in unstable conditions, $\alpha_p \leq \alpha_l$ (Rosenbusch et al., 2021). The latter condition leads to the hybrid scheme (Eq. 33) used in the internal time-averaging in the WindcubeV2.1 (earlier versions use a scalar average).

$$\overline{|\mathbf{u}_h|}^{T,hyb} = \frac{1}{3}\overline{|\mathbf{u}_h|}^{T,vec} + \frac{2}{3}\overline{|\mathbf{u}_h|}^{T,sca} \tag{33}$$

By weighting the scalar- and vector-averaged lidar measurements, the hybrid scheme scales its effective inflation factor to better represent that experienced at a point, thereby improving the bias in the lidar compared to cup measurements. The ideal weighting depends on the degree of correlation in the velocity fluctuations at the lidar beams and the impact of the vertical fluctuations, which inevitably vary with the flow conditions.

3 Virtual lidar observation error

The error incurred in any individual measurement depends on the specific realization of turbulence during the measurement and is not necessarily representative of the full variability of possible error behavior. To deduce useful information about bias and typical error magnitudes that can be generalized to other measurements in the same conditions, we focus instead on the distribution of the observation error. Each virtual instrument in the ensemble provides instances of the way the WindcubeV2

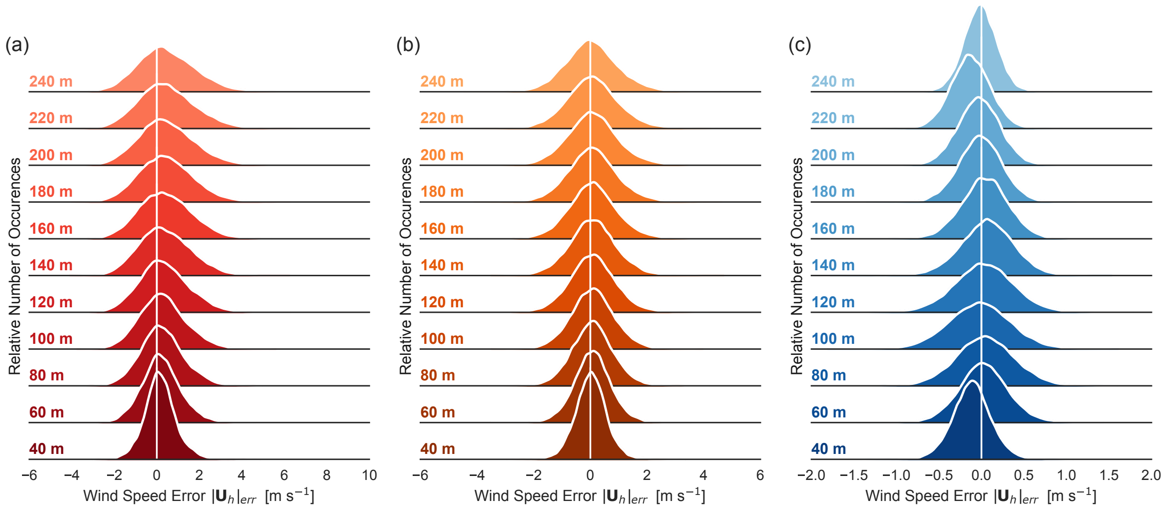

Figure 6. Kernel density estimates of the 1-Hz wind speed error distributions. Errors are computed with respect to the volume average at each height for the (a) strong CBL, (b) weak CBL, and (c) stable boundary layer (BL). Each distribution comprises 108,000 data points.

might interact with turbulent features in each flow regime, thereby sampling the error distribution. The raw 1-Hz distributions describe the error in a single measurement made by an instrument randomly dropped into each stability regime. We characterize the resulting error distributions and trends in behavior, in the raw 1-Hz and time-averaged lidar output, and deconstruct the driving mechanisms. Though the error magnitudes are not generally large, the behavior is far from uniform and exhibits strong dependence on the flow itself, even with respect to height within the same stability regime.

3.1 Raw 1-s reconstructed velocity components

A lidar reports a vertical profile of velocities each second over the duration of the simulation. Each distribution consists of 10 minutes of data combined over the 45 ensemble members and four orientation angles, giving a total of 108,000 error samples. Disaggregating by height and stability, kernel density estimates (KDEs) of the error histogram visualize the resulting distribution. Collating the KDEs into a ridgeline plot (e.g. wind speed in Fig. 6), distinct variations in the distribution center, width, and shape appear. The distribution width in particular varies heavily with stability and height. Visual inspection confirms that the distributions are well-behaved and roughly normal with one central peak.

Statistical moments serve to summarize and quantify the properties of the distributions, facilitating intercomparison and the identification of trends in the error behavior. We consider the first four moments: unbiased estimators of the mean, centered variance/standard deviation, and the adjusted Fisher–Pearson standardized moment coefficients for skewness and excess kurtosis (Zwillinger and Kokoska, 2000; Joanes and Gill, 1998). The mean, μ, represents the expected error, with non-zero values indicating a bias in the lidar observation. The centered variance, σ^2, measures the spread of the distribution about the

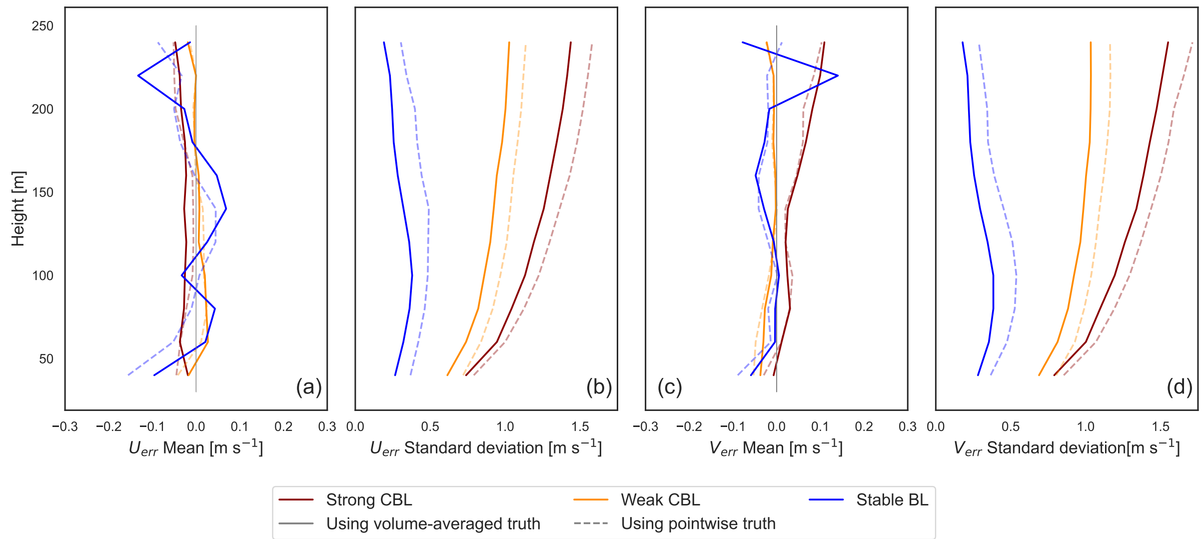

Figure 7. Mean and standard deviation of error in the u (a,b) and v (c,d) horizontal velocity components using both volume-averaged truth (solid) and pointwise "tower" truth (dashed). Stability cases are distinguished by line color.

mean, though the corresponding standard deviation, σ, can be easier to intuit as an indication of the distribution width and represents typical error magnitude in the original measurement units. For centered (zero mean) distributions, the standard deviation is comparable to the root-mean-squared-error (RMSE or RMSD) metric. The higher-order moments of skewness and kurtosis, normalized by the standard deviation, are non-dimensional descriptors of the distribution shape, namely asymmetries and decay of the tails. With a few exceptions, the metrics suggest that the distributions do not differ substantially from normal.

We start by examining the reconstructed horizontal velocity components. The skewness and kurtosis metrics suggest generally normal behavior except for the excess kurtosis (+1) indicating more slowly decaying tails, particularly near the surface. The rest of the discussion of the component errors focuses on trends in the mean and variance; see Appendix A for the first four moments for all variables.

In all cases, the distribution of the error with respect to the pointwise truth displays a larger standard deviation than the error using the volume-averaged truth (Fig. 7). With the beam measurements at the perimeter of the scan volume, the lidar reconstruction has no way to predict small-scale variations at the center of the volume where the pointwise truth resides. It can only reconstruct an average representation, and comparison with the point value incorporates additional uncertainty into the error.

In general, the mean biases are close to zero (< 0.05 $\mathrm{m\ s^{-1}}$) with just a few instances in the stable BL and at the top of the range in the strong CBL exhibiting biases up to 0.15 $\mathrm{m\ s^{-1}}$. The strong convective case consistently suffers from more significant errors, reflected in the greater error standard deviations (around 1-1.5 $\mathrm{m\ s^{-1}}$). It is followed by the weak CBL (0.5-1 $\mathrm{m\ s^{-1}}$), with the stable case being the best behaved (< 0.5 $\mathrm{m\ s^{-1}}$). In the convective cases, the error magnitudes grow

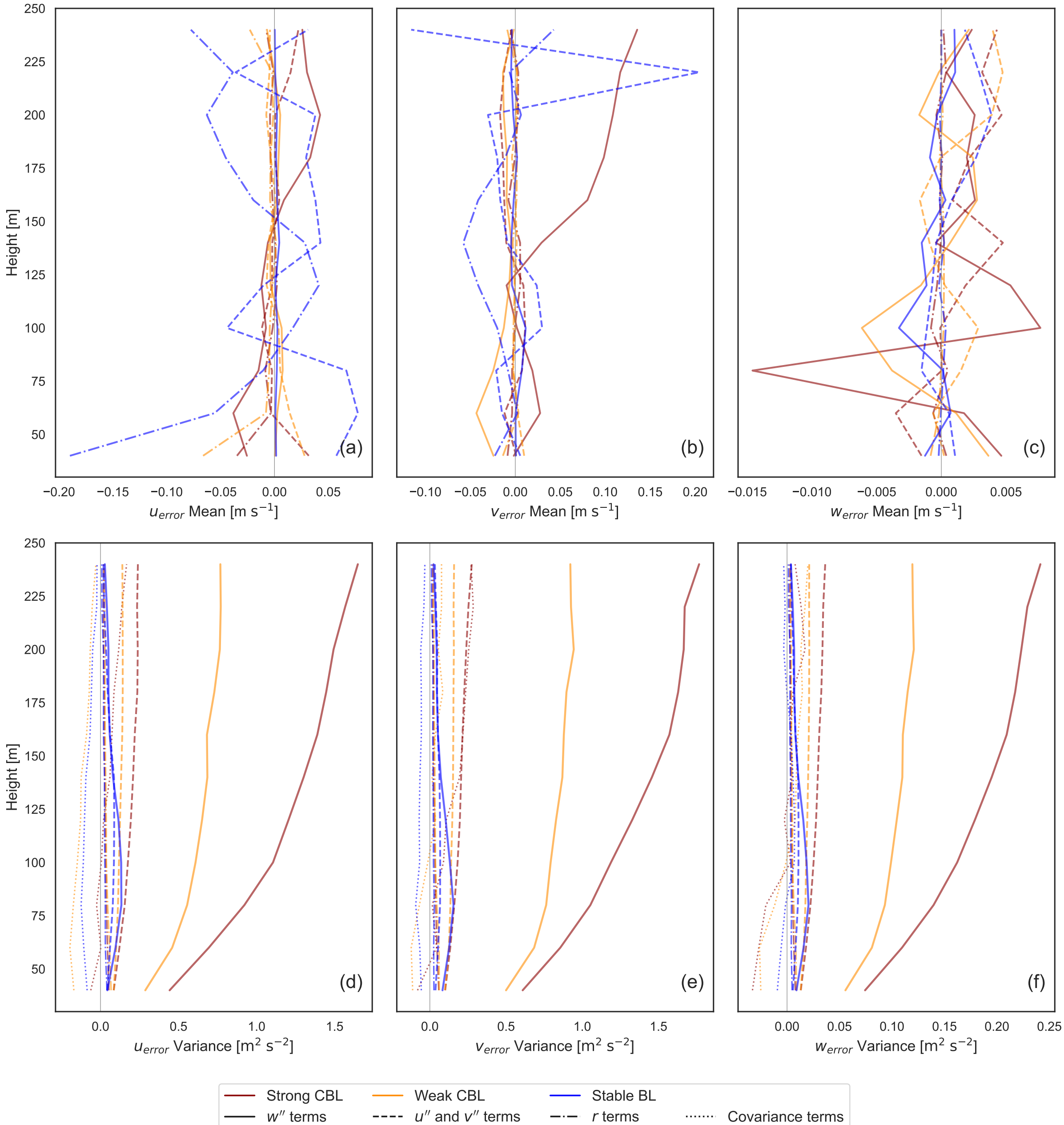

Figure 8. Contributions to the mean (a,b,c) and variance (d,e,f) of the error for each wind component, partitioned according to Eq. 12-15 into horizontal (u'', v'') and vertical (w'') velocity perturbations, RWF effects (r), and combined covariance effects.

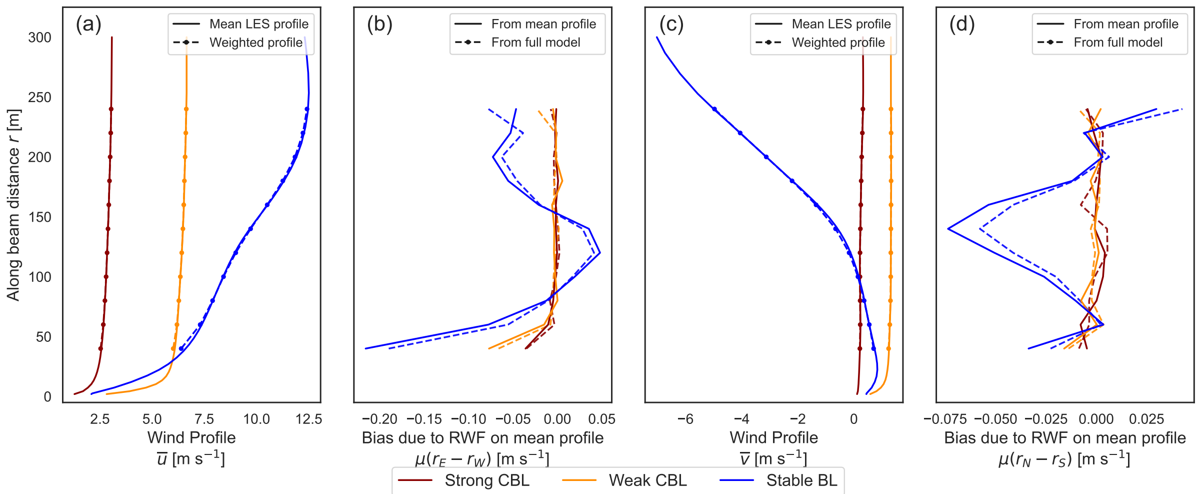

Figure 9. The mean vertical profiles of (a) $\overline{u}$ and (c) $\overline{v}$ from the LES along with the corresponding, RWF-weighted view of the profile sampled along the angled beam. (b,d) The RWF-weighting bias on the uniform, mean vertical profiles of $\overline{u}$ and $\overline{v}$ compared to the bias due to the RWF in the full virtual lidar.

consistently with height to the top of the lidar range in the middle of the boundary layer. The stable BL error peaks in the middle of the boundary layer (around 80 m). Using the derived forms for the wind component errors (Eq. 11), we delineate the roles of the perturbations in the horizontal (u'', v'') and vertical (w'') velocities and due to the RWF in the total error mean and variance (computed from the 45 virtual lidar with no offset from the LES axes) (Fig. 8).

For the most part, in homogeneous turbulence, non-zero mean biases in u and v can be attributed to RWF effects. The largest deviations from zero arising instead from velocity perturbation terms occur in the strong CBL case and stable case (Fig. 8a,b), where coherent structures large enough to span the scan volume (42-255 m) may appear. Repeated sampling across asymmetric internal-structures in convective plumes or large turbulent features above the stable BL could potentially induce small biases. In the absence of strong systematic results, however, numerical noise and the finite nature of the ensemble can also induce small apparent deviations in the model that do not meaningfully indicate bias. The bias introduced by the RWF, though also generally small (< 0.15 m s^{-1}), is considered robust since it is mechanistically supported.

The most prominent influence of the RWF is near the surface layer due to strong shear, manifesting as an under-estimate of the magnitude of the horizontal velocities. As shown for a general RWF (Eq. 16), curvature in the wind profile permits larger measurement biases from the targeted point value. In the LES test cases, the RWF contribution to the mean ensemble error corresponds to the bias of the RWF acting on the background $\overline{u}$ and $\overline{v}$ profiles (Fig. 9). The effect is most significant near the surface layer in strong shear (-0.2 m s^{-1} in the strong CBL case and stable BL case, though they do arise elsewhere. We attribute these deviations to the presence of large coherent structures on the order of the scan volume as discussed above, which agrees with the presence of the large convective plumes as well as the larger-scale structures above the boundary layer in the stable BL.) and around inflection points. Although the peak curvature of the vertical profile of the weak CBL

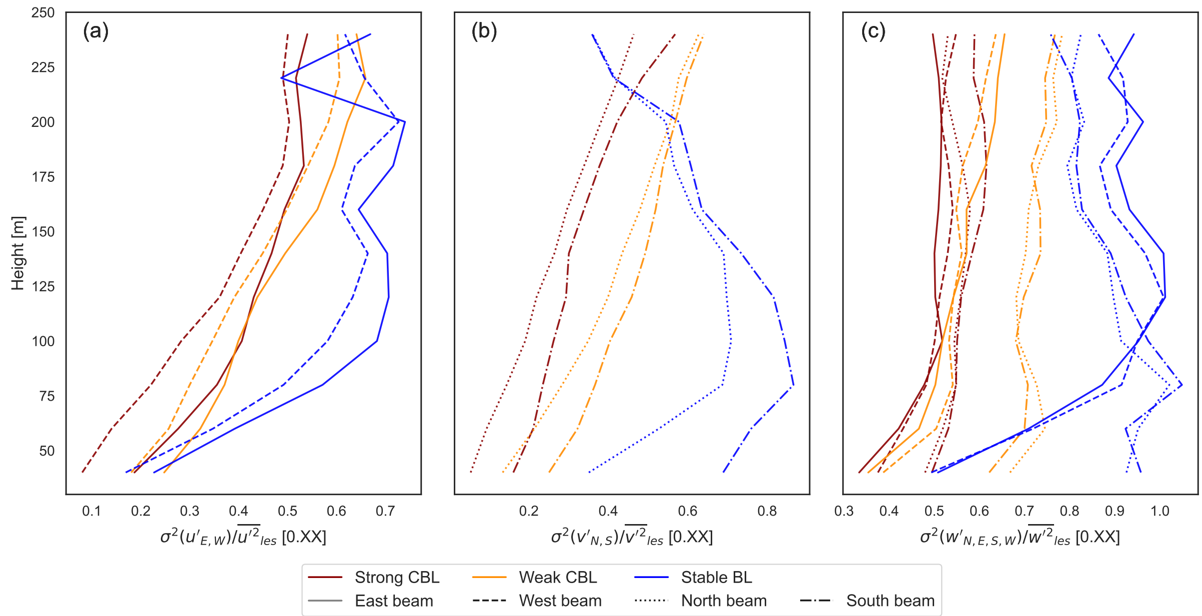

Figure 10. The proportion of the full turbulent velocity variances ($\overline{u'^2}$, $\overline{v'^2}$, $\overline{w'^2}$) present in the variance of the turbulent perturbations from the lidar scan-volume average (e.g. $\sigma^2(u''_E)$). Ratios shown using the perturbation variances at each beam.

(about -0.03 $\mathrm{m^{-1}\ s^{-1}}$) has a greater magnitude than that of the stable BL (around -0.01 $\mathrm{m^{-1}\ s^{-1}}$), the curvature in the stable CBL is more sustained and paired with larger wind speeds which leads to a larger realized bias (Eq. 16). Our findings are consistent with previous studies that have identified the key interaction of the RWF with shear resulting in error bias (Lindelöw et al., 2008; Clive, 2008; Courtney et al., 2014).

The variability of the measurement errors, shown in the variance and standard deviation, are a consequence of the velocity perturbations, with negligible contribution from the RWF. In convective conditions, the weighted ~~perturbations in vertical velocity~~ vertical velocity perturbations dominate the other sources of variance in the error, indicating ~~that the vertical velocity perturbations become larger than the other terms and dominate the occurrences of large magnitude error .~~ the w'' terms are dwarfing the others and driving the error (Fig. 8d,e). The stronger the convection, the ~~more dominant the role of the vertical velocity terms~~stronger the effect, echoing the findings by Rahlves et al. (2021) that the bulk error is larger in more strongly convective conditions. By contrast, the error in the stable BL arises from a more even interplay ~~in~~ of the horizontal and vertical velocity ~~perturbations. The covariance~~ perturbation terms. The covariances between the beam perturbations ~~also generally serves~~ generally serve to temper the overall error variances, particularly near the surface where the smaller scan volume may permit stronger correlations.

~~The relative contributions of the vertical and horizontal perturbation terms is due to the variance of the perturbations themselves, which we identified as the~~

The velocity perturbation terms arise from a weighted, filtered portion of the full turbulent velocity variance, and the weighting of the terms in the error (equations 14 and 15). Physically, we might expect convective plumes to violate the desired horizontal homogeneity horizontal uniformity in the flow ??(Fig. 4), but it is an even more outsized effect that creates the error in convective conditions. The convective plumes induce large but localized vertical velocity variances so that the lidar scan volume does not filter out the bulk of vertical velocity variance while more of the horizontal turbulence is filtered out (figure variations, much of which are not filtered out by lidar scan volume, which ranges from 42-255 m across (Fig. 10). The cone angle then over-weights the vertical velocity variance terms . (Eq. 11). The compounding effects conspire to make the vertical velocity dominant in creating large errors (figures ?? and ??in convective conditions (Fig. 8d,e,f). Even in the stable boundary layer, which features much smaller vertical velocity variances, BL, the vertical velocity perturbations contribute significantly to the error. The smaller scales length-scales of the vertical velocity variations turbulence in stable conditions (figure ??) coincide with smaller turbulent variance, but also allow a larger portion of the variance to be filtered into the lidar perturbations (figure through the lidar scan volume (Fig. 10). The result is again over-weighted according to the cone angle. The contributions from the horizontal perturbationshorizontal velocity variances, meanwhile, are lessened by more of the variations being filtered out filtered out to a greater degree by the scan volume and lack of relative weightingare not weighted in the error form, lessening their relative impact compared to the vertical velocity terms.

The coupling of the error with the turbulent structure, and the vertical velocity in particular, helps explain the cause of the correlation in of the error height trends with the boundary layer structure. Variance in the horizontal perturbations is more effectively limited by the scan volume filtering, especially near the surface. In the convective cases, as velocity variance ($\overline{w'w'}$) grows from the surface to the middle of the mixed layer (figure 10(a)), so too does the variance in the w' perturbations, driving a greater spread of error with increasing height. In this example, the lidar range does not extend to the top of the convective boundary layer, but without other background sources of heterogeneity the error variance might diminish higher up, even with the large scanning radius. The error variance in the stable boundary layer peaks near the center of the boundary layer where the turbulent vertical velocity variances are large and more of the horizontal variances are filteredpass through the filter. The diminishing error variance at higher altitudes relies on the decay of both the horizontal and vertical perturbations at the top of and above the boundary layer and the and the increase in turbulent length scaleswhich combat any , which combats the increase in scan volume size.

The proportion of the full turbulent velocity variances ($\overline{u'^2}, \overline{v'^2}, \overline{w'^2}$) present in the turbulent perturbations from the lidar scan volume average (e.g. u'_E). Ratios shown using the perturbation variances at the east (solid), west (dashed), north (dash-dotted), and south (dotted) beams.

Interpreting the velocity perturbations as turbulent fluctuations filtered by the scan volume, The lidar range does not extend to the top of the boundary layer in the convective test cases, but we might expect the error variance to also peak in the middle of the connection between the lidar error variance and the structure of turbulence in the boundary layer flow becomes clear. The and decrease with height as the vertical velocity variance takes on a more prominent role in the error due to the smaller spatial scales in the turbulent variations and the additional weighting on the terms from the beam projection angle. And while the perturbations are turbulent fluctuations, the spatial tapers back toward zero. The dependence of the error height trends not only on the volume circumscribed by the scan, but also on the vertical structure of the scan volume and beam samples can induce non-zero perturbation means in the presence of cohesive structures with sizes on the order of the scan volume scale . The large vertical variances and cohesive structures in convective regimes can induce larger lidar measurement errorsboundary layer and corresponding scale and character of the turbulent structures was also noted by Wainwright et al. (2014) for sodar measurements.

3.2 Secondary effect on derived quantities: wind speed and direction

An often preferred representation of the observed horizontal wind vector is as a direction, Θ (meteorological convention), and magnitude, $|\boldsymbol{U}_h|$. The WindcubeV2 internally computes and reports these derived quantities by solving for them with the reconstructed velocity components (equation 17). The computed values do not inherit the error from the wind component errors directly; rather the quantities should be thought of as functions of the u The choice of cone angle determines the degree of projection of the horizontal and v errors treated above, taking on their own distinct, related error distribution behavior.

As non-linear functions of u and $v$vertical perturbations (manifest in the weighting in the error form) as well as the spatial separation of the sampling beams. In the strong and weak CBL test cases in particular, the error in the wind speed and direction do not drop out as cleanly as they did for the individual wind components. We can, howeverdemonstrates the adverse impacts of heavy weighting on the vertical perturbations. Rahlves et al. (2021) tested a low elevation angle (35.3° from Teschke and Lehmann (2017)) with a virtual instrument in quasi-homogeneous convective conditions with favorable results compared to more typical, larger elevation angles (60°,still estimate the breakdown of contributions so we can analyze the behavior. Consider the error of the squared wind speed,

$$|\boldsymbol{u}_{h,lidar}|^2 - |\boldsymbol{U}_h|^2 = \quad 2Uu_{err} + 2Vv_{err} + u_{err}^2 + v_{err}^2$$

To estimate the wind speed error itself, suppose that the lidar-derived estimate is close to the actual 75°). Improvements achieved by reducing the angle to lessen the weighting on the vertical velocity perturbations, however, may be offset by the corresponding effects of increasing the separation of the beams. In quasi-homogeneous turbulent conditions, a lower elevation angle lengthens the filter scale, allowing for larger error variances, up to a cap determined by the full, unfiltered turbulence. The optimal cone angle to minimize the error will depend on the balance of the competing effects in a particular flow.

3.2 Raw 1-s horizontal wind speed and direction

The horizontal wind speed and direction are computed from the lidar-measured wind components and compared against those of the volume-averaged wind speed, $|\boldsymbol{U}_h|$. Then we can factor and approximate (first order in $|\boldsymbol{U}_h|_{err}$) as follows.

$$\begin{aligned}|\boldsymbol{u}_{h,lidar}|^2 - |\boldsymbol{U}_h|^2 &= (|\boldsymbol{u}_{h,lidar}| + |\boldsymbol{U}_h|)(|\boldsymbol{u}_{h,lidar}| - |\boldsymbol{U}_h|) \\ &= (2|\boldsymbol{U}_h| + |\boldsymbol{U}_h|_{err})(|\boldsymbol{U}_h|_{err}) = 2|\boldsymbol{U}_h||\boldsymbol{U}_h|_{err} + |\boldsymbol{U}_h|_{err}^2 \approx 2|\boldsymbol{U}_h||\boldsymbol{U}_h|_{err}\end{aligned}$$

Combining with the squared speed error and solving for the $|\boldsymbol{U}_h|_{err}$, we find the error in the computed wind speed with respect to the horizontal velocity component errors (equation 34).

$$|\boldsymbol{U}_h|_{err} = |\boldsymbol{u}_{h,lidar}| - |\boldsymbol{U}_h| \approx \frac{U}{|\boldsymbol{U}_h|}u_{err} + \frac{V}{|\boldsymbol{U}_h|}v_{err} + \frac{u_{err}^2 + v_{err}^2}{2|\boldsymbol{U}_h|} = \frac{\boldsymbol{U}_h}{|\boldsymbol{U}_h|}\cdot\boldsymbol{u}_{h,err} + \frac{|\boldsymbol{u}_{h,err}|^2}{2|\boldsymbol{U}_h|}$$

The wind speed error consists of a projection of the horizontal wind errors and a strictly positive term. The more closely the mean wind aligns with an axis, the more heavily the corresponding component error is weighted. We observed slightly wider error distributions in cross-stream velocity estimates compared to streamwise (figure A2). In that case, the potentially larger error is weighted less heavily. winds (Eq. 17). The errors (Eq. 34 and 34) exhibit behavior consistent with theoretical expectations (Section 2.0.1).

The squared terms account for the positive bias observed in the wind speed error distributions (figure 11) since it consistently shifts errors to be more positive. We can explicitly find a theoretical mean of the distributions are again roughly normal. There is a slight positive skewness (long tail on the positive side of the distribution) in the wind speed error (appendix C) and simplify by assuming the u and v error random variables have a mean of zero (although this assumption can break down, e. g. in the presence of coherent structures or 0.25 in strong convection) (Fig. A2), likely due to the RWF near the surface).

$$\mu(|\boldsymbol{u}_h|_{err}) \approx \frac{\sigma^2(u_{err}) + \sigma^2(v_{err})}{2|\boldsymbol{U}_h|}$$

Note that this does not mean the total error (equation 34) is always positive – the weighted component errors can cause it to be negative – but that on average the reported wind speed will be greater than the truth. The bias should be less severe the smaller the errors in the u and v wind component estimates and the higher the wind speed. The difference in the positive, second-order bias term (Eq. 34). The bottom range-gates, influenced by the surface layer, also deviate from normal under strong convection: there is evidence of slight positive skewness (0.4) at the surface in wind direction. The excess kurtosis (+1-2) again suggests more slowly decaying tails, more pronounced near the surface. Wind direction at the surface exhibits the most extreme behavior, with an excess kurtosis of +8 at the surface.

The height and stability trends in the mean and variance of the u and v errors across the stability regimes along with the respective wind speeds accounts for the degree of bias observed between the cases, most significant for the strong CBL and least for errors (Fig. 11) follow from those of the horizontal velocity components (Fig. 7). The standard deviation of the wind speed error corresponds to that of the horizontal components as anticipated, carrying over the larger error magnitudes in the strong CBL compared to the weak CBL and followed by the stable BL.

Without explicitly computing the variance forms, we can estimate the error magnitude. The wind speed error should generally be on the order of the individual component errors (i.e. their standard deviation), though the bias term term has the potential to become more prominent in adverse conditions (large u, v errors, slow winds). The standard deviations of the wind speed error from the virtual lidar data (figure 11) do match up with The trends in standard deviation, growing with height over the lidar range in the convective cases and peaking mid-boundary layer in the stable BL, are also consistent with those of the u and v error distributions, maintaining respective height trends in each of the stability cases as described in the previous

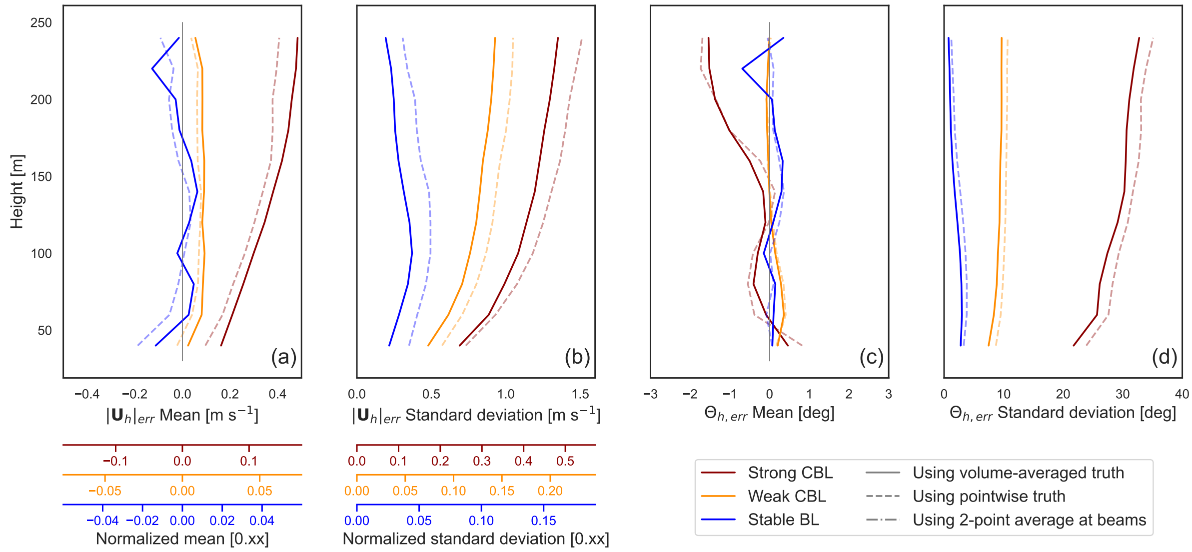

Figure 11. Mean and standard deviation of error in the 1-Hz, vector-averaged wind speed and wind direction. For wind speed, the primary axis gives absolute error and colored secondary axes designate relative error with respect to 100-m values for the respective LES case.

section. component errors. The bias in the u and v components also propagates into the bias in the wind speed error, reflecting the underestimate due to shear near the surface of the stable BL and weak CBL.

Now consider the wind direction error. To simplify the analysis, we set aside the quadrant correction and consider just the traditional inverse tangent function to find the angle in $[-90°, 90°]$. Then the wind direction error, in radians, is the difference,

$$\Theta_{err} = \Theta_{lidar} - \Theta = \arctan\left(\frac{u_{lidar}}{v_{lidar}}\right) - \arctan\left(\frac{U}{V}\right)$$

As with the wind speed , the mean value does not directly cancel. Applying the difference identity for arctan and simplifying,

$$\Theta_{err} = \arctan\left(\frac{V u_{err} - U v_{err}}{|\boldsymbol{U}_h|^2 + V v_{err} + U u_{err}}\right)$$

Turn this into looser bound that is simpler to interpret. The derivative of arctan is continuous and bound above by one so that we may bound, $|\arctan(x)| \leq |x|$. For the error,

$$|\Theta_{err}| \leq \left|\frac{V u_{err} - U v_{err}}{|\boldsymbol{U}_h|^2 + V v_{err} + U u_{err}}\right| = \left|\frac{|\boldsymbol{u}_{h,err}|\sin(\theta_{\boldsymbol{U}_h,\boldsymbol{u}_{h,err}})}{|\boldsymbol{U}_h| + \frac{\boldsymbol{U}_h}{|\boldsymbol{U}_h|}\cdot \boldsymbol{u}_{h,err}}\right|$$

The bound is tighter the smaller the error and the sign of the bounding expression should match that of the error creating an 'envelope' for the error. As opposed to We derived a systematic positive bias term in the wind speed , in the wind direction error form, the mean velocity components are cross-multiplied with measurement (Eq. 34) which is leading order when the biases in u and v are negligible. In the ensemble mean, it is proportional to the variance of the horizontal component errors and inversely proportional to the velocity component errors. Depending on the orientation of the wind, one of the terms in the numerator is more likely to dominate: the stronger wind component multiplied with the larger cross-stream error.

Under the error approximation, we can similarly estimate the mean error (equation 34). If we again assume the wind speed (Eq. 19). It follows that measurements in the strong CBL experience the most significant biases (0.2-0.4 $\mathrm{m\,s^{-1}}$), growing with height as do the u and v reconstruction errors to have zero mean , then the wind direction mean error should also be zero.

$$\mu(\Theta_{h,err}) \approx \frac{1}{|\boldsymbol{U}_h|}\left(\sin(\Theta)\mu(v_{err}) - \cos(\Theta)\mu(u_{err})\right)$$

As seen in the strong CBL (figure 11), the approximation can break down in significant ways, introducing bias and listing. Patterns in coherent structures were identified as a likely cause of non-zero means in error variances. The same occurs, to a lesser degree, in the weak CBL with a bias < 0.2 $\mathrm{m\,s^{-1}}$. In the stable BL, which has small u and v, but the v error variances and fast mean winds, the bias term becomes negligible.

We anticipated that the wind direction bias should be close to zero assuming the u_{err} and v_{err} were similarly distributed with zero mean. The computed bias is indeed generally small ($< 0.5°$ in the weak CBL and stable BL and $< 2°$ in the strong CBL). Under strong convection, the wind direction observations list more and more counter-clockwise (southward) from truth with height. The expansion of the expected bias in the wind direction (Appendix C), relies on the uniform distribution of the direction and magnitude of the biases in the strong CBL resemble those in the stable BL at some heightshorizontal error vector $(u_{err}, v_{err})^T$, which coincides with zero mean bias in the horizontal wind components. Deviations from this assumption result in small terms scaled by powers of $1/|\boldsymbol{U}_h|$ (Eq. B9) so that fast wind speeds act instrumentally to diminish bias in the wind direction. The combination in the strong convection case of the coherent structures and the weak winds allows the even small non-zero means in u and v to be amplified to create the wind direction error bias. The stable BL, on the other hand, tempers the effect by the wind direction bias through the strength of the wind speeds. If the lidar ensemble included instruments rotated at offsets Over an ensemble including instruments spanning a full 360° rather than 45°, the signs of the errors would cancel (flipping the signs of u and v in the lidar coordinate system flips the signs of the error)set of offsets we would expect the signs to cancel leaving zero bias. Within the ensemble of offsets computed with the virtual instrumentover a 45° arc used here, however, the signs are consistent and the bias persists across the rotated lidar measurements. For measurements made in relatively steady, slow winds it cannot be expected that bias will not emerge as it does Measurements made in conditions of slow winds of fairly consistent direction, as in the strong CBL datacase, do not benefit from the cancellation expected in an ensemble over all instrument orientations and should take into account the possibility of a persistent bias arising in the wind direction.

3.2.1 Effects of wind speed and orientation angle

The idea that lidar might manifest a smaller error at higher winds seems intuitive. On top of In addition to potential implicit effects on the homogeneity over the correlations across the scan volume, the derived error forms (Eq. 34 and 34) draw out explicit dependencies on wind speed and direction. The trends predicted by the analytic form convincingly describe those

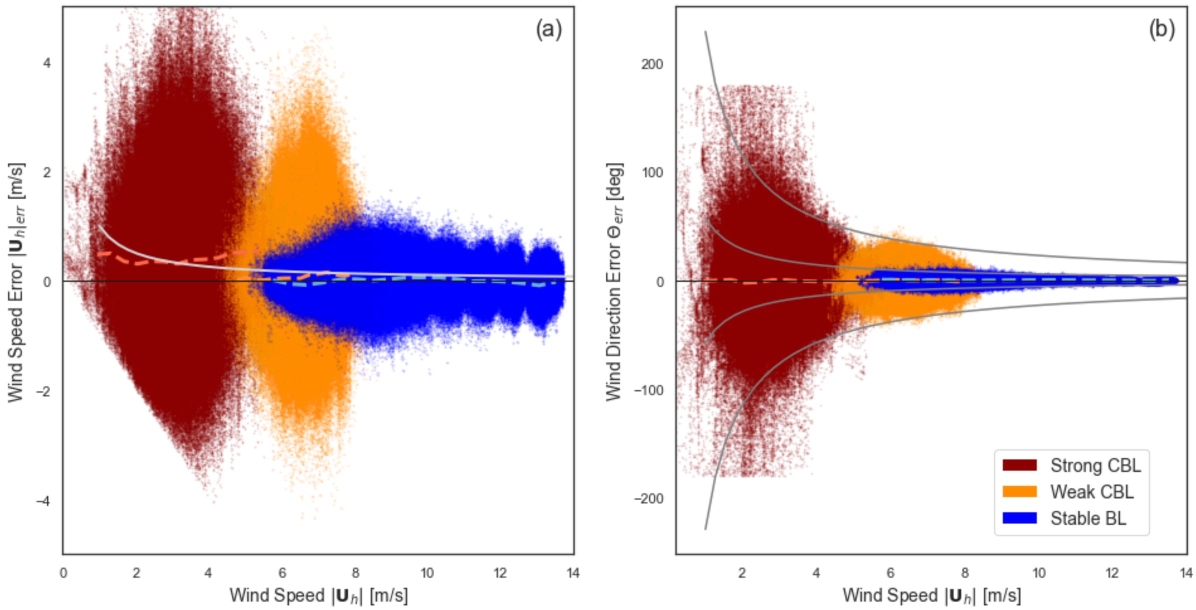

Figure 12. Trends in (a) wind speed and (b) wind direction errors with respect to the volume-averaged wind speed~~for the observation~~. Data points from all lidar measurements are colored by stability case: strong CBL (red), weak CBL (orange), and stable BL (blue). Reference lines are given ~~in (a)~~ for the mean ~~scatter~~ error for each stability at each wind speed (colored, dashed)~~and $1/|\boldsymbol{U}_H|$ decay~~. Reference lines (grey, solid) ~~. In~~ trace (a) $1/|\boldsymbol{U}_h|$ decay and (b) ~~, reference lines trace~~ the ~~$1/|\boldsymbol{U}_H|$~~ $1/|\boldsymbol{U}_h|$ and ~~$4/|\boldsymbol{U}_H|$~~ $4/|\boldsymbol{U}_h|$ envelopes.

~~observed in the virtual lidar data.~~ We find that wind speed powerfully influences error in the lidar observations, ~~while~~ whereas the orientation of the lidar with respect to the mean wind has a negligible impact.

The wind speed trends ~~in~~ across all the virtual lidar ~~data align with theoretical assessments (figure 12)~~wind speed and direction data are shown in Fig. 12. The wind speed error magnitudes visibly contract from the slow, strong CBL data to the fast winds of the stable BL; the decrease has to do with the identified mechanisms of filtered turbulence driving the error variance in each of the stability regimes. A trend line for the mean error in the wind speed measurement is computed for each stability case with respect to the true ~~volume averaged wind speed . It exhibits a positive bias that diminishes rapidly with increasing wind speed . Variations in~~ volume-averaged wind speed over 0.5 $\mathrm{m\,s^{-1}}$ bins with at least 2500 points. The positive bias in each stability case is clearly evident. All else being equal, we expect from the form of the wind speed bias (Eq. 19) that faster wind speeds should temper the magnitude of the ~~u and v error variances in the numerator as well as contributions from their deviation from zero means introduce noise on the predicted $1/(2|\boldsymbol{U}_h|)$ (equation 34) decay~~bias according to $1/(|\boldsymbol{U}_h|)$. Comparing the tending bias with the expected decay, we cannot confirm the behavior empirically over the natural variations in the error variances concomitant with wind speed in the virtual lidar test case data.

According to the wind direction error form (Eq. 34), we expect the magnitude of the error to decay on the whole with at least $1/|\boldsymbol{U}_h|$. Indeed, allowing for potentially different scales of u and v error in the numerator, the data ~~falls~~ fall nicely along the

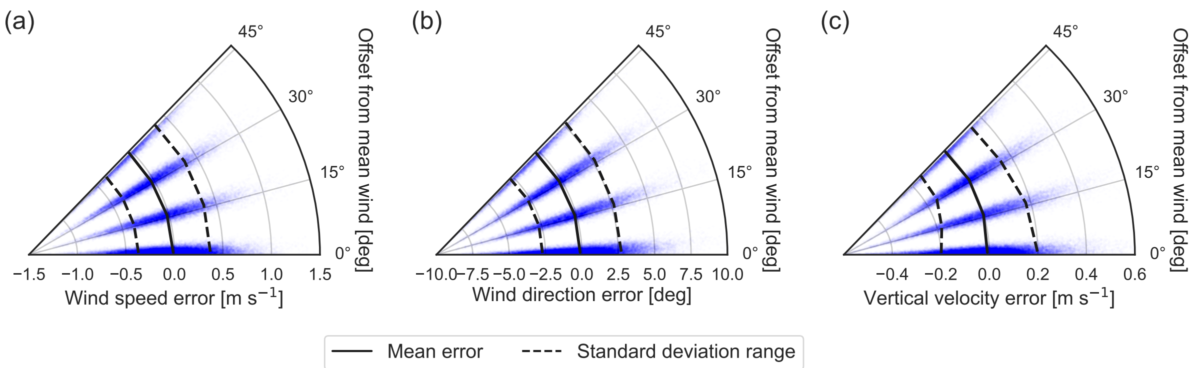

Figure 13. Errors in the 100-m (a) wind speed, (b) wind direction, and (c) vertical velocity (wind-direction weighting, Eq. 9) in the stable BL case plotted against the offset angle between the wind direction and the nearest lidar axis. ~~Data clusters around~~ Lines show the ~~offsets for the discrete offset angles tested~~means (solid) and standard deviation interval (dashed).

reference envelopes, especially along the tail of the stable BL. ~~The additional decay is likely accountable to the inverse tangent which curtails the~~ In some cases, the decay in the error magnitudes is greater than the anticipated $1/|\boldsymbol{U}_h|$ bound. This may be in part because the inverse tangent in the full error expression (Eq. 21) should act to further curtail the size of the largest errors ~~compared to~~ more than is captured in the bounding estimate ~~as well as improved correlation at the heights with the strongest winds reducing the component errors~~(Eq. 22) and in part because of implicit correlation effects and variance behavior with height and wind speed.

Potential differences in error as a function of the lidar orientation ~~with respect to the mean wind direction come from slight differences in the weighting in~~ are due to projection of the error vector onto the mean wind parallel or transverse directions (Eq. 34 and 34) and implicit differences in correlation effects in the streamwise and cross-stream directions. In the virtual lidar error data, only small discrepancies could be distinguished between errors in the ~~stream-wise~~ streamwise and cross-stream velocity component estimates~~, likely due to the relatively poorer correlation in the cross-stream velocity component. Comparing the~~ ; comparing the disaggregated rotated lidar ensembles (~~figure A2~~Fig. 7), a slight amplification in error variance shifts from one component to the other~~depending on which has a smaller projection of the prevalent wind~~.

~~In practice,~~ As in Rahlves et al. (2021), our results suggest changes in orientation produce a negligible effect on the error ~~which~~ that is washed out by other, more significant ~~sources. (figure **??**). A small improvement in the error spread for $|\boldsymbol{u}_H|$, Θ and w might be discerned when the lidar axes are closer to an even 45° offset from the prevailing wind (~~effects (illustrated by the 100-m measurements in the stable case~~; this variability erodes completely in the convective cases)which makes the relative error between the horizontal wind components more consistent. The~~ , Fig. 13). The noticeable trend with offset angle in the vertical velocity error ~~may be because of a combination of the correlation and the full, even incorporation of all four beams in the reconstruction (equation 9), each with similar error distribution characteristics. None of~~ appears only when using the wind-direction weighting (Eq. 9), not under equal weighting of the ~~trends are particularly significant, however~~beams (Eq. 8).

As discussed in Section 3.4, the dependence is likely due the difference in the effective number of beams used, with an average over two beams having more variability than over four. The lack of sensitivity in the wind speed and direction error distributions suggests that the direction of the error vector, $(u_{err}, v_{err})^T$, is fairly evenly distributed. Comparing moments across the rotated ensembles (figure Fig. A2) confirms that there is little meaningful difference in the error behavior between offset angles (with some exception for peak variance of the stable BL vertical velocity error).

It should be noted that although no strong trends were found with respect to the relative offset between the mean wind and the lidar axes, the signs of some of the biases can change with the signs of u and v. The derived error forms for the wind speed and direction and discussion of the RWF (section C) explain these dependencies.

3.3 Reducing error through time averaging

3.3 Time-averaged horizontal velocities

Common time-averaging intervals used with lidar data may be over 2, 10, or even 30 minutes, with experimental evaluations of the system accuracy often reported in terms of the 10-minute average in wind energy contexts. As with the error in the high(er) frequency wind measurements, we characterize the error distribution of the ten-minute averaged measurements (Fig. 14).

We first characterize the error distributions of the vector-averaged lidar measurement compared to the vector-averaged point- and volume-references for the wind speed and direction (Fig. 14). Each distribution in the 10-minute average comprises an ensemble of a total of 180 values (ensemble and offset angles).

Time averaging reduces the 'noise' of the error in the raw, highfrequency measurements made by the lidar, leaving a more reliable mean measurement. Under conditions in which the background flow continues to evolve in time, the utility of time averaging must be weighed against the length of the interval during which 'quasi-stationary' conditions exist and sacrificing the resolution of shorter time-scale dynamics. Making an informed assessment of an appropriate time window length rests on quantifying the expectation of the improvement of the measurement.

The lidar error varies along with the 'random' turbulence in the flow which we have reflected by describing the error as a random variable drawn from a distribution dependent on the character of the turbulence and the lidar scan geometry. In preceding analysis we considered how the physical and mathematical mechanisms might influence the distribution of the error in the raw lidar measurement. Now we consider how time averaging acts on the full error distributionUnder stationary and homogeneous flow conditions, the notions of pointwise and volume-averaged truth start to converge to a general spatio-temporal average, which is reflected in the merging of the two error distribution profiles. The correspondence suggests that field studies comparing against time-averaged "point" tower measurements can effectively reflect the error with respect to the volume-average as well (ignoring spatial displacement of the tower from the lidar). The overall error magnitudes found by the virtual lidar are consistent with those in field deployments of lidar compared against tower measurements. In select, flat conditions typical mean discrepancies in the range ± 0.2 $\mathrm{m\,s^{-1}}$ with standard deviations of 0.20 $\mathrm{m\,s^{-1}}$ (Courtney et al., 2008) have been reported, which encompass all but the more extreme errors in the strong convection case. The virtual 10-minute averaged wind speeds have mean errors within ± 0.2 $\mathrm{m\ s^{-1}}$ with standard deviation < 0.3 $\mathrm{m\ s^{-1}}$. Furthermore, the wind

Change in time-average error distribution compared to the error distribution of the 1 Hz samples for wind speed and direction. Left panels show shift in the distribution means $\mu(u_{err}) - \mu(\overline{u}^{T}_{err})$ and right panels show the ratio of the standard deviation of the time-averaged error distribution to the original $\sigma(\overline{u}^{T}_{err})/\sigma(u_{err})$. Colors indicate stability case: red (strong CBL), orange (weak CBL), and blue (stable BL). Expected ranges are demarcated by the shaded box.

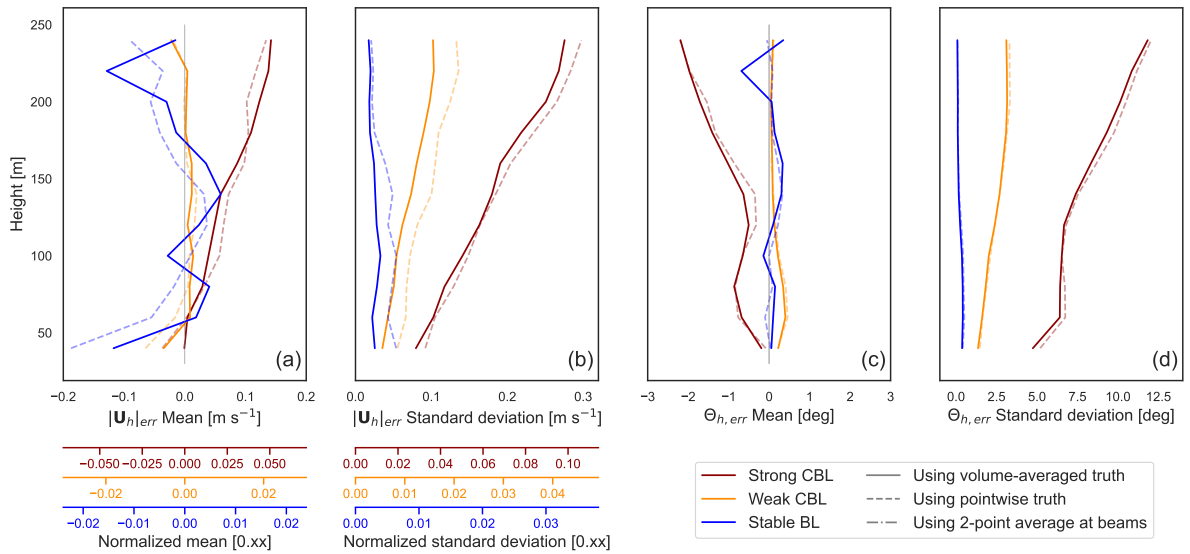

Figure 14. Mean and standard deviation of error in (vector) 10-min averaged wind speed and wind direction. For wind speed, the primary axis gives absolute error and colored secondary axes designate relative error with respect to 100-m values for the respective LES case.

direction has mean error bias within 2° and standard deviations within 2.5°, except for in the strongly convective case where it can reach up to 12°.

Time averages were performed over the wind components (which is mathematically equivalent to averaging over the beam radial velocities when the reconstruction is linear with respect to them as in equation 8). Let T be the length of time window average and suppose the instrument samples at a constant interval of τ_s (every second for the WindcubeV2). Then there are $T_s = \lfloor T/\tau_s \rfloor$ samples in the discrete average over the window. Assume quasi-stationary conditions so that the volume average at one any given time is close to

As anticipated, the time-averaged errors reflect a decrease in the wind-speed bias in the convective cases, little change in the time averaged valuewind-direction bias, and a reduction of the standard deviations (by a factor of around 5). The degree of reduction in the biases and standard deviation are not uniform, but vary somewhat with stability and height, likely depending on the decorrelation scales in the error time series. This leads to some shift in the shape of the moment profiles compared to the original distribution, e.g. $U \approx \overline{U}^{T}$. the curvature of the standard deviation with height.

Start with the effect of the average Based on the error in model, not only a reduction in error magnitude and bias (in the wind speed) were predicted, but also the rate of reduction. The wind speed error distribution at 100 m was computed for several

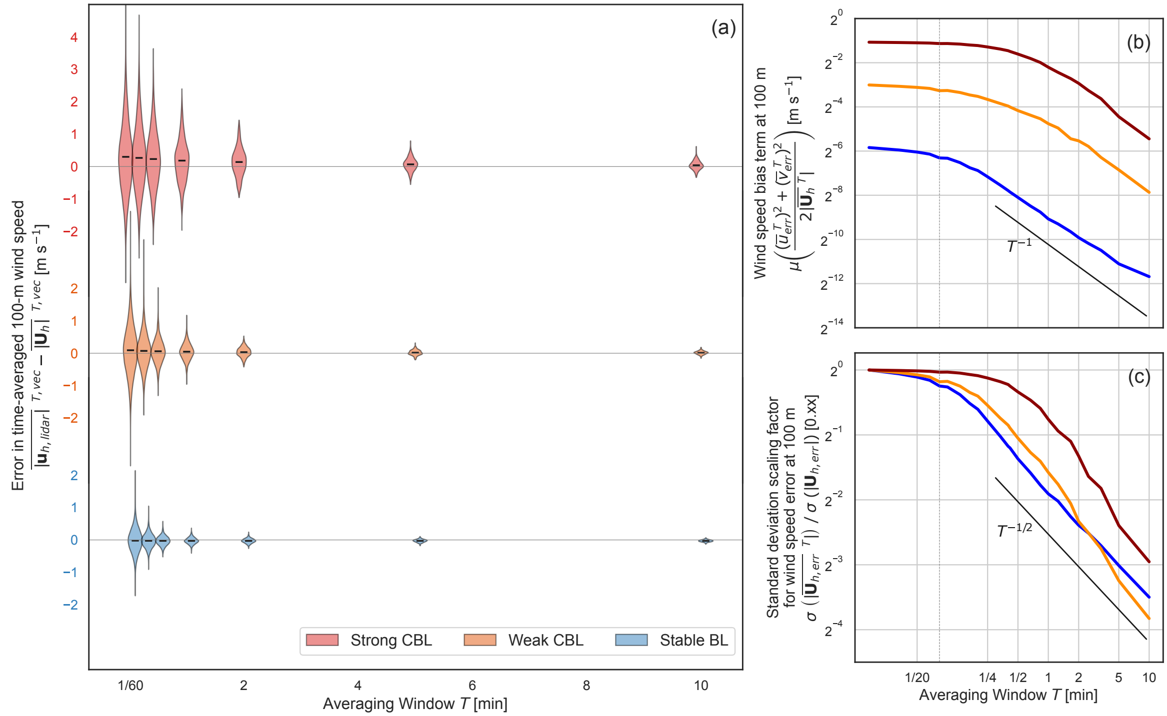

Figure 15. Wind speed error at 100 m under a vector time average. (a) A violin plot of the error distribution and mean for each stability over several averaging windows up to 10 min. (b) The reduction in the second order positive bias term against a reference T^{-1} rate. (c) The reduction in the error standard deviation against a reference $T^{-1/2}$ rate.

time-averaging windows ranging from a few seconds to the full 10-minute span available. Not only is the reduced spread of the distribution marked across cases and the decay of the bias apparent in the strong CBL (Fig. 15a), but both decay according to the anticipated power laws ($\propto T^{-1}$ decay of the wind component reconstructions. The following derivations are given in terms of u, but hold identically for all the wind components. Expanding the lidar estimate of the time-averaged truth, $\overline{U}^T$, the error in the time averaged measurement emerges as the arithmetic mean of each of the sample errors (equation 23)

$$\overline{u}_{lidar}^T = \frac{1}{T_s}\sum_{t=1}^{T_s} u_{lidar}(t) = \frac{1}{T_s}\sum_{t=1}^{T_s}[U(t) + u_{err}(t)] = \overline{U}^T + \frac{1}{T_s}\sum_{t=1}^{T_s} u_{err}(t) \quad \Longrightarrow \quad \overline{u}_{err}^T = \frac{1}{T_s}\sum_{t=1}^{T_s} u_{err}(t)$$

That is , the error in the time-averaged measurement can be expressed as the sum of (scaled) random variables drawn from the distribution of the original sample errors. Using linearity, the mean of the time-averaged error distribution, $\overline{u}_{err}^T$, is equal to the mean for the original sample errors; i.e. time averaging does not change the mean ensemble error of the wind components. The result holds for any linear reconstruction. The mean error in individual measurements may benefit from time averaging, however, as the time average approaches the potentially less biased 'ensemble' error from the selective sub-sample (e. g. figure

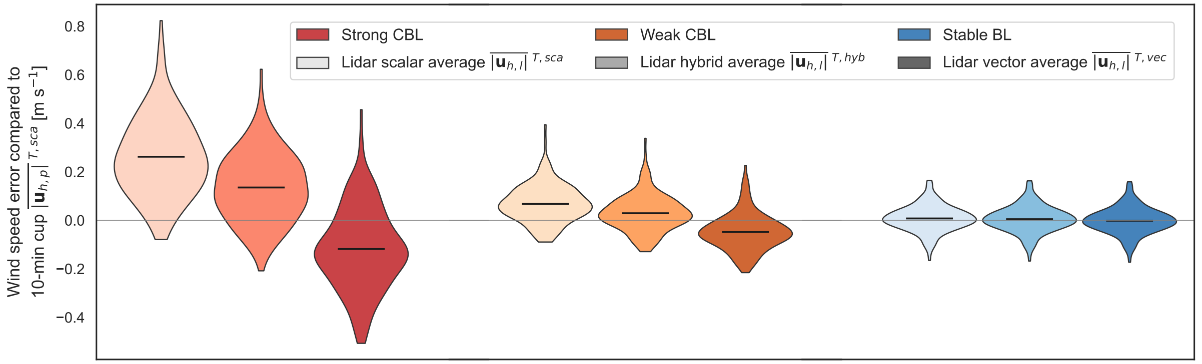

Figure 16. Comparison of time-averaged lidar wind speed estimates at 100-m (using vector-, scalar-, and hybrid-average) with the pointwise, scalar average representing a cup measurement. Black horizontal lines show the distribution means.

??). bias term and $\propto T^{-1/2}$ reduction in the standard deviation (Fig. 15b,c). The behavior is representative of other heights and of the decay rate in the standard deviation of the wind components and wind direction averages.

The time average does, however, reduce the error spread, as observed in the virtual

We also compared 10-minute vector-, scalar-, and hybrid-averaged lidar data. The variance of a sum of independent, identically distributed variables is well known; the variance of the original random variable (the un-averaged error) is scaled by one over the number of samples in the average. In a time series, the samples cannot simply be treated as independent since subsequent samples are highly correlated. In the lidar , the pattern of turbulent structures that gave rise to a particular error continue to influence the error in the following samples as well so that the errors are quite similar. The reduction factor on the error standard deviation may be estimated by a range. The lower bound is given by treating all of the T_s samples in the time average as independent, even though they are not. A rough upper estimate can be formed by simply discarding the highly-correlated data. Let τ_c be the decorrelation time for the time series (which should be similar to the decorrelation time for the winds themselves) . A time average computed only with T_c samples spaced at least τ_c apart from one another can safely treat the samples as independent. The combination of the estimates provides a range of factors by which we can expect to reduce the error standard deviation in the time-averaged estimate of the wind components (equation 34)

$$(T/\tau_s)^{-1/2} \approx T_s^{-1/2} \leq \frac{\sigma_{\overline{u}^T_{err}}}{\sigma_{u_{err}}} \lesssim T_c^{-1/2} \approx (T/\tau_c)^{-1/2}$$

The standard deviation reduction factor (assuming τ_s, τ_c fixed) scales proportionally to $T^{-1/2}$. The marginal utility of longer time average in terms of reducing the standard deviation shrinks rapidly; just four independent samples are needed to halve the standard deviation but 100 are needed to bring the standard deviation to a tenth of its original value. wind-speeds (Eq. 26, 27, and 33) against a scalar-averaged point measurement made at the center of the scan volume for the 100-m winds (Fig. 16). At this height, which is mid-boundary layer in all stability cases, the lidar scalar-average over-estimates the speed reported by the "cup" measurement whereas the vector average under-estimates. The straddling of the cup measurement was anticipated for unstable stratification or cases of strong mechanical turbulence. The hybrid scheme, taking the weighted average, works as designed to scale the inflation of the lidar scalar-averaged winds compared to the vector average to better represent the inflation experienced by a point measurement, thereby improving the error bias. The reduced bias is most pronounced in the convective cases, which experienced larger biases compared to the cup measurement in both the vector- and scalar-averages and a larger gap between the two averaging types. The bias in both average types is small in the stable BL so that the realized change is negligible. We now consider what the ideal weights for a hybrid scheme would be, across the simulated cases and heights, and how they relate to the flow behavior.

The error in the derived quantities of wind speed and direction were derived in terms of the wind component errors. For the time-averaged quantities, we may simply use the modified component distributions, which we determined above had (1) no change in mean and (2)scaled variance.

The wind speed error experiences an improvement not only in the spread of the error but also in the mitigation of the positive bias . In the mean, the first terms in the wind speed error (34) remain unaltered, but the positive bias term is proportional to the sum of the The theory behind the hybrid average leverages the expected inflation in a scalar-averaged wind speed (compared to the vector average) in a lidar and a pointwise measurement (Eq. 32 and 31). A pointwise inflation arises purely from fluctuations in the horizontal velocities (u', v') while the lidar measurements of u and v error variances and is accordingly scaled by the factor $(T/\tau_c)^{-1}$. Though the mean estimates of the wind components themselves do not improve under the time average, contain projected vertical velocity fluctuations, which are also reflected in the inflation factor. We decompose the contributions to the lidar inflation-factor based on the virtual lidar ensembles and compare to the corresponding pointwise inflation (Fig. 17). Following the form of the analysis in Rosenbusch et al. (2021), the reduction in the spread of their errors leads to a marked improvement in the mean error of the wind speed. The variance for the wind speed was not explicitly computed but estimated to be roughly equal to a weighted combination of the two-point beam average is used as the U and V truth reference in the lidar computation and the RWF is omitted (instead directly interpolating the radial velocity) to focus on the turbulence effects.

The lidar wind speed inflation is decomposed into horizontal velocity fluctuation terms and terms due to vertical or mixed vertical-horizontal velocity fluctuations. Note that the lidar inflation-factor is due to perceived variances in the horizontal velocity components and its decomposition echos the decomposition of the u and v error variances. The reduction factor for the wind speed variance (and thus standard deviation)is about that of the wind components. Using the rough approximation for the decorrelation time, error variances (Fig. 8). The findings are consistent with the analysis of limiting-case behavior in Rosenbusch et al. (2021). The combined contribution to the lidar inflation factor by the horizontal velocity fluctuations is consistently less than that experienced by a point measurement (across stability and height). Based solely on these terms, the lidar-scalar average would under-estimate the averaged cup-wind-speed. The additional variation due to the projections for the change in the time averaged behaviors hold up against the virtual lidar data (figure ??). vertical velocity, which has no counterpart in the point measurement, means that in the convective cases the lidar scalar-average experiences a greater inflation than a cup measurement would. The stable BL behaves in a similar fashion within the bulk of the boundary layer (< 150 m) where there is moderate vertical velocity variance. Higher, however, the vertical velocity contributions become less substantial and only just compensate for the difference between the lidar and pointwise horizontal velocity terms. In this upper

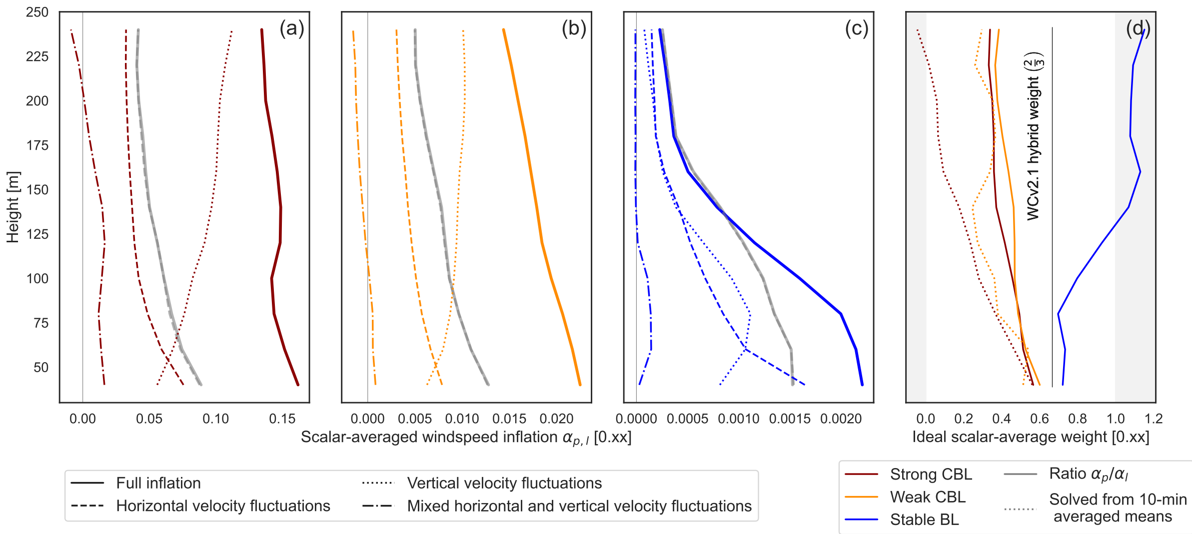

Figure 17. Decomposition of the lidar and pointwise scalar-average inflation factor (α_l and α_p) in the (a) strong CBL (b) weak CBL, and (c) stable BL. Contributions to the inflation from horizontal (u', v'), vertical (w'), and cross-terms ($u'w'$, $v'w'$) with the lidar shown in color and the pointwise inflation in grey. (d) Shows the ideal weighting for the scalar-averaged lidar measurement in a hybrid scheme computed from the ratio of pointwise inflation factors and solved directly from the 10-minute averaged mean errors.

regime, the cup measurement would be expected to match or exceed the lidar scalar-average. The ideal weighting of the lidar scalar-average for the hybrid scheme (assuming the vector-average biases are zero) is given by the ratio of the pointwise to lidar inflation factors, α_p/α_l. The ratio determined from the LES test cases (Fig. 17d) suggest a value smaller than $\frac{2}{3}$ is needed to fully counter the vertical velocity contribution in the convective conditions (around 0.3-0.6). A larger weight would be required in stable conditions: 0.7 up to one in the bottom portion of the boundary layer and exceeding a weight of one where the lidar scalar-average underestimates the point scalar-average. Overall, without optimizing the weighting for a particular type of flow, the $\frac{2}{3}$ weight splits the difference between the LES test cases.

~~The mean wind direction error should experience negligible change under the time average since it arises from the component error means. The estimate of the error magnitudes project it to be proportional to the component standard deviation over the mean horizontal wind speed. Since we assume the wind speed to be consistent through~~ The derivation of the hybrid scheme and the weightings shown above are predicated on the assumption that the bias term vanishes completely in the 10-minute, vector-averaged pointwise and lidar measurements. The vector averages were assumed to be equal approximations of the speed of a Reynolds-averaged wind. The behavior of the bias in the vector-averaged winds suggests that, at least for the upper range-gates in the strong CBL, a non-negligible positive bias (0.1-0.2 $\mathrm{m\,s^{-1}}$) persists under a 10-minute average (Fig. 14a). The persisting bias results from the combination of a large initial bias (Fig. 11a) and correlation in the time-series slowing the decay of the bias term under the vector average (Fig. 12). In the derivation, the difference between the vector and scalar time-average is assumed to reflect the entire inflation factor; however, in conditions such as upper strong CBL range, only a portion of the

inflation factor divides the two after 10-minutes. The 10-minute lidar scalar-average will consequently be over-weighted when using the α_p/α_l ratio. Again omitting the RWF from the model, we solved for the weights required to fully cancel the bias in the lidar-cup comparison using the the ensemble errors of the 10-minute averaged winds (Fig. 17d). (We have omitted the weights for the stable BL; the small biases, $< 0.02\,\mathrm{m\,s^{-1}}$, produce noisy, unreliable results and the vector-average bias in this case has decayed to negligible levels). In practice, the 10-minute averages in the strong CBL requires smaller weights (0-0.4) on the lidar scalar-averaged wind speed than expected based on the full inflation factors (0.3-0.6). In order for the underlying theory in the weighting to be applied in this case, the the remaining inflation in the vector-averaged wind speed would have to be addressed directly or further diminished extending the time window, the wind direction standard deviation should also be reduced by the same factor as the wind components, $(T/\tau_c)^{-1/2}$. Both predictions hold up in the empirical results (figure ??).
.

3.4 Note on vertical Vertical velocity measurements

Comparison of the error in vertical velocity measurement using the evenly weighted vertical velocity reconstruction (equation 8), dotted line) and the wind-direction weighted reconstruction (equation 9), solid line). Both use the volume-average as truth.

The vertical velocity measurement demands separate treatment from the horizontal winds. The vertical velocity itself behaves distinctly from the horizontal winds : it varies much because it varies more rapidly and the the features of interest occur at smaller spatial and temporal scales, the background signal being with the background (spatio-temporal average) signal tending close to zero. The WindcubeV2 offers two possibilities to reconstruct the vertical velocity from the measured radial velocities by either equally weighting the beams or using the wind direction to selectively weight them (equations 8 ,Eq. 8 and 9). The measurement from the vertical beam is a third option that samples just the vertical velocity and does not require reconstruction.

Since the Because the variation in the vertical velocity generally occurs at a smaller scale than the scan volume, the most interesting information much of the dynamics will tend to be lost in the reconstruction process. Even if the volume average were perfectly recovered, the average itself loses information. The measurement from the vertical beam is a third option that samples just the vertical velocity and does not require reconstruction.

The error induced in the different sensing cases were separately examined from the virtual instrument data. Figure 18 compares the two reconstruction techniques (equations 8 and 9

Figure 18 shows the mean and variance of the error using the two reconstruction techniques. The vertical velocity error distributions using point and volume-averaged truth references do not mirror one another as they do for the u and v velocities. Because the variability in vertical velocity occurs on a shorter length-scale, the pointwise value is less representative of the volume average, which explains the greater discrepancy. In all cases, the bias is negligible ($< 0.02\,\mathrm{m\,s^{-1}}$). The equally-weighted reconstruction was examined in depth with the analytic break down standard deviation of the error ; here we empirically consider the effect of instead using the wind direction weightingis driven by similar dynamics as in the horizontal components; the vertical velocity variance dominates and the height trends follow the boundary layer structure (Fig. 8). In the vertical

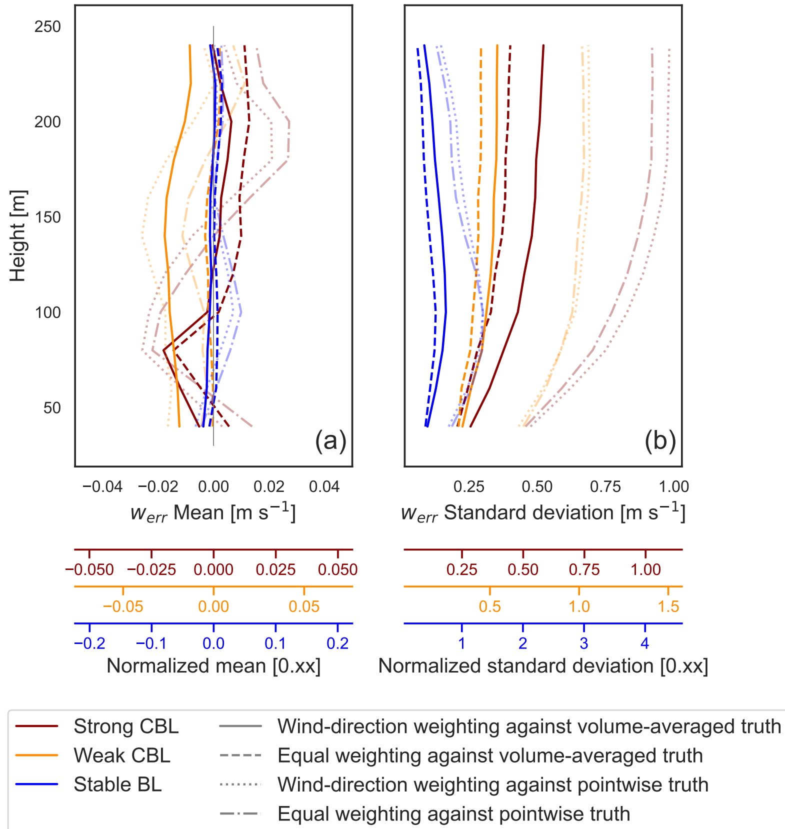

Figure 18. Comparison of the error in vertical velocity measurement using the evenly weighted vertical velocity reconstruction (Eq. 8, dotted line) and the wind-direction weighted reconstruction (Eq. 9, solid line). Both use the volume average as truth.

velocity, however, the relative magnitude of the standard deviation can grow to large fractions (0.3-0.9) of typical magnitudes in all stability cases, obscuring the actual signal in the measurement.

~~At~~ Comparing the reconstruction techniques, at least with respect to the disk-averaged truth, the lessened dependence on the full four beams using wind direction weighting seems to outweigh the beneficial effects. When the wind is directed between the lidar axes (45~~degree angle~~° offset), the two reconstructions are identical; the difference arises when the wind direction lies more closely with one of the axes so that two beams are weighted more heavily, shrinking the contribution from the other two beams. In our test cases, the reconstruction relies primarily on the east and west beams. With respect to the volume-averaged vertical velocity, the ~~bias and~~ standard deviation of the error is on the whole larger under the reconstruction using wind direction weights than with equally weighted beams (~~figure 18).~~ Fig. 18b). The behavior is consistent with the sensitivity of the wind-direction weighting to the orientation angle of the instrument (Fig. 13), which showed slightly smaller standard deviations when the mean wind was closer to a 45° offset with the lidar axes.

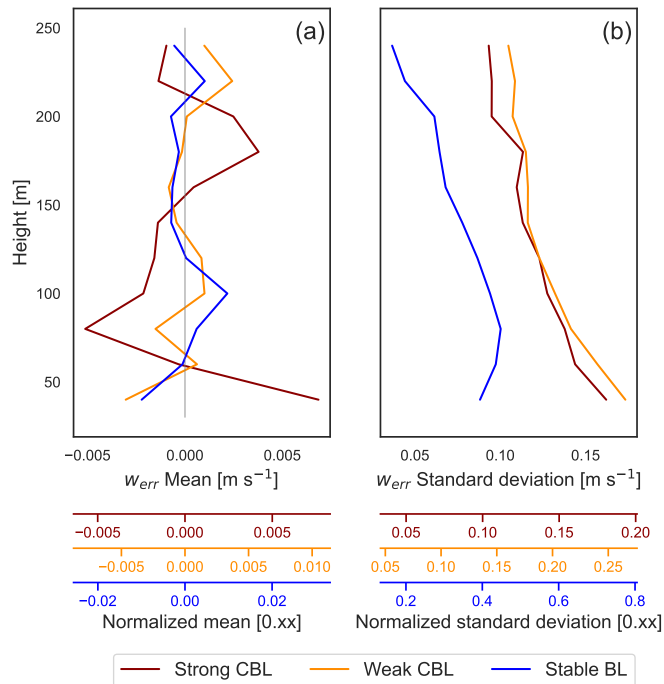

Figure 19. Vertical velocity measurement error moments for the vertically pointed beam. Error is with respect to the pointwise truth.

In the context of the random variable error model (~~equation ??~~Eq. 11), weakening or removing dependence on some of the beams removes the chance for ~~cancellation of~~ canceling the perturbations; the mean over two points will tend to be a poorer representation of the volume ~~mean than that~~ average than the mean over four points. The concentrated dependence can also magnify the influence of variations experienced at the two beam locations. In light of the empirical error behavior, the benefits of incorporating more points ~~seems~~ seem to supersede the benefits of streamwise correlations.

The vertical beam sidesteps the implicit volume average ~~as well as~~ along with the need for any reconstruction. In this case, the error incurred in measuring a pointwise vertical velocity arises purely from the effects of the ~~range-gate-weighting~~ range-gate weighting in the measurement process. The RWF produces errors with magnitude and character that are distinct from the reconstruction errors (~~figure~~ Fig. 19). Across stability cases, the bias ~~shrinks to be negligible~~ is negligible (<0.005 $\mathrm{m\,s^{-1}}$). The difference in standard deviation between the convective cases vanishes and the overall magnitude is significantly reduced compared to ~~the error~~ that in the reconstruction methods. As opposed to the error in the reconstruction estimate, the standard deviation with only the RWF decreases with height. In the stable case, the RWF was a larger relative portion of the error in the vertical velocity reconstruction (~~figure ??~~Fig. 8). Under stable conditions, the difference between the reconstruction and the vertical beam is less dramatic; the standard deviation magnitudes are about halved and the decrease in the standard deviation with height exists with both but is more pronounced with the vertical beam. Even when using the vertical beam, the standard deviation can still be relatively quite large compared to typical values.

4 Discussion

~~Atmospheric variability inextricably influences error in wind lidar measurements. By using virtual instruments acting on LES flows, error mechanisms can be isolated and explicitly tracked and analyzed to better understand the error behavior as a whole. In this study, we considered profiling lidar measurements in quasi-stationary conditions. Even in the absence of explicit sources of inhomogeneity, observation error can arise, tightly coupled to the character of turbulence in the flow. The error distributions of a virtual WindcubeV2 lidar were estimated from ensembles of virtual lidar run in uniform, ideal WRF-LES scenarios in convective and stable boundary layer regimes. An analytic error model leverages random variable representations to describe how the turbulent variability propagates into the lidar error, decomposing the contributions from velocity perturbations at each beam from the volume-average and from deviations in the point measurement due to range-gate weighting.~~

The quantification of the error found here aligns with values found in field studies ~~(e.g. Courtney et al. (2008))~~ (Courtney et al., 2008) and in similar estimates of virtual lidar performance in baseline convective conditions (Rahlves et al., 2021). To define the error, we compared virtual measurements against both a pointwise truth reference and the average over the scan volume. ~~Under ten-minute averages in the quasi-stationary conditions of the test cases~~With 10-minute averaging, the distinction between the kinds of spatio-temporal averages fades and the two error distributions seem to converge. The magnitudes of the overall errors in the virtual measurements fall generally within experimentally determined ranges in favorable conditions: ~~ten-minute averaged~~ 10-minute-averaged wind speeds have mean errors within ~~$\pm 0.2 m/s$ with standard deviation $< 0.3 m/s$~~ ± 0.2 $\mathrm{m\,s^{-1}}$ with a standard deviation of less than 0.3 $\mathrm{m\,s^{-1}}$ and wind direction ~~have~~ has a mean error bias within 2° and standard deviations in 2.5° except for ~~in~~ the strongly convective case where it can reach up to 12°.

The character of the error in the reconstructed wind vector components is driven by the form of the turbulence, so that the lidar accuracy is dependent on the flow regime and vertical structure of the boundary layer. ~~This~~ Our derivation explains findings from other sensitivity studies (Klaas and Emeis, 2021; Rahlves et al., 2021) in that unstable conditions are prone to larger ~~error~~ errors than stable conditions. The error variances ~~were connected to~~ derive from weighted, spatially filtered turbulent variances in the horizontal and vertical velocities. The vertical velocity variances are of particular importance. ~~Since~~ Because the variations in vertical velocities tend to occur on smaller spatial scales, fewer of these variations are filtered out by the lidar scan volume scale. The resulting velocity perturbation variance is then weighted more heavily in the error ~~compared to~~ than horizontal perturbations, i.e. the 'projection' of the vertical velocity variations is greater on a more narrow scan cone. In convective conditions, the compounding mechanisms lead to vertical velocity perturbations almost single-handedly accounting for the error. Under stable conditions, the error magnitudes are notably smaller and result from a more balanced interplay of the vertical and horizontal velocity inhomogeneities. ~~Height trends in the error arise from the interaction of the changing filtering scale and the vertical structure of the turbulence in the boundary layer. The magnitudes grow with the increasing vertical velocity variance up into the middle of the convective boundary layers. The shallow stable boundary layer is fully encompassed in the lidar range and the error trends strongly with its profile; the error magnitudes are maximized in the mid-boundary layer where the filtered turbulence is strongest.~~ Previous work has investigated the relationship of lidar error with aggregate turbulence intensity (Courtney et al., 2014). Our findings reflect the connection, with additional separation of the turbulent fluctuations into each of the components to allow for the difference in spatial scales and weighting to come through.

The range-gate weighting in the radial velocity measurement has minimal relative effect on the total lidar error except for in high-shear regions near the surface layer. Deviations incurred in the radial velocity measurement by the weighted volume-average along the beam should vanish under constant gradients but can grow in the presence of large second derivatives in the radial velocity projection along the beam. For the most part, the impact of the larger variations over the scan volume dominate any RWF effects. In the bottom few range gates near the surface, however, the virtual lidar data reflect a prominent interaction of the RWF with shear near the surface layer leading to measurement bias. The persistent curvature of an approximately logarithmic in the profile results in significant (around $0.6 m/s$ 0.2 ms^{-1} in the stable case) and consistent underestimation under-estimation of the magnitude of along-wind horizontal component(s). Our findings are consistent with previous studies that have identified the key interaction of the RWF with shear resulting in error bias (e. g. Lindelöw et al. (2008) and Clive (2008) and Courtney et al. (2014)). (Lindelöw et al., 2008; Clive, 2008; Courtney et al., 2014).

Within the class of DBS/VAD profiling scans, any control over the reconstruction error comes from adjusting the cone angle, ϕ, and the number and spacing of the scan azimuthal angles, $\{\gamma_i\}$. The virtual instrument tests in our study held these parameters fixed to match the WindcubeV2, but other studies have explicitly investigated the sensitivity of the lidar error with respect to the scan configuration. The decomposition of the error in our study according to the derived error form, however, allows for insights into the relative impacts of the configuration choices on the error behavior.

The cone angle determines the degree of projection of the horizontal and vertical perturbations (manifest in the weighting in the error form) as well as the spatial separation of the sampling beams. In the strong and weak CBL test cases in particular, the error demonstrates strong adverse impacts of resulting heavy weighting on the vertical perturbations. The dominance of the vertical perturbation terms can be tempered by reducing the elevation angle. Teschke and Lehmann (2017) proposed a shallow elevation angle ($\phi \approx 35.26°$) based on an analytic minimization of reconstruction error in a horizontally homogeneous and stationary wind field. Rahlves et al. (2021) tested the low elevation angle with a virtual instrument in quasi-stationary convective conditions with favorable results compared to more typical, larger elevation angles. Improvements achieved by reducing the angle to lessen the weighting on the vertical velocity perturbations may be offset by the corresponding effects of increasing in the separation of the beams. In the presence of background flow gradients, larger separation can induce greater mean error, as explored in terms of linear variations of w' in Bingöl et al. (2009). In quasi-stationary cases without background gradients, the effect of the scan radius is primarily one of filtering the turbulence in the flow. Only a (high-pass) filtered portion of the full turbulent velocity variance is reflected in the variance of the velocity perturbations from the volume average which appear in the error form. Decreasing the elevation angle lengthens the filter scale, allowing for larger error variances, up to a cap determined by the full, unfiltered turbulence. We propose that the competing effects of the cone angle lead to different optimal angles depending on the flow conditions and that reasonable estimates can be performed to minimize error if rough numbers for any gradients and the magnitudes of the turbulent variances / spectra are known.

Some profiling scans use a different number of off-vertical beams to diagnose the mean winds. The beams are usually preferred to be symmetrically spaced to remove potential bias (Sathe et al., 2015; Teschke and Lehmann, 2017). Common reconstructions of the three-dimensional 3D velocity fit sinusoids to the radial velocity measurements using a least squares process (Newsom et al., 2015))least-squares process (Newsom et al., 2015). The result is a linear operation on the beam radial velocities of which the DBS scan presented in this study is a special case. The error in these alternative profiling scans should take on a similar error form to that derived here, with perturbations averaged over a greater number of beams. Under a simple stochastic model, Teschke and Lehmann (2017) showed the standard deviation of the error should be proportional to $N^{-1/2}$, with N representing the number of beams. The form our of the error model also suggests that a greater number of independent samples in the scan volume should help reduce error. We do not explicitly account for the time required to complete the scan, however, which increases with the number of beams and can become significant. Rahlves et al. (2021) tested scans using different numbers of beams without finding a universal trend in error.

The error in wind component reconstructions propagates into the error in the corresponding computation of horizontal wind speed and direction. The error was formulated in terms of the u and v reconstruction errors. A systematic positive bias in the wind speed estimate emerges from a strictly positive term that scales with u and v error variance and inversely with wind speed, which is corroborated by the virtual lidar data. These findings of a systematic positive bias do not contradict the mechanisms of possible wind speed under-estimation studied in Bingöl et al. (2009), and will coexist with the other, competing sources of bias arising from gradients in the flow. The standard deviation of the wind speed error is estimated to be on par with the u and v error standard deviations. The form of the wind speed error derived here is similar to that in Rosenbusch et al. (2021) (but only expanded to first order in the wind speed error), with similar consequences. The leading order terms are the same and a positive bias of the same scale results. The formulation used here relies on the wind component errors rather than directly using u' and v' perturbations from the mean horizontal wind. The u and v component errors behave differently than just turbulent perturbations, e.g. incorporating vertical velocity variations as shown in our analysis. These findings of a systematic overestimation do not contradict the mechanisms of possible wind speed underestimation studied in Bingöl et al. (2009) which arise from specific gradient in the flow inducing an underestimation in the first order terms.

The wind direction has no explicit bias except that arising from the u and v reconstructions. The standard deviation is roughly that of the u and v errors over the average wind speed (i.e. the error magnitudes are reduced at higher winds). The observed error magnitudes strongly depend on mean wind speeds (especially the wind direction) but are only weakly related to the relative orientation of the lidar. As in Rahlves et al. (2021), our results suggest no predominant direction of the random (u_{err}, v_{err}) $(u_{err}, v_{err})^T$ vector.

Individual measurements can suffer from large error larger errors which can be reduced through time averaging. While time averaging cannot correct for biases in the wind component measurements, the standard deviations of the error are reduced by a factor proportional to $T^{-1/2}$, thus also reducing the standard deviation of the wind speed and direction errors. The longer the decorrelation time in the error time series, the less the reduction. The use of both scalar and vector time averaging on wind speed measurements has elicited particular interest have elicited interest (Courtney et al., 2014; Clive, 2008); Rosenbusch et al. (2021) examines both the behavior of pointwise and lidar scalar and vector averaging of the winds and the different behaviors presented. We recomputed the vector average of the wind speed and direction using the time-averaged u and v horizontal wind components.Although the averages to motivate a hybrid averaging scheme to mitigate the bias of the lidar compared to scalar-averaged cup measurements. We find that the hybrid scheme does improve the bias as designed in many conditions (with exceptions where we might expect the theory to breaks down, e.g. in the top of the stable BL where vertical velocity variances are close to zero). The ideal weighting to cancel the turbulence effects in the LES test cases, assuming no bias in the wind component estimations cannot be improved, the systematic overestimation bias in the wind speed is reduced through vector time averaging (pointwise versus lidar vector-averages, shifts as expected by stability case. The scalar average would be more heavily weighted in convective conditions and more lightly in stable conditions compared to the current scheme (weight of $\frac{2}{3}$). The assumption of negligible bias in a 10-minute vector average does not universally hold across the test cases. The bias is expected to be reduced by a factor proportional to T^{-1}). under the vector average, but in regions with high initial bias and longer decorrelation times (such as the upper strong CBL), positive biases larger than $0.1\ \mathrm{m\,s^{-1}}$ do persist after a 10-minute average. A longer time average is required in such cases for the weightings in the hybrid scheme to be optimal.

Vertical velocity, with features of interest existing on smaller spatial and temporal scales, is a greater challenge to measurements by lidar lidar measurements. A vertically pointing beam omits the need for reconstruction or the implicit large scale large-scale spatial average over the scan volume. Instead, only the smaller-scale averaging from the range-gate range gate is applied. The errors associated with the vertical beam with respect to the pointwise values are significantly smaller and represent a more useful value that captures more of the small-scale variability in w.

5 Conclusions

Atmospheric variability inextricably influences error in wind lidar measurements. By using virtual instruments acting on LES flows, error mechanisms can be isolated and explicitly tracked and analyzed to better understand the error behavior as a whole. In this study, we considered profiling lidar measurements in quasi-stationary conditions. Even in the absence of explicit sources of inhomogeneity, observation error can arise, tightly coupled to the character of turbulence in the flow. The error distributions of a virtual WindcubeV2 lidar were estimated from ensembles of virtual lidar run in uniform, ideal WRF-LES scenarios in convective and stable boundary layer regimes. An analytic error model leverages random variable representations to describe how the turbulent variability propagates into the lidar error, decomposing the contributions from velocity perturbations at each beam from the volume average and from deviations in the point measurement due to range-gate weighting.

To define the error, we compared virtual measurements against both a pointwise truth reference and the average over the scan volume. With 10-minute averaging, the distinction between the kinds of spatio-temporal averages fades and the two error distributions converge, although time averaging cannot correct for bias. The systematic overestimation bias in the wind speed is reduced through vector time-averaging. Hybrid scalar-vector time-averages can also be effectively used to reduce bias in comparisons with cup measurements in many flow conditions. Further, we show why the lidar accuracy depends on atmospheric stability. Unstable conditions induce larger errors than stable conditions because of the role of vertical velocity variances.

While we derive our error estimates by considering the u and v components of the flow, any error in wind component reconstructions propagates into the error in the corresponding computation of horizontal wind speed and direction. Error in wind speed is similar to that of u and v, with a tendency for a positive bias. There is no systematic bias for wind direction.

Fully leveraging the access to the flow field afforded by an LES model, virtual lidar tools allow for not only predicting instrument error but also for separating and analyzing potentially competing mechanisms ~~which~~ that give rise to the error. Performance optimization of the model implementation, for the intensive interpolation routines in particular, would reduce the computational cost and allow longer scan times and larger ensembles to be studied. The results would benefit ~~from a comparison~~ by comparing with field data from an actual Windcube instrument and ~~investigation of~~ investigating ways to identify the mechanisms and possible behavior of error in the data. For specifically targeted quantities ~~/~~and heights, optimizations of the scan using knowledge of likely mechanisms should be tested to confirm expected behaviors. Working from this baseline study, additional complications to the flow field could be introduced, e.g. complex terrain, heterogeneous flows like turbine wakes or canopy flows, or deployment of lidars on moving platforms such as ships, buoys, vans, or aircraft.

Code and data availability. Virtual lidar code may be found at https://gitlab.com/raro0632/virtual-lidar. Ensemble data collected from the virtual lidar for the LES test cases analyzed here are archived at https://doi.org/10.5281/zenodo.6112629.

Appendix A: Error distribution moments with orientation disaggregation

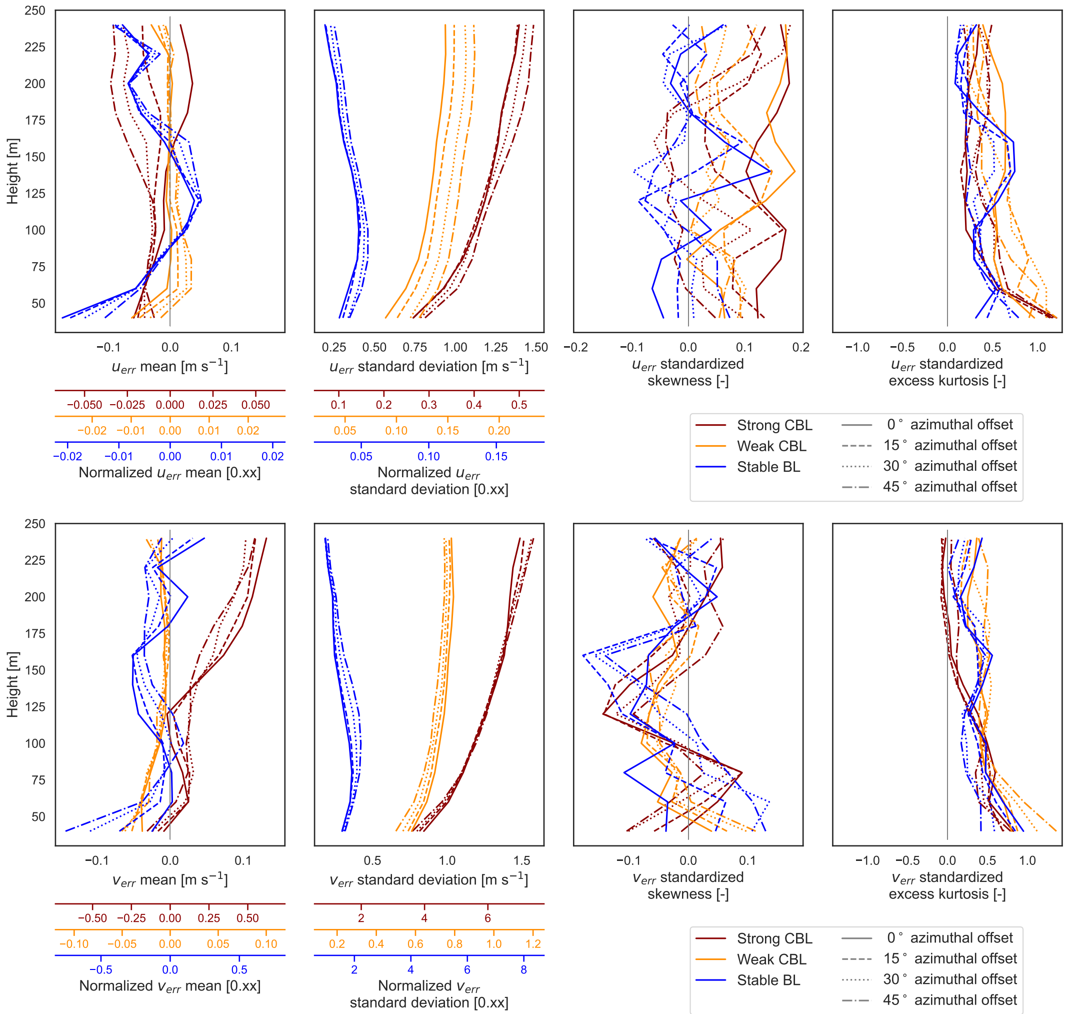

Figure A1. Comparison of u and v error distribution moments over disaggregated lidar orientation angles. No offset, same axes as LES domain (solid~~line~~), rotated 15° ~~CCW~~ counter-clockwise from LES domain axes (dashed), rotated 30° ~~CCW~~ counter-clockwise (dotted), and 45° ~~CCW~~ counter-clockwise (~~dash-dot~~dashed-dotted).

Appendix B: ~~Sample-based estimates~~ Derivation of ~~statistical moments~~wind speed and direction error means

~~For a random variable X which has been sampled with observed values $\{x_i\}$, the definitions used for the unbiased estimators of the full population/distribution moments are as follows.~~

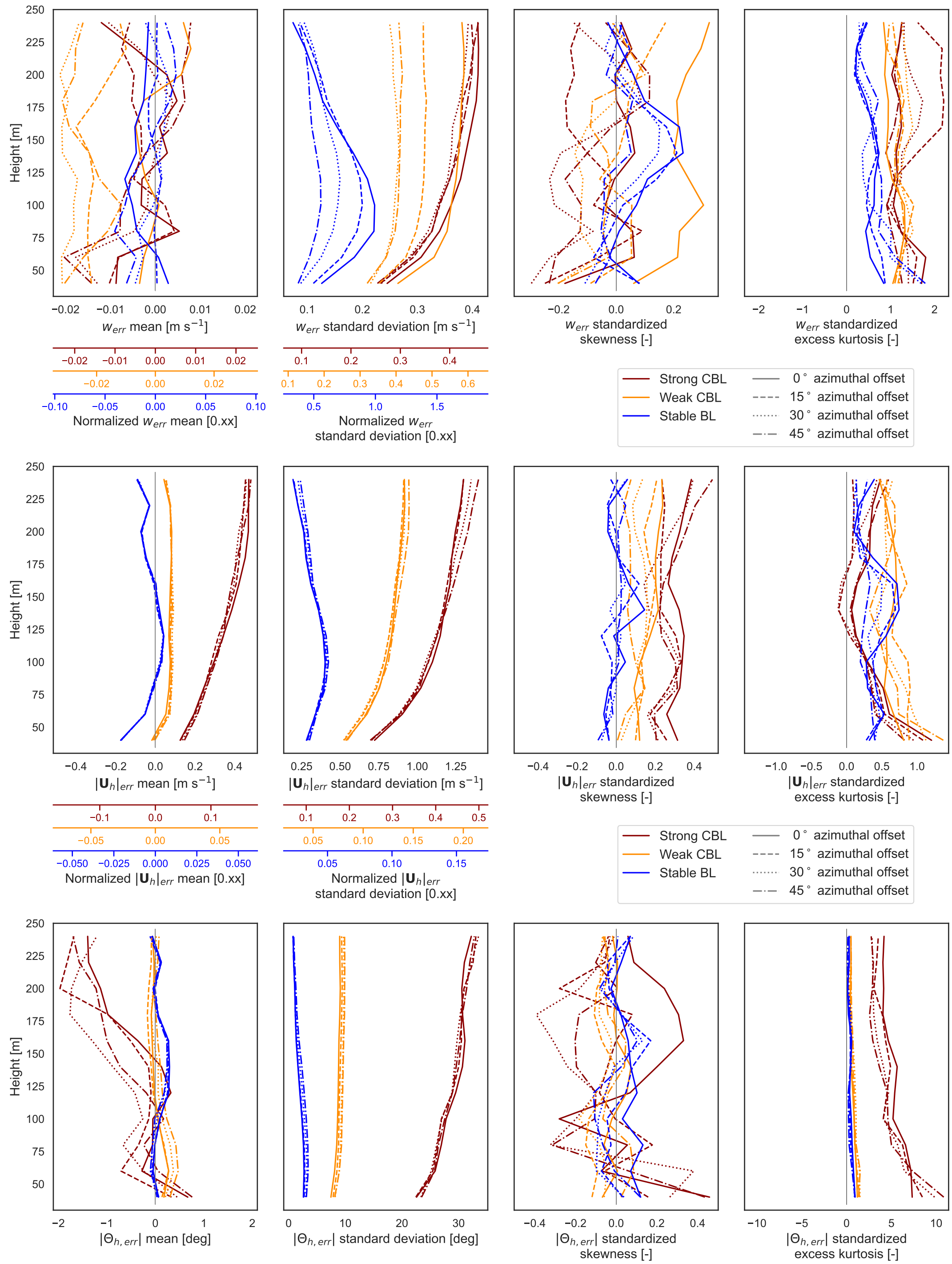

Figure A2. Comparison of error distribution moments over disaggregated lidar orientation angles. No offset, same axes as LES domain (solid~~line~~), rotated 15° ~~CCW~~ counter-clockwise from LES domain axes (dashed), rotated 30° ~~CCW~~ counter-clockwise (dotted), and 45° ~~CCW~~ counter-clockwise (~~dash-dot~~dashed-dotted).

(Mean) $\mu \approx \frac{1}{N}\sum_{i=1}^{N} x_i$

(Centered Variance) $\sigma^2 \approx s^2 = \frac{1}{N-1}\sum_{i=1}^{N}(x_i-\mu)^2$

(Standardized Skewness) $\hat{\mu_3} \approx \hat{m}_3 = \frac{N}{(N-1)(N-2)}\sum_{i=1}^{N}\left(\frac{x_i-\mu}{s}\right)^3$

(Standardized Excess Kurtosis) $\hat{\mu}_4 \approx \hat{m}_4 = \frac{N(N+1)}{(N-1)(N-2)(N-3)}\sum_{i=1}^{N}\left(\frac{x_i-\mu}{s}\right)^4 - \frac{3(N-1)^2}{(N-2)(N-3)}$

Appendix C: Derivation of wind speed and direction error means

The he mean wind speed error value is computed by taking the expected value of the random variable equation for wind speed error was derived in equation 34. Compute the expected value. (Eq. 34). We can further simplify if the component errors are assumed to have zero mean .

$$\mu(|\boldsymbol{U}_h|_{err}) = \mu\left[\frac{U}{|\boldsymbol{U}_h|}u_{err} + \frac{V}{|\boldsymbol{U}_h|}v_{err} + \frac{u_{err}^2+v_{err}^2}{2|\boldsymbol{U}_h|}\right]$$

$$= \frac{U}{|\boldsymbol{U}_h|}\mu(u_{err}) + \frac{V}{|\boldsymbol{U}_h|}\mu(v_{err}) + \frac{\sigma^2(u_{err})+\mu^2(u_{err})+\sigma^2(v_{err})+\mu^2(v_{err})}{2|\boldsymbol{U}_h|}$$

$$\approx \frac{\sigma^2(u_{err})+\sigma^2(v_{err})}{2|\boldsymbol{U}_h|}$$

a mean of zero.

$$\mu(|\boldsymbol{U}_h|_{err}) = \mu\left[\frac{U}{|\boldsymbol{U}_h|}u_{err} + \frac{V}{|\boldsymbol{U}_h|}v_{err} + \frac{u_{err}^2+v_{err}^2}{2|\boldsymbol{U}_h|}\right]$$

$$= \frac{U}{|\boldsymbol{U}_h|}\mu(u_{err}) + \frac{V}{|\boldsymbol{U}_h|}\mu(v_{err}) + \frac{\sigma^2(u_{err})+\mu^2(u_{err})+\sigma^2(v_{err})+\mu^2(v_{err})}{2|\boldsymbol{U}_h|}$$

$$\approx \frac{\sigma^2(u_{err})+\sigma^2(v_{err})}{2|\boldsymbol{U}_h|} \quad \text{(B1)}$$

The approximated wind direction function 34 argument of the inverse tangent function in the wind direction error (Eq. 34) is the ratio of two random variables, each of which is a linear function of the component errors. Compute We start by finding the expected value of the approximated form.

$$\mu(\Theta_{h,err}) \approx \mu\left(\frac{Vu_{err}-Uv_{err}}{|\boldsymbol{U}_h|^2+Uu_{err}+Vv_{err}}\right)$$

$$= \mu(Vu_{err}-Uv_{err})\mu\left(\frac{1}{|\boldsymbol{U}_h|^2+Uu_{err}+Vv_{err}}\right)$$

$$= [V\mu(u_{err})-U\mu(v_{err})]\,\frac{1}{|\boldsymbol{U}_h|^2}\mu\left[1-\left(\frac{U}{|\boldsymbol{U}_h|^2}u_{err}+\frac{V}{|\boldsymbol{U}_h|^2}v_{err}\right)+\left(\frac{U}{|\boldsymbol{U}_h|^2}u_{err}+\frac{V}{|\boldsymbol{U}_h|^2}v_{err}\right)^2-\cdots\right]$$

$$\approx [V\mu(u_{err})-U\mu(v_{err})]\,\frac{1}{|\boldsymbol{U}_h|^2}$$

$$= \frac{1}{|\boldsymbol{U}_h|}\left(\cos(-\Theta)\mu(u_{err})-\sin(-\Theta)\mu(v_{err})\right)$$

argument.

$$\mu\left(\frac{Vu_{err}-Uv_{err}}{|\boldsymbol{U}_h|^2+Uu_{err}+Vv_{err}}\right)=\mu\left(\frac{X}{Y}\right) \tag{B2}$$

If the component errors Using an established approximation for the expected value of a ratio of random variables based on Taylor series expansions (Kendall et al., 1994), we can expand the expected value of the ratio.

$$\mu\left(\frac{X}{Y}\right)\approx\frac{\mu(X)}{\mu(Y)}-\frac{\mathrm{Cov}(X,Y)}{[\mu(Y)]^2}+\frac{\sigma^2(Y)\mu(X)}{[\mu(Y)]^3} \tag{B3}$$

Letting X and Y refer to the numerator and denominator of the bound respectively, we can solve for the means. If we assume the u and v component errors are zero, we may simplify further.

$$\mu(X)=\mu(Vu_{err}-Uv_{err})=V\mu(u_{err})-U\mu(v_{err})\approx 0 \tag{B4}$$

$$\mu(Y)=\mu(|\boldsymbol{U}_h|^2+Uu_{err}+Vv_{err})=|\boldsymbol{U}_h|^2+U\mu(u_{err})+V\mu(v_{err})\approx|\boldsymbol{U}_h|^2 \tag{B5}$$

Assuming u_{err} and v_{err} have zero mean, then the wind direction error is zerogiving us the result for the means of X and Y above, and further that u_{err} and v_{err} are uncorrelated, compute the covariance.

$$\begin{aligned}\mathrm{Cov}(X,Y) &= \mathrm{Cov}(Vu_{err}-Uv_{err},|\boldsymbol{U}_h|^2+Uu_{err}+Vv_{err})\\ &= \mu\left[(Vu_{err}-Uv_{err})(|\boldsymbol{U}_h|^2+Uu_{err}+Vv_{err}-|\boldsymbol{U}_h|^2)\right]\\ &= \mu\left[UVu_{err}^2+V^2u_{err}v_{err}-U^2u_{err}v_{err}-UVv_{err}^2\right]\\ &\approx UV\left[\sigma^2(u_{err})-\sigma^2(v_{err})\right]\end{aligned} \tag{B6}$$

Similarly, we can obtain the variance with the same assumptions about the means of

$$\sigma^2(Y) = \mu\left[(|\boldsymbol{U}_h|^2 + Uu_{err} + Vv_{err} - |\boldsymbol{U}_h|^2)^2\right]$$

$$= \mu\left[U^2u_{err}^2 - 2UVu_{err}v_{err} + V^2v_{err}^2\right] \quad \text{(B7)}$$

$$\approx U^2\sigma^2(u_{err}) + V^2\sigma^2(v_{err}) \quad \text{(B8)}$$

Substituting back into Eq. B3,

$$\mu\left(\frac{X}{Y}\right) \approx \frac{0}{|\boldsymbol{U}_h|^2} - \frac{UV\left[\sigma^2(u_{err}) - \sigma^2(v_{err})\right]}{|\boldsymbol{U}_h|^4} + \frac{\left[U^2\sigma^2(u_{err}) + V^2\sigma^2(v_{err})\right]\cdot 0}{|\boldsymbol{U}_h|^6} = -\frac{UV\left[\sigma^2(u_{err}) - \sigma^2(v_{err})\right]}{|\boldsymbol{U}_h|^4} \approx 0 \quad \text{(B9)}$$

If the wind component errors have zero mean and are uncorrelated then we get the expected bias in Eq. B9. The remaining term should be small if the variance of u_{err} and v_{err} are similar and the wind speed is appreciable (making $|\boldsymbol{U}_h|^4$ large). The approximation of zero mean bias, lack of correlation, and similar variances holds when the horizontal error vector $(u_{err}, v_{err})^T$ has a direction about evenly distributed and the magnitude is relatively consistent about the circle.

Even in the presence of small biases in u and v, moderate winds serve to keep any bias in the wind direction in check. In the presence of very weak winds, however, small deviations of the mean biases from zero can be magnified in the wind direction bias. ~~If they are nonzero, large wind speeds can temper the bias and high wind speeds compound it.~~

The mean wind direction error is given by $\mu(\arctan(X/Y)) = \arctan(\mu(X/Y))$. Since we expect the mean of the ratio to be close to zero, so too do we expect the wind direction bias to be close to zero.

Appendix C: Derivation of error bound on ~~RWF weighted~~ RWF-weighted radial velocity measurement

Let $v_r(r_0)$ be the actual radial velocity at radius r_0 and $\overline{v}_r(r_0)$ the observed, range-gate-weighted radial velocity centered at r_0. Let ~~$T > 0$~~ $R > 0$ be an arbitrary threshold to split the integral.

We ~~'ll~~ willl assume the $v_r(s)$ profile has at least two continuous derivatives. The ~~range gate~~ range-gate weighting function, $\rho(s)$, should generally be non-negative, symmetric, and satisfy $\int_{-\infty}^{\infty}\rho(s)ds = 1$ by definition so we assume these properties as well.

Using the triangle inequality, integral mean value theorem, and Taylor series expansion, we have the following derivation.

$$
\begin{aligned}
|\,\overline{v}_r(r_0) - v_r(r_0)| &= \left|\int_{-\infty}^{\infty} \rho(s) v_r(r_0+s)ds - v_r(r_0)\right| \\
&\leq \left|\ \int_{|s|>T} \rho(s) v_r(r_0+s)ds\right| + \left|\ \int_{|s|\leq T} \rho(s) v_r(r_0+s)ds - v_r(r_0)\right| \\
&\leq \max_{s>|T|} |v_r(r_0+s)| \int_{|s|>T} \rho(s)ds + \left|\ \int_{|s|\leq T} \rho(s) v_r(r_0+s)ds - v_r(r_0)\right| \\
&= \max_{s>|T|} |v_r(r_0+s)| \int_{|s|>T} \rho(s)ds + \left|\ \int_{|s|\leq T} \rho(s) \left[v_r(r_0) + v_r'(r_0)s + \tfrac{1}{2} v_r''(r_0+\xi(s))s^2\right] ds - v_r(r_0)\right| \\
&= \max_{s>|T|} |v_r(r_0+s)| \left[1 - \int_{|s|\leq T} \rho(s)ds\right] + \left| v_r(r_0) \left(\ \int_{|s|\leq T} \rho(s)ds - 1\right) + v_r'(r_0) \int_{|s|\leq T} \rho(s)sds + \tfrac{1}{2} v_r''(r_0+\xi_*) \int_{|s|\leq T} \rho(s \right. \\
&\leq \left[1 - \int_{|s|\leq T} \rho(s)ds\right] \left(\max_{s>|T|} |v_r(r_0+s)| + |v_r(r_0)|\right) + \left[\ \tfrac{1}{2} \int_{|s|\leq T} \rho(s)s^2 ds\right] |v_r''(r_0+\xi_*)|
\end{aligned}
$$

$$
\begin{aligned}
|\,\overline{v}_r(r_0) - v_r(r_0)| &= \left|\int_{-\infty}^{\infty} \rho(s) v_r(r_0+s)ds - v_r(r_0)\right| \\
&\leq \left|\ \int_{|s|>R} \rho(s) v_r(r_0+s)ds\right| + \left|\ \int_{|s|\leq R} \rho(s) v_r(r_0+s)ds - v_r(r_0)\right| \\
&\leq \max_{|s|>R} |v_r(r_0+s)| \int_{|s|>R} \rho(s)ds + \left|\ \int_{|s|\leq R} \rho(s) v_r(r_0+s)ds - v_r(r_0)\right| \\
&= \max_{|s|>R} |v_r(r_0+s)| \int_{|s|>R} \rho(s)ds + \left|\ \int_{|s|\leq R} \rho(s) \left[v_r(r_0) + v_r'(r_0)s + \frac{1}{2} v_r''(r_0+\xi(s))s^2\right] ds - v_r(r_0)\right| \\
&= \max_{|s|>R} |v_r(r_0+s)| \left[1 - \int_{|s|\leq R} \rho(s)ds\right] + \left| v_r(r_0) \left(\ \int_{|s|\leq R} \rho(s)ds - 1\right) + v_r'(r_0) \int_{|s|\leq R} \rho(s)sds + \frac{1}{2} v_r''(r_0+\xi_*) \int_{|s|\leq R} \rho(s)s^2 ds\right| \\
&\leq \left[1 - \int_{|s|\leq R} \rho(s)ds\right] \left(\max_{|s|>R} |v_r(r_0+s)| + |v_r(r_0)|\right) + \left[\frac{1}{2} \int_{|s|\leq R} \rho(s)s^2 ds\right] |v_r''(r_0+\xi_*)| \qquad \text{(C1)}
\end{aligned}
$$

~~Growth and decay of the coefficients in the bounding terms of the radial velocity measurement error with increasing threshold distance T. The WindcubeV2 RWF (equation 6 with parameters in table 1) is used for illustration.~~

~~Where we 've introduced $\xi : [-T, T] \to [-T, T]$~~ Where we have introduced $\xi : [-R, R] \to [-R, R]$ as part of the Taylor remainder. The relative sizes of the coefficients with choice of ~~T~~ R in the WindcubeV2 RWF (~~equation~~ Eq. 6) are plotted in ~~figure~~ Fig. C1.

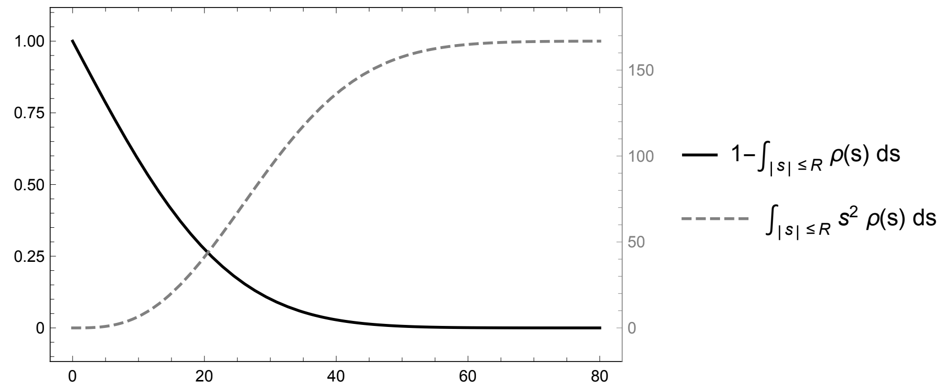

Figure C1. Growth and decay of the coefficients in the bounding terms of the radial velocity measurement error with increasing threshold distance, R. The WindcubeV2 RWF (Eq. 6 with parameters in Table 1) is used for illustration.

Appendix D: Numeric computation of RWF convolution

The numeric computation of the range-gate-weighted radial velocity involves approximating a convolution integral for a continuous weighted average. The estimate should ideally maintain the weighted average nature of the operation to prevent, e.g., underestimating under-estimating the result by virtue of only incorporating a sub-unity set of weights. For this reason, previous implementations (Forsting et al., 2017; Lundquist et al., 2015) have implemented the RWF convolution as a discrete weighted average using re-normalized RWF values at the corresponding points.

$$\int_{-\infty}^{\infty} \rho(s) v_r(r+s) ds \approx \int_{-T}^{T} \rho(s) v_r(r+s) ds \approx \frac{1}{\sum_i \rho(s_i)} \sum_k \rho(s_k) v_r(s_k)$$

$$\int_{-\infty}^{\infty} \rho(s) v_r(r+s) ds \approx \int_{-R}^{R} \rho(s) v_r(r+s) ds \approx \frac{1}{\sum_i \rho(s_i)} \sum_k \rho(s_k) v_r(s_k) \tag{D1}$$

The quadrature form amounts to a re-scaled midpoint rule when the nodes ($\{s_k\}$) are equispaced; rewrite to show explicitly.

$$\sum_k \frac{\rho(s_k)}{\sum_i \rho(s_i)} v_r(s_k) = \sum_k \frac{h\rho(s_k)}{h\sum_i \rho(s_i)} v_r(s_k) = \frac{1}{\sum_i h\rho(s_i)} \sum_k h\rho(s_k) v_r(s_k)$$

$$\sum_k \frac{\rho(s_k)}{\sum_i \rho(s_i)} v_r(s_k) = \sum_k \frac{h\rho(s_k)}{h\sum_i \rho(s_i)} v_r(s_k) = \frac{1}{\sum_i h\rho(s_i)} \sum_k h\rho(s_k) v_r(s_k) \tag{D2}$$

For nodes that are not equispaced, it suggests that the variable interval width, h_k, should be incorporated into the approximation such that it is still a ~~rescaled midpoint rule.~~

$$\int_{-\infty}^{\infty} \rho(s)v_r(r+s)ds \approx \frac{1}{\sum_i h_i\rho(s_i)} \sum_k h_k\rho(s_k)v_r(s_k)$$

re-scaled mid-point rule.

$$\int_{-\infty}^{\infty} \rho(s)v_r(r+s)ds \approx \frac{1}{\sum_i h_i\rho(s_i)} \sum_k h_k\rho(s_k)v_r(s_k) \tag{D3}$$

First, we ~~'ll~~ will truncate the domain over which we try to estimate the integral to a finite interval. The omitted contribution from the ends of the infinite integration interval can be bound small using ~~that~~ the fact that the ~~the~~ tails of the RWF must vanish in order for the infinite integral $\int_{-\infty}^{\infty} \rho(s)ds = 1$ to converge.

$$\left|\frac{1}{\sum_i h_i\rho(s_i)} \sum_k h_k\rho(s_k)v_r(r+s_k) - \int_{-\infty}^{\infty} \rho(s)v_r(r+s)ds\right|$$

$$\leqq \left|\frac{1}{\sum_i h_i\rho(s_i)} \sum_k h_k\rho(s_k)v_r(r+s_k) - \int_{-T}^{T} \rho(s)v_r(r+s)ds\right| + \left|\int_{|s|>T} \rho(s)v_r(r+s)ds\right|$$

$$\leqq \left|\frac{1}{\sum_i h_i\rho(s_i)} \sum_k h_k\rho(s_k)v_r(r+s_k) - \int_{-T}^{T} \rho(s)v_r(r+s)ds\right| + \left[\int_{|s|>T} \rho(s)ds\right] \max_{|s|>T}|v(r+s)|$$

$$\left|\frac{1}{\sum_i h_i\rho(s_i)} \sum_k h_k\rho(s_k)v_r(r+s_k) - \int_{-\infty}^{\infty} \rho(s)v_r(r+s)ds\right|$$

$$\lessapprox \left|\frac{1}{\sum_i h_i\rho(s_i)} \sum_k h_k\rho(s_k)v_r(r+s_k) - \int_{-R}^{R} \rho(s)v_r(r+s)ds\right| + \left|\int_{|s|>R} \rho(s)v_r(r+s)ds\right|$$

$$\lessapprox \left|\frac{1}{\sum_i h_i\rho(s_i)} \sum_k h_k\rho(s_k)v_r(r+s_k) - \int_{-R}^{R} \rho(s)v_r(r+s)ds\right| + \left[\int_{|s|>R} \rho(s)ds\right] \max_{|s|>R}|v(r+s)| \tag{D4}$$

The error bound on the numeric quadrature will be derived based on the midpoint mid-point rule. Consider just one subinterval sub-interval of length h_k with midpoint mid-point at s_k.

$$\begin{aligned}
&\left|\frac{1}{\sum_i h_i\rho(s_i)}h_k\rho(s_k)v_r(r+s_k)-\int_{s_k-h_k/2}^{s_k+h_k/2}\rho(s)v_r(r+s)ds\right| \\
\equiv\ &\left|\frac{1}{\sum_i h_i\rho(s_i)}h_k\rho(s_k)v_r(r+s_k)-\int_{s_k-h_k/2}^{s_k+h_k/2}\left[\rho(s_k)v_r(r+s_k)+\left(\rho(s_k)v_r(r+s_k)\right)'(s-s_k)+\tfrac{1}{2}\left(\rho(\xi_k)v_r(r+\xi_k(s))\right)''(s-s_k)^2\right]ds\right| \\
\equiv\ &\left|\frac{1}{\sum_i h_i\rho(s_i)}h_k\rho(s_k)v_r(r+s_k)-\int_{s_k-h_k/2}^{s_k+h_k/2}\left[\rho(s_k)v_r(r+s_k)+\tfrac{1}{2}\left(\rho(\xi_k)v_r(r+\xi_k(s))\right)''(s-s_k)^2\right]ds\right| \\
\equiv\ &\left|\frac{1}{\sum_i h_i\rho(s_i)}h_k\rho(s_k)v_r(r+s_k)-\rho(s_k)v_r(r+s_k)h_k-\tfrac{1}{2}\int_{s_k-h_k/2}^{s_k+h_k/2}\left(\rho(\xi_k)v_r(r+\xi_k(s))\right)''(s-s_k)^2ds\right| \\
\leq\ &\left|\left(\frac{1}{\sum_i h_i\rho(s_i)}-1\right)h_k\rho(s_k)v_r(r+s_k)\right|+\left|\tfrac{1}{2}\int_{s_k-h_k/2}^{s_k+h_k/2}\left(\rho(\xi_k)v_r(r+\xi_k(s))\right)''s^2ds\right| \\
\leq\ &\left|\left(\frac{1}{\sum_i h_i\rho(s_i)}-1\right)h_k\rho(s_k)v_r(r+s_k)\right|+\tfrac{h_k^3}{24}\max_{|\xi_k^*-s_k|\leq h_k}\left|\left(\rho(\xi_k)v_r(r+\xi_k^*)\right)''\right|
\end{aligned}$$

$$\begin{aligned}
&\left|\frac{1}{\sum_i h_i\rho(s_i)}h_k\rho(s_k)v_r(r+s_k)-\int\limits_{s_k-h_k/2}^{s_k+h_k/2}\rho(s)v_r(r+s)ds\right| \\
\equiv\ &\left|\frac{1}{\sum_i h_i\rho(s_i)}h_k\rho(s_k)v_r(r+s_k)-\int\limits_{s_k-h_k/2}^{s_k+h_k/2}\left[\rho(s_k)v_r(r+s_k)+\left(\rho(s_k)v_r(r+s_k)\right)'(s-s_k)+\frac{1}{2}\left(\rho(\xi_k)v_r(r+\xi_k(s))\right)''(s-s_k)^2\right]ds\right| \\
\equiv\ &\left|\frac{1}{\sum_i h_i\rho(s_i)}h_k\rho(s_k)v_r(r+s_k)-\int\limits_{s_k-h_k/2}^{s_k+h_k/2}\left[\rho(s_k)v_r(r+s_k)+\frac{1}{2}\left(\rho(\xi_k)v_r(r+\xi_k(s))\right)''(s-s_k)^2\right]ds\right| \\
\equiv\ &\left|\frac{1}{\sum_i h_i\rho(s_i)}h_k\rho(s_k)v_r(r+s_k)-\rho(s_k)v_r(r+s_k)h_k-\frac{1}{2}\int\limits_{s_k-h_k/2}^{s_k+h_k/2}\left(\rho(\xi_k)v_r(r+\xi_k(s))\right)''(s-s_k)^2ds\right| \\
\leq\ &\left|\left(\frac{1}{\sum_i h_i\rho(s_i)}-1\right)h_k\rho(s_k)v_r(r+s_k)\right|+\left|\frac{1}{2}\int\limits_{s_k-h_k/2}^{s_k+h_k/2}\left(\rho(\xi_k)v_r(r+\xi_k(s))\right)''s^2ds\right| \\
\leq\ &\left|\left(\frac{1}{\sum_i h_i\rho(s_i)}-1\right)h_k\rho(s_k)v_r(r+s_k)\right|+\frac{h_k^3}{24}\max_{|\xi_k^*-s_k|\leq h_k}\left|\left(\rho(\xi_k)v_r(r+\xi_k^*)\right)''\right| \qquad \text{(D5)}
\end{aligned}$$

Sum the error accumulated over all the intervals. If the ~~subintervals~~ sub-intervals partition the full interval $[-T,T]$, then:

$$\begin{aligned}
&\left|\frac{1}{\sum_i h\rho(s_i)}\sum_k h\rho(s_k)v_r(r+s_k)-\int_{-T}^{T}\rho(s)v_r(r+s)ds\right| \\
\leq\;& \sum_k\left|\frac{1}{\sum_i h\rho(s_i)}h_k\rho(s_k)v_r(r+s_k)-\int_{s_k-h_k/2}^{s_k+h_k/2}\rho(s)v_r(r+s)ds\right| \\
\leq\;& \sum_k\left[\left|\left(\frac{1}{\sum_i h_i\rho(s_i)}-1\right)h_k\rho(s_k)v_r(r+s_k)\right|+\frac{h_k^3}{24}\max_{|\xi_k-s_k|\leq h_k}\left|(\rho(\xi_k)v_r(r+\xi_k))''\right|\right] \\
\leq\;& \left|\frac{1}{\sum_i h_i\rho(s_i)}-1\right|\sum_k h_k\rho(s_k)\left|v_r(r+s_k)\right|+\frac{\sum_k h_k^3}{24}\max_{|\xi|\leq T}\left|(\rho(\xi)v_r(r+\xi))''\right| \\
\leq\;& \left|\frac{1}{\sum_i h_i\rho(s_i)}-1\right|\max_k\left|v_r(r+s_k)\right|\sum_k h_k\rho(s_k)+\frac{\sum_k h_k^3}{24}\max_{|\xi|\leq T}\left|(\rho(\xi)v_r(r+\xi))''\right| \\
\leq\;& \left|1-\sum_k h_k\rho(s_k)\right|\max_k\left|v_r(r+s_k)\right|+\frac{\sum_k h_k^3}{24}\max_{|\xi|\leq T}\left|(\rho(\xi)v_r(r+\xi))''\right|
\end{aligned}$$

$$\begin{aligned}
&\left|\frac{1}{\sum_i h\rho(s_i)}\sum_k h\rho(s_k)v_r(r+s_k)-\int_{-T}^{T}\rho(s)v_r(r+s)ds\right| \\
\lessapprox\;& \sum_k\left|\frac{1}{\sum_i h\rho(s_i)}h_k\rho(s_k)v_r(r+s_k)-\int_{s_k-h_k/2}^{s_k+h_k/2}\rho(s)v_r(r+s)ds\right| \\
\lessapprox\;& \sum_k\left[\left|\left(\frac{1}{\sum_i h_i\rho(s_i)}-1\right)h_k\rho(s_k)v_r(r+s_k)\right|+\frac{h_k^3}{24}\max_{|\xi_k-s_k|\leq h_k}\left|(\rho(\xi_k)v_r(r+\xi_k))''\right|\right] \\
\lessapprox\;& \left|\frac{1}{\sum_i h_i\rho(s_i)}-1\right|\sum_k h_k\rho(s_k)\left|v_r(r+s_k)\right|+\frac{\sum_k h_k^3}{24}\max_{|\xi|\leq R}\left|(\rho(\xi)v_r(r+\xi))''\right| \\
\lessapprox\;& \left|\frac{1}{\sum_i h_i\rho(s_i)}-1\right|\max_k\left|v_r(r+s_k)\right|\sum_k h_k\rho(s_k)+\frac{\sum_k h_k^3}{24}\max_{|\xi|\leq R}\left|(\rho(\xi)v_r(r+\xi))''\right| \\
\lessapprox\;& \left|1-\sum_k h_k\rho(s_k)\right|\max_k\left|v_r(r+s_k)\right|+\frac{\sum_k h_k^3}{24}\max_{|\xi|\leq R}\left|(\rho(\xi)v_r(r+\xi))''\right|
\end{aligned} \tag{D6}$$

All together, the error of the numeric approximation of the integral may be bounded by:

$$\begin{aligned}
&\left|\frac{\sum_k h_k\rho(s_k)v_r(r+s_k)}{\sum_i h_i\rho(s_i)}-\int_{-\infty}^{\infty}\rho(s)v_r(r+s)ds\right| \\
&\quad\leq\left|1-\sum_k h_k\rho(s_k)\right|\max_k\left|v_r(r+s_k)\right|+\frac{\sum_k h_k^3}{24}\max_{|\xi|\leq T\,|\xi|\leq R}\left|(\rho(\xi)v_r(r+\xi))''\right|+\left[\int_{|s|>T\,|s|>R}\rho(s)ds\right]\max_{|s|>T\,|s|>R}|v(r+
\end{aligned} \tag{D7}$$

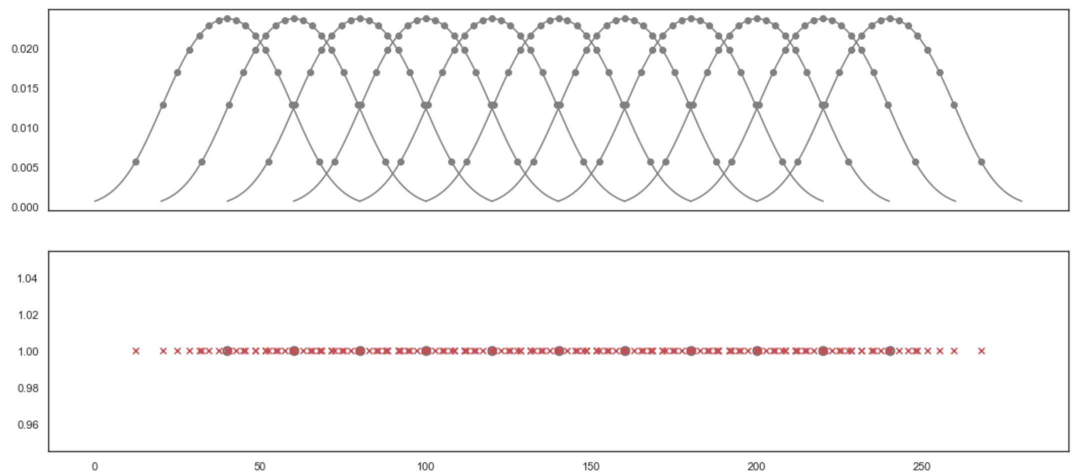

Figure D1. Using ~~fifteen~~ 15 points per range gate, the node locations $\{s_k\}$ found by imposing $h_k\rho(s_k)$ to be constant for the WindcubeV2 RWF for as many nodes as possible. ~~Top~~ The top panel shows node locations on the overlapping RWF centered at each of the ~~eleven~~ 11 range gates. ~~Bottom~~ The bottom panel shows the nodes (x's) and ~~range gate~~ range-gate centers (dots) along the one-dimensional beam length.

In addition to picking the interval ~~$[-T,T]$~~ $[-R,R]$ large enough so that the contribution from the tails is small and the usual ~~second order~~ second-order error term from the ~~midpoint~~ mid-point rule, the points should be selected so that the ~~midpoint approximation of~~ mid-point approximation of the integral of the RWF (i.e the first term) is close to one.

Choices for nodes include (1) equispaced, (2) exponentially spaced, (3) equal RWF area, and (4) equal ~~midpoint~~ mid-point area $h_k\rho(s_k)$. Equispaced points are easy to determine and implement but do not maximize the utility of each point included. For a virtual lidar, which has to interpolate the winds for every node, inefficiently using points can be computationally expensive before the quadrature is even computed. The idea behind the other node distributions is to sample more heavily near the RWF center, where each point has greater impact on the result so that we reduce the number of ~~'low utility'~~ low-utility nodes.

Exponentially spaced nodes (e.g. $\{-16,-8,-4,-2,-1,0,1,2,4,16\}$) are easy to compute independent of the particular RWF function like the equispaced nodes, but crudely achieves the goal of clustering points more heavily close to the RWF center. Forsting et al. (2017) recommend using nodes spaced so that the integral of the RWF between nodes is constant. The result is nodes clustered more heavily toward the center and more equal weighting on each node (not ~~'oversampling'~~ over-sampling the tails). Based on the ~~midpoint~~ mid-point form and error bound derived ~~above~~earlier, we propose an alternative in the same vein. We can explicitly set the $h_k\rho(s_k)$ to be constant so that every point has equal weight. Starting with $s_0 = 0$ and $h_0 = \frac{1}{N}$, where N is the total (odd) number of points, we can iteratively solve out for the symmetric nodes. In practice, the last nodes usually do not seem to be able to attain the same $h_k\rho(s_k) = 1/N$ weighting. Either the sum $\sum_k h_k\rho(s_k)$ must be reduced to less than one or the constant weighting relaxed for the end nodes. The latter is preferable to reduce the overall error.

Selecting nodes for computational expediency in the case of multiple range gates along a beam introduces further considerations than those for a single range gate. For the WindcubeV2, the intervals of dependency for the ~~20m-spaced~~ 20 m-spaced range gates overlap (D1; nodes should be reused where possible rather than interpolating a separate set of points for each range gate. Methods using spacing ~~by~~ according to the RWF area or imposing constant weighting are likely to produce unusual numbers that do not necessarily coincide between multiple range gates. Exponential spacing makes it easier to impose overlap in position. The cluster of points at the center of one range gate appear at the tail of another range gate and would have to be ~~subselected~~ sub-selected to the desired points.

Author contributions. **Rachel Robey:** methodology, software, analysis and investigation, writing and editing **Julie K. Lundquist:** conceptualization, methodology, writing and editing

Competing interests. The authors declare that they have no conflict of interest.

Disclaimer. This report was prepared as an account of work sponsored by an agency of the United States Government. Neither the United States Government nor any agency thereof, nor any of their employees, makes any warranty, express or implied, or assumes any legal liability or responsibility for the accuracy, completeness, or usefulness of any information, apparatus, product, or process disclosed, or represents that its use would not infringe privately owned rights. Reference herein to any specific commercial product, process, or service by trade name, trademark, manufacturer, or otherwise does not necessarily constitute or imply its endorsement, recommendation, or favoring by the United States Government or any agency thereof. The views and opinions of authors expressed herein do not necessarily state or reflect those of the United States Government or any agency thereof.

This work was authored by the National Renewable Energy Laboratory, operated by Alliance for Sustainable Energy, LLC, for the U.S. Department of Energy (DOE) under Contract No. DE-AC36-08GO28308. Funding provided by the U.S. Department of Energy Office of Energy Efficiency and Renewable Energy Wind Energy Technologies Office. The views expressed in the article do not necessarily represent the views of the DOE or the U.S. Government. The U.S. Government retains and the publisher, by accepting the article for publication, acknowledges that the U.S. Government retains a nonexclusive paid-up, irrevocable, worldwide license to publish or reproduce the published form of this work, or allow others to do so, for U.S. Government purposes.

Acknowledgements. Much thanks to Alex Rybchuk for use of his idealized convective boundary layer LES data, to Miguel Sanchez Gomez for his work to produce robust and stable LES case runs, and to Raghavendra Krishnamurthy for his guidance with the WindcubeV2 velocity reconstruction. The authors would also like to express appreciation to Dr. Andrew Black and two anonymous reviewers for their helpful comments and reviews of the manuscript.

This material is based upon work supported by the U.S. Department of Energy, Office of Science, Office of Advanced Scientific Computing Research, Department of Energy Computational Science Graduate Fellowship under Award Number DE-SC0021110.

This research has been supported by the US National Science Foundation (grand nos. AGS-1554055 and AGS-1565498).

We would like to acknowledge ~~high-performance computing~~ high-performance-computing support from Cheyenne (doi:10.5065/D6RX99HX) provided by ~~NCAR~~National Center for Atmospheric Energy's Computational and Information Systems Laboratory, sponsored by the National Science Foundation.

This work utilized resources from the University of Colorado Boulder Research Computing Group, which is supported by the National Science Foundation (awards ACI-1532235 and ACI-1532236), the University of Colorado Boulder, and Colorado State University.

References

Aitken, M. L. and Lundquist, J. K.: Utility-Scale Wind Turbine Wake Characterization Using Nacelle-Based Long-Range Scanning Lidar, Journal of Atmospheric and Oceanic Technology, 31, 1529–1539, https://doi.org/10.1175/JTECH-D-13-00218.1, 2014.

Aitken, M. L., Rhodes, M. E., and Lundquist, J. K.: Performance of a Wind-Profiling Lidar in the Region of Wind Turbine Rotor Disks, Journal of Atmospheric and Oceanic Technology, 29, 347–355, https://doi.org/10.1175/JTECH-D-11-00033.1, 2012.

Banakh, V., Smalikho, I., Köpp, F., and Werner, C.: Turbulent Energy Dissipation Rate Measurement Using Doppler Lidar, in: Advances in Atmospheric Remote Sensing with Lidar, edited by Ansmann, A., Neuber, R., Rairoux, P., and Wandinger, U., pp. 255–258, Springer, Berlin, Heidelberg, https://doi.org/10.1007/978-3-642-60612-0_63, 1997.

Barad, M. L.: Project Prairie Grass, a Field Program in Diffusion, Tech. Rep. AFCRC-TR-58-235(I), Air Force Cambridge Research Center Geophysics Research Directorate Geophysical Research Papers 59, 1958.

Basu, S., Holtslag, B., Van de Wiel, B., Moene, A., and Steeneveld, G.-J.: An Inconvenient "Truth" about Using Sensible Heat Flux as a Surface Boundary Condition in Models under Stably Stratified Regimes, ACTA GEOPHYSICA, 56, 88–99, https://doi.org/10.2478/s11600-007-0038-y, 2007.

Bingöl, F., Mann, J., and Foussekis, D.: Conically scanning lidar error in complex terrain, Meteorologische Zeitschrift, 18, 189–195, https://doi.org/10.1127/0941-2948/2009/0368, 2009.

Bodini, N., Zardi, D., and Lundquist, J. K.: Three-Dimensional Structure of Wind Turbine Wakes as Measured by Scanning Lidar, Atmospheric Measurement Techniques, 10, 2881–2896, https://doi.org/10.5194/amt-10-2881-2017, 2017.

Bodini, N., Lundquist, J. K., Krishnamurthy, R., Pekour, M., Berg, L. K., and Choukulkar, A.: Spatial and Temporal Variability of Turbulence Dissipation Rate in Complex Terrain, Atmospheric Chemistry and Physics, 19, 4367–4382, https://doi.org/10.5194/acp-19-4367-2019, 2019.

Bonin, T. A., Newman, J. F., Klein, P. M., Chilson, P. B., and Wharton, S.: Improvement of Vertical Velocity Statistics Measured by a Doppler Lidar through Comparison with Sonic Anemometer Observations, Atmospheric Measurement Techniques, 9, 5833–5852, https://doi.org/10.5194/amt-9-5833-2016, 2016.

Boquet, M., Royer, P., Cariou, J.-P., Machta, M., and Valla, M.: Simulation of Doppler Lidar Measurement Range and Data Availability, Journal of Atmospheric and Oceanic Technology, 33, 977–987, https://doi.org/10.1175/JTECH-D-15-0057.1, publisher: American Meteorological Society Section: Journal of Atmospheric and Oceanic Technology, 2016.

Cariou, J.-P. and Boquet, M.: LEOSPHERE Pulsed Lidar Principles, in: UpWind WP6 on Remote Sensing Devices, pp. 1–32, Orsay, France, 2010.

Cheynet, E., Jakobsen, J., Snæbjörnsson, J., Mann, J., Courtney, M., Lea, G., and Svardal, B.: Measurements of Surface-Layer Turbulence in a Wide Norwegian Fjord Using Synchronized Long-Range Doppler Wind Lidars, Remote Sensing, 9, 977, https://doi.org/10.3390/rs9100977, 2017.

Choukulkar, A., Brewer, W. A., Sandberg, S. P., Weickmann, A., Bonin, T. A., Hardesty, R. M., Lundquist, J. K., Delgado, R., Iungo, G. V., Ashton, R., Debnath, M., Bianco, L., Wilczak, J. M., Oncley, S., and Wolfe, D.: Evaluation of Single and Multiple Doppler Lidar Techniques to Measure Complex Flow during the XPIA Field Campaign, Atmospheric Measurement Techniques, 10, 247–264, https://doi.org/10.5194/amt-10-247-2017, 2017.

Clements, C. B., Lareau, N. P., Kingsmill, D. E., Bowers, C. L., Camacho, C. P., Bagley, R., and Davis, B.: The Rapid Deployments to Wildfires Experiment (RaDFIRE): Observations from the Fire Zone, Bulletin of the American Meteorological Society, 99, 2539–2559, https://doi.org/10.1175/BAMS-D-17-0230.1, 2018.

Clifton, A., Boquet, M., Burin Des Roziers, E., Westerhellweg, A., Hofsass, M., Klaas, T., Vogstad, K., Clive, P., Harris, M., Wylie, S., Osler, E., Banta, B., Choukulkar, A., Lundquist, J., and Aitken, M.: Remote Sensing of Complex Flows by Doppler Wind Lidar: Issues and Preliminary Recommendations, Tech. Rep. NREL/TP–5000-64634, 1351595, https://doi.org/10.2172/1351595, 2015.

Clive, P. J. M.: Compensation of Vector and Volume Averaging Bias in Lidar Wind Speed Measurements, IOP Conference Series: Earth and Environmental Science, 1, 012 036, https://doi.org/10.1088/1755-1315/1/1/012036, 2008.

Courtney, M., Wagner, R., and Lindelöw, P.: Testing and Comparison of LIDARs for Profile and Turbulence Measurements in Wind Energy, IOP Conference Series: Earth and Environmental Science, 1, 012 021, https://doi.org/10.1088/1755-1315/1/1/012021, 2008.

Courtney, M., Sathe, A., and Gayle Nygaard, N.: Shear and Turbulence Effects on Lidar Measurements, Report, DTU Wind Energy, 2014.

Forsting, A. R. M., Troldborg, N., and Borraccino, A.: Modelling Lidar Volume-Averaging and Its Significance to Wind Turbine Wake Measurements, J. Phys.: Conf. Ser., 854, 012 014, https://doi.org/10.1088/1742-6596/854/1/012014, 2017.

Frehlich, R.: Effects of Wind Turbulence on Coherent Doppler Lidar Performance, Journal of Atmospheric and Oceanic Technology, 14, 54–75, https://doi.org/10.1175/1520-0426(1997)014<0054:EOWTOC>2.0.CO;2, 1997.

Gasch, P., Wieser, A., Lundquist, J. K., and Kalthoff, N.: An LES-based Airborne Doppler Lidar Simulator for Investigation of Wind Profiling in Inhomogeneous Flow Conditions, Atmospheric Measurement Techniques Discussions, pp. 1–53, https://doi.org/10.5194/amt-2019-118, 2019.

Gottschall, J. and Courtney, M.: Verification Test for Three WindCubeTM WLS7 LiDARs at the Høvsøre Test Site, Report 978-87-550-3819-6, Danmarks Tekniske Universitet, Risø Nationallaboratoriet for Bæredygtig Energi, Roskilde, 2010.

Gryning, S.-E., Mikkelsen, T., Baehr, C., Dabas, A., O'Connor, E., Rottner-Peyrat, L., Sjöholm, M., Suomi, I., and Vasiljevic, N.: Measurement Methodologies for Wind Energy Based on Ground-Level Remote Sensing, in: Renewable Energy Forecasting: From Models to Applications, pp. 29–56, https://doi.org/10.1016/B978-0-08-100504-0.00002-0, 2017.

Haupt, S. E., Kosovic, B., Shaw, W., Berg, L. K., Churchfield, M., Cline, J., Draxl, C., Ennis, B., Koo, E., Kotamarthi, R., Mazzaro, L., Mirocha, J., Moriarty, P., Muñoz-Esparza, D., Quon, E., Rai, R. K., Robinson, M., and Sever, G.: On Bridging A Modeling Scale Gap: Mesoscale to Microscale Coupling for Wind Energy, Bulletin of the American Meteorological Society, 100, 2533–2550, https://doi.org/10.1175/BAMS-D-18-0033.1, publisher: American Meteorological Society Section: Bulletin of the American Meteorological Society, 2019.

Joanes, D. N. and Gill, C. A.: Comparing Measures of Sample Skewness and Kurtosis, Journal of the Royal Statistical Society. Series D (The Statistician), 47, 183–189, 1998.

Kendall, M. G., Stuart, A., Ord, J. K., and O'Hagan, A.: Kendall's Advanced Theory of Statistics, vol. 1, Edward Arnold ; Halsted Press, 6th ed edn., 1994.

Kirkil, G., Mirocha, J., Bou-Zeid, E., Chow, F., and Kosovic, B.: Implementation and Evaluation of Dynamic Subfilter-Scale Stress Models for Large-Eddy Simulation Using WRF*, Monthly Weather Review, 140, 266–284, https://doi.org/10.1175/MWR-D-11-00037.1, 2012.

Klaas, T. and Emeis, S.: The Five Main Influencing Factors on Lidar Errors in Complex Terrain, Wind Energy Science Discussions, pp. 1–25, https://doi.org/10.5194/wes-2021-26, 2021.

Klaas, T., Pauscher, L., and Callies, D.: LiDAR-mast Deviations in Complex Terrain and Their Simulation Using CFD, Meteorologische Zeitschrift, pp. 591–603, https://doi.org/10.1127/metz/2015/0637, 2015.

Krishnamurthy, R.: Windcube V2 Reconstruction, 2020.

Lindelöw, P.: Fiber Based Coherent Lidars for Remote Wind Sensing, Ph.D. thesis, Technical University of Denmark, 2008.

Lindelöw, P., Courtney, M., Parmentier, R., and Cariou, J. P.: Wind Shear Proportional Errors in the Horizontal Wind Speed Sensed by Focused, Range Gated Lidars, IOP Conference Series: Earth and Environmental Science, 1, 012 023, https://doi.org/10.1088/1755-1315/1/1/012023, 2008.

Liu, Z., Barlow, J. F., Chan, P.-W., Fung, J. C. H., Li, Y., Ren, C., Mak, H. W. L., and Ng, E.: A Review of Progress and Applications of Pulsed Doppler Wind LiDARs, Remote Sensing, 11, 2522, https://doi.org/10.3390/rs11212522, 2019.

Lumley, J. L. and Panofsky, H. A.: The Structure of Atmospheric Turbulence, no. v. 12 in Interscience Monographs and Texts in Physics and Astronomy, Interscience Publishers, 1964.

Lundquist, J. K., Churchfield, M. J., Lee, S., and Clifton, A.: Quantifying Error of Lidar and Sodar Doppler Beam Swinging Measurements of Wind Turbine Wakes Using Computational Fluid Dynamics, Atmospheric Measurement Techniques, 8, 907–920, https://doi.org/10.5194/amt-8-907-2015, 2015.

Maronga, B., Gryschka, M., Heinze, R., Hoffmann, F., Kanani-Sühring, F., Keck, M., Ketelsen, K., Letzel, M. O., Sühring, M., and Raasch, S.: The Parallelized Large-Eddy Simulation Model (PALM) Version 4.0 for Atmospheric and Oceanic Flows: Model Formulation, Recent Developments, and Future Perspectives, Geoscientific Model Development, 8, 2515–2551, https://doi.org/10.5194/gmd-8-2515-2015, 2015.

Mazzaro, L. J., Muñoz-Esparza, D., Lundquist, J. K., and Linn, R. R.: Nested Mesoscale-to-LES modeling of the atmospheric boundary layer in the presence of under-resolved convective structures, Journal of Advances in Modeling Earth Systems, 9, 1795–1810, https://doi.org/https://doi.org/10.1002/2017MS000912, 2017.

Menke, R., Vasiljević, N., Wagner, J., Oncley, S. P., and Mann, J.: Multi-lidar wind resource mapping in complex terrain, Wind Energy Science, 5, 1059–1073, https://doi.org/10.5194/wes-5-1059-2020, publisher: Copernicus GmbH, 2020.

Mirocha, J. D., Lundquist, J. K., and Kosović, B.: Implementation of a Nonlinear Subfilter Turbulence Stress Model for Large-Eddy Simulation in the Advanced Research WRF Model, Monthly Weather Review, 138, 4212–4228, https://doi.org/10.1175/2010MWR3286.1, 2010.

Mirocha, J. D., Rajewski, D. A., Marjanovic, N., Lundquist, J. K., Kosović, B., Draxl, C., and Churchfield, M. J.: Investigating Wind Turbine Impacts on Near-Wake Flow Using Profiling Lidar Data and Large-Eddy Simulations with an Actuator Disk Model, Journal of Renewable and Sustainable Energy, 7, 043 143, https://doi.org/10.1063/1.4928873, 2015.

Muñoz-Esparza, D., Cañadillas, B., Neumann, T., and van Beeck, J.: Turbulent Fluxes, Stability and Shear in the Offshore Environment: Mesoscale Modelling and Field Observations at FINO1, Journal of Renewable and Sustainable Energy, 4, 063 136, https://doi.org/10.1063/1.4769201, 2012.

Muñoz-Esparza, D., Kosović, B., Mirocha, J., and van Beeck, J.: Bridging the Transition from Mesoscale to Microscale Turbulence in Numerical Weather Prediction Models, Boundary-Layer Meteorology, 153, 409–440, https://doi.org/10.1007/s10546-014-9956-9, 2014.

Muschinski, A., Sullivan, P. P., Wuertz, D. B., Hill, R. J., Cohn, S. A., Lenschow, D. H., and Doviak, R. J.: First Synthesis of Wind-Profiler Signals on the Basis of Large-Eddy Simulation Data, Radio Science, 34, 1437–1459, https://doi.org/10.1029/1999RS900090, 1999.

Newman, J. F., Klein, P. M., Wharton, S., Sathe, A., Bonin, T. A., Chilson, P. B., and Muschinski, A.: Evaluation of Three Lidar Scanning Strategies for Turbulence Measurements, Atmospheric Measurement Techniques, 9, 1993–2013, https://doi.org/10.5194/amt-9-1993-2016, 2016.

Newsom, R., Calhoun, R., Ligon, D., and Allwine, J.: Linearly Organized Turbulence Structures Observed Over a Suburban Area by Dual-Doppler Lidar, Boundary-Layer Meteorology, 127, 111–130, https://doi.org/10.1007/s10546-007-9243-0, 2008.

Newsom, R. K., Sivaraman, C., Shippert, T. R., and Riihimaki, L. D.: Doppler Lidar Wind Value-Added Product, Tech. Rep. DOE/SC-ARM/TR-148, DOE ARM Climate Research Facility, Pacific Northwest National Laboratory; Richland, Washington, https://doi.org/10.2172/1238069, 2015.

Peña, A., Kosović, B., and Mirocha, J. D.: Evaluation of Idealized Large-Eddy Simulations Performed with the Weather Research and Forecasting Model Using Turbulence Measurements from a 250 m Meteorological Mast, Wind Energy Science, 6, 645–661, https://doi.org/10.5194/wes-6-645-2021, 2021.

Raasch, S. and Schröter, M.: PALM - A Large-Eddy Simulation Model Performing on Massively Parallel Computers, Meteorologische Zeitschrift, pp. 363–372, https://doi.org/10.1127/0941-2948/2001/0010-0363, 2001.

Rahlves, C., Beyrich, F., and Raasch, S.: Scan Strategies for Wind Profiling with Doppler Lidar — An LES-based Evaluation, Atmospheric Measurement Techniques Discussions, pp. 1–27, https://doi.org/10.5194/amt-2021-417, 2021.

Rosenbusch, P., Mazoyer, P., Pontreau, L., Allain, P. E., and Cariou, J.-P.: Wind Speed Reconstruction from Mono-Static Wind Lidar Eliminating the Effect of Turbulence, Journal of Renewable and Sustainable Energy, 13, 063 301, https://doi.org/10.1063/5.0048810, 2021.

Rybchuk, A., Alden, C. B., Lundquist, J. K., and Rieker, G. B.: A Statistical Evaluation of WRF-LES Trace Gas Dispersion Using Project Prairie Grass Measurements, Monthly Weather Review, 149, 1619–1633, https://doi.org/10.1175/MWR-D-20-0233.1, 2021.

Rösner, B., Egli, S., Thies, B., Beyer, T., Callies, D., Pauscher, L., and Bendix, J.: Fog and Low Stratus Obstruction of Wind Lidar Observations in Germany—A Remote Sensing-Based Data Set for Wind Energy Planning, Energies, 13, 3859, https://doi.org/10.3390/en13153859, number: 15 Publisher: Multidisciplinary Digital Publishing Institute, 2020.

Salesky, S. T., Chamecki, M., and Bou-Zeid, E.: On the Nature of the Transition Between Roll and Cellular Organization in the Convective Boundary Layer, Boundary-Layer Meteorology, 163, 41–68, https://doi.org/10.1007/s10546-016-0220-3, 2017.

Sanchez Gomez, M., Lundquist, J., Mirocha, J., Arthur, R., and Muñoz-Esparza, D.: Quantifying Wind Plant Blockage under Stable Atmospheric Conditions, https://doi.org/10.5194/wes-2021-57, 2021.

Sathe, A. and Mann, J.: Measurement of Turbulence Spectra Using Scanning Pulsed Wind Lidars, Journal of Geophysical Research: Atmospheres, 117, https://doi.org/10.1029/2011JD016786, 2012.

Sathe, A., Mann, J., Gottschall, J., and Courtney, M. S.: Can Wind Lidars Measure Turbulence?, Journal of Atmospheric and Oceanic Technology, 28, 853–868, https://doi.org/10.1175/JTECH-D-10-05004.1, 2011.

Sathe, A., Mann, J., Vasiljevic, N., and Lea, G.: A Six-Beam Method to Measure Turbulence Statistics Using Ground-Based Wind Lidars, Atmospheric Measurement Techniques, 8, 729–740, https://doi.org/10.5194/amt-8-729-2015, 2015.

Simley, E., Pao, L., Frehlich, R., Jonkman, B., and Kelley, N.: Analysis of Wind Speed Measurements Using Continuous Wave LIDAR for Wind Turbine Control, in: 49th AIAA Aerospace Sciences Meeting Including the New Horizons Forum and Aerospace Exposition, Aerospace Sciences Meetings, American Institute of Aeronautics and Astronautics, https://doi.org/10.2514/6.2011-263, 2011.

Simley, E., Fürst, H., Haizmann, F., and Schlipf, D.: Optimizing Lidars for Wind Turbine Control Applications—Results from the IEA Wind Task 32 Workshop, Remote Sensing, 10, 863, https://doi.org/10.3390/rs10060863, number: 6 Publisher: Multidisciplinary Digital Publishing Institute, 2018.

Skamarock, W. C., Klemp, J. B., Dudhia, J., Gill, D. O., Liu, Z., Berner, J., Wang, W., Powers, J. G., Duda, M. G., Barker, D. M., and Huang, X.-Y.: A Description of the Advanced Research WRF Model Version 4, Tech. rep., UCAR/NCAR, https://doi.org/10.5065/1DFH-6P97, 2019.

Smith, E. N., Gebauer, J. G., Klein, P. M., Fedorovich, E., and Gibbs, J. A.: The Great Plains Low-Level Jet during PECAN: Observed and Simulated Characteristics, Monthly Weather Review, 147, 1845–1869, https://doi.org/10.1175/MWR-D-18-0293.1, 2019.

Stawiarski, C., Träumner, K., Knigge, C., and Calhoun, R.: Scopes and Challenges of Dual-Doppler Lidar Wind Measurements—An Error Analysis, Journal of Atmospheric and Oceanic Technology, 30, 2044–2062, https://doi.org/10.1175/JTECH-D-12-00244.1, 2013.

Teschke, G. and Lehmann, V.: Mean Wind Vector Estimation Using the Velocity–Azimuth Display (VAD) Method: An Explicit Algebraic Solution, Atmospheric Measurement Techniques, 10, 3265–3271, https://doi.org/10.5194/amt-10-3265-2017, 2017.

Thobois, L., Krishnamurthy, R., Boquet, M., Cariou, J.-P., Santiago, A., and Sas, L.: Coherent Pulsed Doppler LIDAR Metrological Performances and Applications for Wind Engineering, p. 13, 2015.

Virtanen, P., Gommers, R., Oliphant, T. E., Haberland, M., Reddy, T., Cournapeau, D., Burovski, E., Peterson, P., Weckesser, W., Bright, J., van der Walt, S. J., Brett, M., Wilson, J., Millman, K. J., Mayorov, N., Nelson, A. R. J., Jones, E., Kern, R., Larson, E., Carey, C. J., Polat, İ., Feng, Y., Moore, E. W., VanderPlas, J., Laxalde, D., Perktold, J., Cimrman, R., Henriksen, I., Quintero, E. A., Harris, C. R., Archibald, A. M., Ribeiro, A. H., Pedregosa, F., van Mulbregt, P., SciPy 1.0 Contributors, Vijaykumar, A., Bardelli, A. P., Rothberg, A., Hilboll, A., Kloeckner, A., Scopatz, A., Lee, A., Rokem, A., Woods, C. N., Fulton, C., Masson, C., Häggström, C., Fitzgerald, C., Nicholson, D. A., Hagen, D. R., Pasechnik, D. V., Olivetti, E., Martin, E., Wieser, E., Silva, F., Lenders, F., Wilhelm, F., Young, G., Price, G. A., Ingold, G.-L., Allen, G. E., Lee, G. R., Audren, H., Probst, I., Dietrich, J. P., Silterra, J., Webber, J. T., Slavič, J., Nothman, J., Buchner, J., Kulick, J., Schönberger, J. L., de Miranda Cardoso, J. V., Reimer, J., Harrington, J., Rodríguez, J. L. C., Nunez-Iglesias, J., Kuczynski, J., Tritz, K., Thoma, M., Newville, M., Kümmerer, M., Bolingbroke, M., Tartre, M., Pak, M., Smith, N. J., Nowaczyk, N., Shebanov, N., Pavlyk, O., Brodtkorb, P. A., Lee, P., McGibbon, R. T., Feldbauer, R., Lewis, S., Tygier, S., Sievert, S., Vigna, S., Peterson, S., More, S., Pudlik, T., Oshima, T., Pingel, T. J., Robitaille, T. P., Spura, T., Jones, T. R., Cera, T., Leslie, T., Zito, T., Krauss, T., Upadhyay, U., Halchenko, Y. O., and Vázquez-Baeza, Y.: SciPy 1.0: Fundamental Algorithms for Scientific Computing in Python, Nature Methods, 17, 261–272, https://doi.org/10.1038/s41592-019-0686-2, 2020.

Wainwright, C. E., Stepanian, P. M., Chilson, P. B., Palmer, R. D., Fedorovich, E., and Gibbs, J. A.: A Time Series Sodar Simulator Based on Large-Eddy Simulation, Journal of Atmospheric and Oceanic Technology, 31, 876–889, https://doi.org/10.1175/JTECH-D-13-00161.1, 2014.

Zwillinger, D. and Kokoska, S.: CRC Standard Probability and Statistics Tables and Formulae, Chapman & Hall/CRC, Boca Raton, Fla, 2000.